

TECHNISCHE UNIVERSITÄT MÜNCHEN

Lehrstuhl E21 für korrelierte Elektronensysteme  
Walther-Meißner-Institut für Tieftemperaturforschung  
der Bayerischen Akademie der Wissenschaften

Crystal growth and characterization of  
magnetic properties of the electron  
underdoped cuprate superconductor  
 $\text{Nd}_{2-x}\text{Ce}_x\text{CuO}_4$

Alma G. Dorantes Palacios

Vollständiger Abdruck der von der Fakultät für Physik der Technischen  
Universität München zur Erlangung des akademischen Grades eines

**Doktors der Naturwissenschaften**

genehmigten Dissertation.

Vorsitzender: Prof. Dr. Andreas Weiler

Prüfer der Dissertation: 1. Prof. Dr. Peter Böni  
2. Dr. habil. Rudolf Hackl

Die Dissertation wurde am 08.05.2018 bei der Technischen Universität München  
eingereicht und durch die Fakultät für Physik am 09.07.2018 angenommen.



---

## Kurze Zusammenfassung

Die antiferromagnetische (AF) Ordnung des elektronendotierten Kupratsupraleiters erstreckt sich im Phasendiagramm mindestens bis zum supraleitenden (SC) Bereich. Es ist unklar, ob es Bereiche gibt, in denen AF und SC Ordnung koexistieren. Hier wurden Einkristalle der Verbindung  $\text{Nd}_{2-x}\text{Ce}_x\text{CuO}_4$  (NCCO) besonders langsam gezüchtet. Messungen dieser Kristalle weisen darauf hin, dass sich die SC Eigenschaften bei diesen Kristallen verbessert haben. Durch die Messung des winkelabhängigen Widerstands in hohen Magnetfeldern konnte antiferromagnetische Ordnung nachgewiesen werden.

## Abstract

The antiferromagnetic (AF) order of electron-doped cuprates extends up to at least the superconducting (SC) region of the phase diagram. Whether the AF and SC states coexist is still a matter of controversy. In this thesis, single crystals of  $\text{Nd}_{2-x}\text{Ce}_x\text{CuO}_4$  (NCCO) were grown with a slow growth rate. The observations point to an improvement of the SC properties. Furthermore, a sharp irreversible feature has been found in the angle-dependent magnetoresistance for a broad doping range of NCCO in the high-field regime, which can be considered as an unambiguous sign of long-range AF order.



---

## Preface

The preparation and production of crystals has been in practice since the times of the alchemists. The crystallization of salt by evaporation of seawater or the extraction of sugar from sugarcane are amongst the oldest methods of crystal growth [1]. This very interdisciplinary subject might have its scientific roots in Johannes Kepler's essay "The six-cornered snowflake: a new year's gift"[2] from the 17<sup>th</sup> century, where he pondered the symmetry with which snowflakes crystallize. While this question remained unanswered for many years, his remarks on the sphere close packing of solids set the basis for the no less famous studies of William Barlow, who described the body-centered cubic, face-centered cubic and hexagonal close packed structures that we know today [3]. An amateur geologist, he also derived the 230 space groups, a discovery also made by E. S. Fedorov and Arthur Schoenflies, and predicted the crystal structures of NaCl and CsCl before the invention of X-ray diffraction [4]. Later on, the works of Gibbs and Ostwald on phase equilibrium and competitive growth provided a thermodynamic understanding of the crystal growth process and more refined methods could be developed [1, 5]. Nowadays the methods of Czochralski, Bridgman, Kyropoulos and Stockbarger have become more elegant [6]. With the Czochralski method, for example, it is possible to produce massive silicon single crystals at industrial rates. Applications for artificially grown crystals can be found in many fields such as electronics, optics and spintronics, and devices including oscillators, polarizers, lasers etc. In the field of biology, protein crystallization is immensely important to solve protein structures which can be useful in the development of drugs or as reaction catalyzers [1]. Crystals are at the heart of modern technology and are of fundamental importance for understanding the physical properties of solids, behavior prediction and the development of new materials. A good crystal can change the way we understand matter.

A classic example was the synthesis of  $\text{YBa}_2\text{Cu}_3\text{O}_{7-\delta}$  (YBCO) in  $\text{BaZrO}_3$  crucibles [7]. The discovery of high temperature superconductivity caused a big in-

---

crease in the efforts to find and develop superconducting materials with high enough critical currents which could be used for technical applications. When reports of an anomalous increase in the magnetisation of YBCO under applied magnetic field were announced [8], the excitement was inevitable. Some theoretical approaches were used to try to explain the so-called fishtail anomaly with, for example, collective pinning theory [9]. Another approach to this problem was more focused on materials science and considered the role of structural inhomogeneities as the root of the phenomenon. The debate was finished when metallic impurity-free single crystals of YBCO were grown and it was proven that the origin of the anomaly laid in the oxygen sublattice and the formation of oxygen vacancy clusters which could be manipulated by a careful annealing process [7, 10].

The need for high quality single crystals continues to be a major issue in the field of physics, materials science and chemistry. The secrets to high temperature superconductivity remain hidden and despite the years of research, many of the questions are still open for debate, in particular in the realm of electron doped superconductors. The asymmetry of the hole- and electron-doped sides of the 214 phase diagram, the coexistence of the antiferromagnetic and superconducting regimes and the reason for the loss in quantum oscillations in underdoped cuprates are only two examples of the unresolved issues in these compounds.

This thesis deals with the crystal growth and characterization of the magnetic properties of the electron-doped cuprate superconductor  $\text{Nd}_{2-x}\text{Ce}_x\text{CuO}_4$  (NCCO), with particular focus on the underdoped regime of the phase diagram. The work is divided in two sections. In Part I an overview of the structural and physical properties of NCCO will be given and the crystal growth and sample preparation methods will be presented. The focus of part I is the investigation of the effect of the growth rates on the sample properties. For this purpose, the characterization of two NCCO  $x = 0.125$  crystals grown with different growth rates will be discussed. The investigation was performed by the use of X-ray fluorescence spectroscopy for elemental analysis, magnetic susceptibility for the determination of superconducting properties, neutron diffraction for structural and magnetic analysis, and a short mention of transport measurements for the detection of certain distinct features of long-range antiferromagnetic order. Additionally, the implications of the change in growth rates on the required post-growth annealing

---

treatment will be discussed for two NCCO single crystals with  $x = 0.13$ . Finally, a short characterization of NCCO crystals with low dopant concentration will be presented.

In the second part of this thesis, the focus will be on the study of magnetic changes in the spin system of underdoped NCCO crystals by the use of magneto-transport measurements. In this part, the focus is the investigation of the origin of a hysteretic step-like feature detected in the angle-dependent magnetoresistance in the high-field regime at field orientations around the Cu-O-Cu direction. This study was motivated by reports from the literature [11] and observations made in earlier investigations conducted at the Walther-Meißner Institute [12, 13]. The observed behavior will be explained in terms of a high field rearrangement of the antiferromagnetic collinear spin structure of the  $\text{Cu}^+$  spins. This model allows to understand the presence of the step-like feature for the NCCO system in the dopant concentration range investigated in this work. It will be argued that this feature is an unambiguous sign of long-range antiferromagnetic order.



# Contents

	Page
Abstract	iii
Preface	v
<b>I Crystal growth and effect of the growth rate on the superconducting properties of <math>\text{Nd}_{2-x}\text{Ce}_x\text{CuO}_4</math></b>	<b>1</b>
<b>1 Introduction</b>	<b>3</b>
1.1 The electron-doped cuprate superconductors . . . . .	3
1.1.1 The electron-doped cuprate superconductor $\text{Nd}_{2-x}\text{Ce}_x\text{CuO}_4$	7
1.2 Crystal growth . . . . .	9
1.2.1 The annealing process . . . . .	9
1.2.2 The traveling solvent floating zone method . . . . .	11
1.3 Sample preparation: change in the growth rate . . . . .	15
<b>2 NCCO <math>x = 0.125</math></b>	<b>19</b>
2.1 X-Ray Fluorescence . . . . .	19
2.1.1 Results . . . . .	22
2.2 Magnetic susceptibility . . . . .	25
2.2.1 Results . . . . .	26
2.3 Elastic neutron scattering . . . . .	31
2.3.1 Results . . . . .	35
2.4 Transport measurements . . . . .	41
2.4.1 Results . . . . .	42
2.5 Discussion on NCCO $x = 0.125$ . . . . .	48

<b>3</b>	<b>NCCO <math>x = 0.13</math></b>	<b>55</b>
3.0.1	Results . . . . .	56
<b>4</b>	<b>NCCO: other dopings</b>	<b>63</b>
4.0.2	Results . . . . .	63
<b>5</b>	<b>Conclusion</b>	<b>69</b>
<b>II</b>	<b>Angle-dependent Magnetoresistance of underdoped <math>\text{Nd}_{2-x}\text{Ce}_x\text{CuO}_4</math></b>	<b>75</b>
<b>6</b>	<b>Introduction</b>	<b>77</b>
6.1	n-doped cuprates: general aspects of electronic and magnetic structure . . . . .	77
6.1.1	Magnetic structure of the n-doped cuprates . . . . .	77
6.1.2	Transport properties . . . . .	80
<b>7</b>	<b>Experimental details</b>	<b>85</b>
7.1	Samples: preparation and contacts . . . . .	85
7.2	The rotating system . . . . .	87
7.2.1	The experimental setup . . . . .	87
7.3	Measurement sequence . . . . .	89
<b>8</b>	<b>Results</b>	<b>91</b>
8.1	Non-superconducting NCCO samples . . . . .	92
8.2	Superconducting NCCO samples . . . . .	102
8.3	Effect of annealing on the AMR of two $x = 0.12$ samples . . . . .	105
<b>9</b>	<b>Discussion</b>	<b>111</b>
<b>10</b>	<b>Addendum: As-grown NCCO</b>	<b>121</b>
10.1	Results . . . . .	121
10.2	Discussion . . . . .	127
<b>11</b>	<b>Conclusions and Outlook</b>	<b>131</b>
	<b>Bibliography</b>	<b>135</b>

<b>List of publications</b>	<b>145</b>
<b>Acknowledgements</b>	<b>147</b>
<b>12 Acknowledgements</b>	<b>147</b>



## **Part I**

**Crystal growth and effect of the  
growth rate on the superconducting  
properties of  $\text{Nd}_{2-x}\text{Ce}_x\text{CuO}_4$**



# 1 Introduction

## 1.1 The electron-doped cuprate superconductors

In 1988 a new class of high temperature cuprate superconductor was reported [14–16]. The new 214 compound had layers of Cu ions surrounded by square planar oxygens and had the chemical formula  $Ln_{2-x}A_xCuO_4$  where  $Ln = Nd, Pr, Sm, Eu$  and  $A = Ce, Th$  [17]. Soon it became clear that this new superconductor could be a good alternative to further investigate the many enigmas in the field of High- $T_c$  superconductivity.

The electron doped cuprates are tetragonal with space group  $I4/mmm$  and typical lattice parameters of  $a = b \sim 3.95 \text{ \AA}$  and  $c \sim 12.1 \text{ \AA}$ . In contrast to the hole-doped cuprates, they crystallize in the  $T'$  structure, in which the site of the apical oxygen is not occupied [18, 19]. Since the coordination number of the copper is 4, the relative positions of the oxygen in the charge reservoirs are shifted and thus the adjacent  $CuO_2$  layers are displaced by  $(\frac{a}{2}, \frac{a}{2})$  between each other, which results in an expansion of the in-plane unit cell [18, 20]. As a result of this displacement, the  $T'$  structure unit cell is shorter in the  $c$  direction than the  $T$  structure and the unit cell volume varies with the change in the rare-earth ionic radius [20]. A visual comparison of the  $T$  structure of the hole-doped cuprates and the  $T'$  structure is shown in Fig. 1.1.

In addition to the structural differences between the electron and hole-doped cuprates, a representation of the relation of the superconducting transition temperature  $T_c$  and Néel temperature  $T_N$  with respect to dopant concentration  $x$ , shown in Fig. 1.2, reveals a very noticeable asymmetry between their superconducting properties. For the hole-doped cuprates, the  $T_N$  drops below  $x = 0.05$  and superconductivity exists for a wide doping range [22]. On the other hand, the antiferromagnetic (AF) ground state in the electron-doped cuprates is broader and extends with increasing dopant concentration up to at least the supercon-

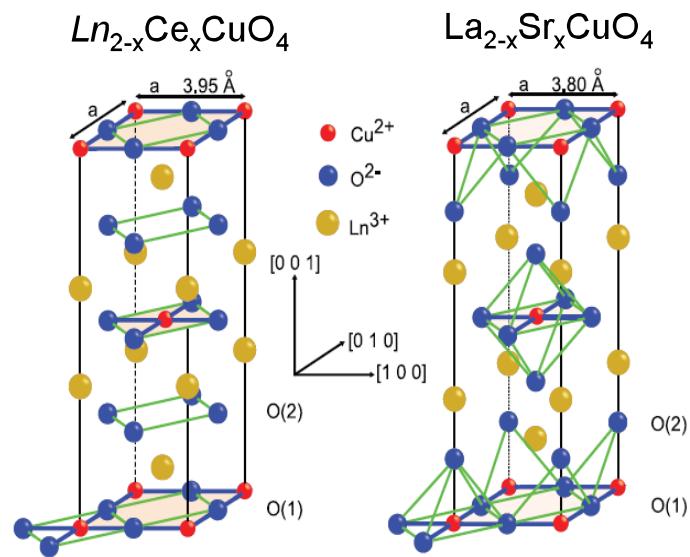


Figure 1.1: Crystal structure of the electron and hole-doped 214 cuprates [21]. **Left:** Body centered  $T'$  structure of the electron-doped cuprates. The oxygens in the  $CuO_2$  planes are labeled O(1) and the oxygens in the rare-earth oxide charge reservoirs are O(2). The O(2) are exactly above and below the O(1) positions. **Right:**  $T$  structure of the hole-doped cuprates. The apical oxygen sites, above and below the copper atoms, are occupied.

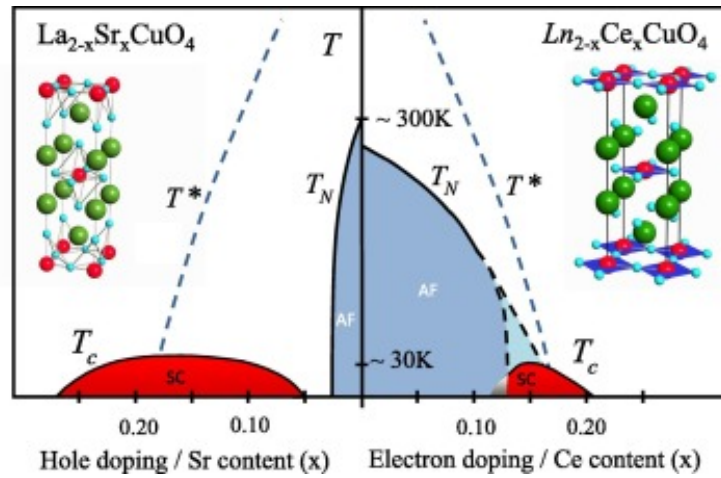


Figure 1.2: Electronic phase diagram of the cuprate superconductors  $\text{La}_{2-x}\text{Sr}_x\text{CuO}_4$  and  $\text{Ln}_{2-x}\text{Ce}_x\text{CuO}_4$ , respectively [18]. The red area indicates the superconducting (SC) regime and the blue area corresponds to the antiferromagnetic (AF) phase. The light blue area on the electron doped side corresponds to strong magnetic correlations but without long range order.  $T^*$  represents the pseudogap line, below this temperature anomalous behavior is observed. In the very overdoped regime, the e-doped cuprates become more metallic but not superconducting.

ducting (SC) region of the phase diagram without a well-defined separation between the SC and AF states. Whether the AF order coexists with superconductivity, and if yes, to which extent, remains a matter of controversy.

A number of techniques which are sensitive to magnetic structure, such as neutron scattering and muon spin relaxation, have been used to probe the extent of antiferromagnetism according to dopant concentration. Studies of elastic and inelastic neutron scattering on electron doped cuprates have been reported on a wide dopant concentration range, from the undoped parent compound up to the overdoped regime [23, 24]. While traces of antiferromagnetism are still detected even in optimally doped samples in their as-grown and annealed states [25], it has been argued that the border between long range AF order and superconductivity is at  $x = 0.134$  and, that the observation of AF bragg peaks above this  $x$  corresponds to remnants of not fully annealed parts of the sample [26].

On the other hand, the study of magnetic order with muon spin rotation ( $\mu$ SR) has presented many different results. Uefiji et al. [27] concluded that the SC and AF order have a competitive coexistence, similar to the hole-doped cuprates. Others have argued that the static AF order gradually decreases as the dopant concentration approaches  $x = 0.15$  and the border lies around  $x = 0.14$  without any sign of coexistence between these two states [28]. Another study suggests that the AF order is already suppressed at  $x = 0.09$  and that the two phases have a region where they coexist [29].

Within this discussion it is commonly recognized that electron doping affects the electronic properties of the cuprates in a different manner than the hole doping, for the insertion of electrons in the system does not destroy the AF order as easily as hole doping.

Furthermore, one very important difference between the electron and hole-doped superconductors is the need for a post-growth annealing treatment to induce superconductivity in the electron-doped cuprates [20, 30]. To date, it is not completely clear why such a procedure is necessary and nor is it clear what effect it has on the material [19, 31–34]. The most accepted theory is that heat treatment eliminates impurities and scattering centers in the structure, i.e. removal of apical oxygen [31, 34]. Nonetheless, it has also been proposed that the secondary phase  $Ln_2O_3$ , which is caused by the reduction process and grows epitaxially to the  $CuO_2$  layers, could be responsible for fixing Cu vacancies in the conduction

layers and thus lowering the amount of breaking sites [32]. It has also been suggested that the AF order can only be disturbed by modification of the oxygen content on the  $\text{CuO}_2$  planes which should enhance the electron mobility [19, 35].

Despite these controversies, the electron-doped cuprates are interesting compounds which can be useful for understanding the physical properties of High- $T_c$  superconductivity. With a solubility limit at  $x = 0.18$  [20], it is possible to explore the whole superconducting (SC) regime of the phase diagram with one compound. Their normal state properties can be easily accessed, since they have much lower critical magnetic fields. Additionally, unlike the hole-doped cuprates, they do not go through a structural phase transition, which means a wide temperature range can be explored without structural interferences [30]. In this work the superconducting and magnetic properties of  $\text{Nd}_{2-x}\text{Ce}_x\text{CuO}_4$  (NCCO) single crystals will be discussed, with particular focus on the border of the SC range of the phase diagram.

### 1.1.1 The electron-doped cuprate superconductor $\text{Nd}_{2-x}\text{Ce}_x\text{CuO}_4$

The parent compound of NCCO,  $\text{Nd}_2\text{Cu}_4$  (NCO), is a charge transfer insulator and shows long-range antiferromagnetic (AF) order [36]. Through the insertion of charge carriers, bulk superconductivity is observed for a doping range  $0.13 \leq x \leq 0.18$ , with optimal doping at  $x_{\text{opt}} = 0.145$  and a transition temperature of  $T_{c,\text{opt}} = 24$  K [20]. The Cu-O bond is a covalent bond formed between the orbitals  $3d_{x^2-y^2}$  of the copper and  $2p_x$  of the oxygen. Substitution of  $\text{Nd}^{3+}$  with  $\text{Ce}^{4+}$  introduces electrons in the antibonding half of the  $\sigma_{x^2-y^2}^*$  orbital [37]. Since the electrostatic potential of the out-of-plane oxygen inhibits fluctuations of electrons into the copper site, the introduction of electrons is more favorable in the  $T'$  structure due to the absence of apical oxygen [38].

In relation to the debate concerning the extent of the long-range AF order and to further understand the hole-electron doped asymmetry in the phase diagram, NCCO has been probed by angle-resolved photoemission spectroscopy (ARPES) and high-field magnetotransport measurements to study the Fermi surface (FS) and its evolution with doping. From ARPES experiments a large FS has been identified which is reconstructed from a gaped contour at  $x = 0.04$  to a hole-like FS centered around the  $(\pi, \pi)$  position at  $x = 0.15$ . This reconstruction has been ascribed to antiferromagnetic correlations up to optimal SC doping [39–42],

whereas in a very recent work [43] only short-range AF fluctuations in the SC region have been detected.

Furthermore, the Shubnikov-de Haas (SdH) quantum oscillations in the inter-layer magnetoresistance of NCCO [44, 45] provided insight into the optimal and overdoped regimes of the phase diagram. SdH oscillations were observed on NCCO single crystals for  $x = 0.15 - 0.17$ . This observation coincided with ARPES experiments and band structure calculation on the size of the FS. Moreover, the slow oscillations for  $x = 0.15$  and  $0.16$  revealed a reconstruction of the Fermi surface which survives up to the upper border of the SC doping range. However, immediately below the optimal doping,  $x_{\text{opt}} = 0.145$ , the oscillations were completely suppressed. It is not fully understood why the oscillations vanish, while it could be an indicator of the disappearance of the hole pockets in the FS, it could also be due to a debilitation of the orbital effect on the interlayer conductivity. The origin of the Fermi surface reconstruction in the SC range and how it develops upon entering the underdoped regime is still unknown. It is not clear whether this reconstruction is caused by the AF order or by the recently detected charge-density modulation [46–48].

Because of the large extent of the long-range AF order in the electron doped cuprates, NCCO is a good probe to look for charge order (CO), since some theoretical models claim that CO has a magnetic order origin [49]. Until a recent report on resonant x-ray scattering which announced the existence of charge order (CO) in NCCO [48], it had not been clear if CO is a universal property of the cuprate superconductors or if it only exists in the hole-doped side of the phase diagram. In this study, it was claimed that the AF order is not directly related to CO. However, the CO in NCCO showed some discrepancies with the CO of the hole-doped cuprates, such as insensitivity to superconductivity and short temperature-independent correlation length. Possibly the secondary phase  $\text{Nd}_2\text{O}_3$  acts as source of length scale disorder and pinning centers [48]. Additionally, the observed peaks were in fact broader and weaker than those for the hole-doped superconductors [50]. This can be a direct effect of crystal quality.

Considering the above stated arguments and controversies surrounding the physical properties of the underdoped regime of the electron doped cuprates, a study of the crystal growth and physical properties of NCCO is necessary, particularly in the doping regime close to the emergence of bulk superconductivity. A

quantitative determination of the SC volume fraction of underdoped NCCO and spatial homogeneity could be crucial for understanding the relation of antiferromagnetism and superconductivity in electron-doped cuprates [11, 34, 51].

In Part I of this work, the crystal growth of underdoped NCCO single crystals will be investigated. For a better understanding of the influence of the growth parameters on the sample properties, the physical properties of the NCCO single crystals will be studied in relation to the growth rate. Additionally, in order to confirm sample homogeneity in relation to the as-grown rod, a comparison of samples originated from different parts of the rod along the diameter will be performed. Analysis will determine if the use of a slow growth rate in the growing method produces crystals which require a shorter post-growth annealing process. With the use of a slow growth rate, samples with low dopant concentrations  $x = 0.10$  and  $x = 0.11$  will be synthesized to determine if superconductivity can be observed in the low dopant concentration regime.

## 1.2 Crystal growth

In order to efficiently characterize the electron-doped cuprates, high quality crystals are needed. Two factors are of great importance to achieve this: the growth method and the post-growth annealing treatment. The crystals should be obtained through a reliable process and, accordingly, the as-grown crystals must be annealed under fully controlled conditions. While the traveling solvent floating zone (TSFZ) method has been more ubiquitously used recently and most of the growth conditions are established, the need of a post-growth annealing treatment is still an issue. Until now, there is no formal methodology for the reduction process and there are many differences between the approaches each experimentalist takes. This could lead to sample dependent physical properties. In Section 1.2.1 a short overview of the annealing treatment will be given and later in Section 1.3 the growth technique of NCCO with the TSFZ method will be presented.

### 1.2.1 The annealing process

Several approaches have been considered for achieving the most effective reduction process. For example, for the annealing process of NCCO with  $x = 0.15$  a

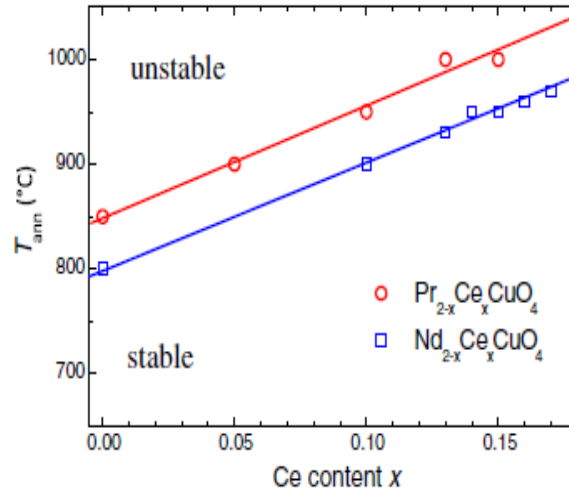


Figure 1.3: Stability diagram of  $\text{Nd}_{2-x}\text{Ce}_x\text{CuO}_4$  and  $\text{Pr}_{2-x}\text{Ce}_x\text{CuO}_4$ . The solid lines are a guide to the eye. Above the depicted line, the samples will decompose into  $\text{Nd}_2\text{O}_3$  and  $\text{Cu}_2\text{O}$  [30].

3 day long process at  $980^\circ\text{C}$  has been reported [52]. However, this only represents one case. In fact, the annealing process can be carried out at temperatures ranging from  $850^\circ\text{C}$  to  $1080^\circ\text{C}$  for several hours, even up to several days in an inert atmosphere [20] and in some cases a second oxygenation is even added to the process [23]. In the so-called 2-step annealing process a high-temperature annealing at  $750^\circ\text{C}$ – $850^\circ\text{C}$  and oxygen pressure of  $8 \times 10^{-2}$  Torr is followed by low-temperature annealing at  $450^\circ\text{C}$ – $700^\circ\text{C}$  in a vacuum [34, 53]. With the use of this method, superconductivity in the parent compound has been claimed to be possible. However, these results have only been observed for thin films.

Another factor to be considered is that the reduction process is highly dependent on the dopant concentration. For strongly underdoped samples to slightly overdoped, it has been shown that the maximum allowed annealing temperature increases according to dopant concentration [30]. Above the stability temperature shown in the diagram of Fig. 1.3 samples will decompose. Nonetheless, it has been shown that if the annealing treatment is systematically performed in time sequences of 20 hours, the SC volume fraction increases with each heat treatment before decomposition [54].

Furthermore, no matter which method is used to reduce the samples, there is the issue of the secondary phase  $\text{Nd}_2\text{O}_3$  induced by the heat treatment [20, 32, 33].

This phase forms epitaxially to the  $\text{CuO}_2$  layers, is cubic with a space group  $Ia\bar{3}$ , and has similar lattice parameters in the  $a$  and  $b$  plane as NCCO. Its presence can have some manifestations in the physical properties of NCCO and thus interfere with the data interpretation. Particularly in the case of NCCO, the  $\text{Nd}^{3+}$  ions can be polarized by the application of a magnetic field and, for example, for neutron scattering measurements the magnetic reflections will be enhanced [55].

### 1.2.2 The traveling solvent floating zone method

The TSFZ method has been for several years the standard method to grow crystals of electron-doped cuprates. High purity, dopant homogeneity and, due to the anisotropic character of these compounds, desired orientation are some of the standards which can be fulfilled by the use of this technique. The many advantages and an extensive explanation of the method have been discussed in past works [54] but a short overview of the process is given in this Chapter.

A 214 compositional phase diagram along with schematics of the process are shown in Fig. 1.4. The system consists of a polycrystalline feed rod, a preferably monocrystalline seed rod and the solvent between the two rods. The solvent is a small  $\text{CuO}$ -rich flux pellet with composition  $x$ , which is between compositions labeled as  $x_P$  and  $x_E$  (Fig. 1.4). These three components are vertically mounted in a parabolic-mirror furnace so their tips meet at the focal point of the ellipsoidal mirrors. This area is locally molten by heat radiation and is held together by surface tension. Working temperatures must be between  $T_P$  and  $T_E$ , i.e. between the peritectic and eutectic point along the liquidus line. At these conditions, the 214 phase is dissolved into the flux and transported to the growth front by diffusion and convection due to the rotation of the seed and feed rod. Crystallization occurs at the top of the seed rod. The stage of the mirror furnace moves in the upward direction and the molten zone is drawn upwards, as a result a single crystalline rod is left behind. For an optimal growth process certain conditions should be satisfied [56]. The zone heating should be uniform, so a correct adjustment of the halogen lamps is crucial. The growth front should be as flat as possible. This is achieved through temperature control and rotation of the rods. The gas atmosphere should have the correct pressure to assure stoichiometric composition and stabilization of the molten zone. If all parameters are met, a single crystal can be grown which is free of impurities, has a homogeneous composition along

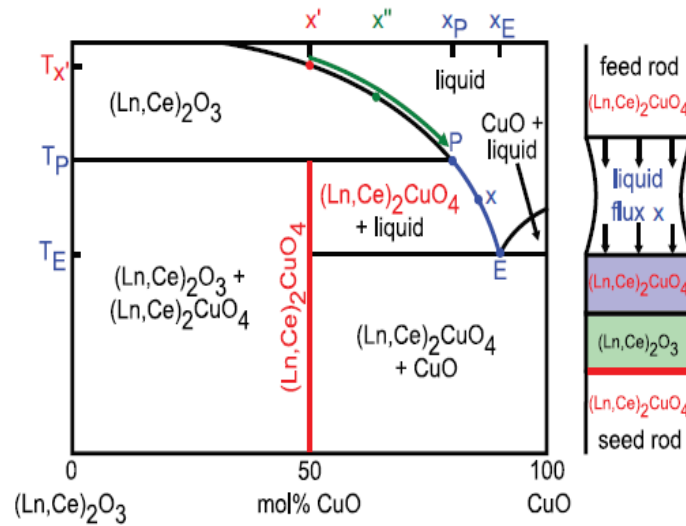


Figure 1.4: Illustration of the working principle of the TSFZ method. Adapted from [21]. **Left:** Compositional phase diagram of the 214 system. The red solidus line corresponds to the composition of the desired crystal. P and E are the peritectic and eutectic points, respectively. **Right:** Representation of the vertical arrangement of the feed and seed rods connected via the molten zone. The polycrystalline material is dissolved into the flux which has a composition  $x$ . The vertical arrows represent the transport of the dissolved material to the lower solid-liquid interface, where it crystallizes. The feed and seed rods are rotated in opposite directions to assure diffusion and convection. The colors correspond to the composition of the solvent zone at a particular stage of the growth process. In this particular case the growth is started without a CuO pellet and the flux is obtained by firstly increasing the temperature to  $T_{x'}$  and then decreasing it following the liquidus line.

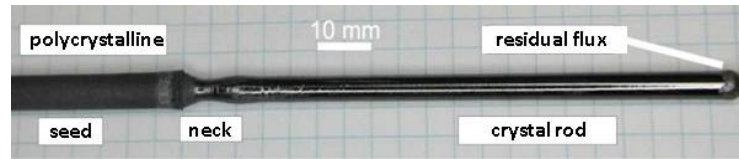


Figure 1.5: As-grown crystal rod of NCCO. The seed rod is polycrystalline. At the beginning of the growth process the rod crystal develops a neck, which is good for the grain selection. Note that the surface of the rod becomes smoother and shinier as the growth process advances. Normally, samples are cut from the uppermost part of the rod to reduce the possibility of secondary grains in the samples.

the length of the rod and which can very easily be oriented since the preferred growth direction is grown in the vertical direction; all of this without the need of a crucible, which is known to be a source of impurities. A picture of an as-grown NCCO crystal rod is shown in Fig.1.5

The homogeneity of the dopant concentration along the length of the rod has been tested by EDX [21] and for some studies the chemical composition is tested by inductively coupled plasma (ICP) spectroscopy [26]. However, a subject which has not been thoroughly studied is the radial homogeneity of the crystal rods grown by the TSFZ method. For example, scant attention has been paid to the differences between the physical or chemical properties of the inner and outer parts of the rod. In order to test the differences between these two parts of the rod, in a neutron scattering study [33], a rod was cut and separated into the core and the shell of the original rod. These two parts were subsequently measured independently from each other. Although no significant difference between the transition temperature  $T_c$  or SC volume fraction was observed, the outer part of the rod showed stronger magnetism, which was interpreted as a difference in the oxygen concentration and it was suggested that the inner part of the rod provides a better sample.

From electron probe microanalysis, it has been suggested that the Ce concentration has a gradient towards the center of the rod and that it decreases at the surface [57]. If, for samples from a single crystal rod, there is a relation between a higher concentration of Ce and the measured magnetic properties of a crystal, a gradient in Ce concentration along the diameter of the rod could be an explanation.

Nd <sub>2-x</sub> Ce <sub>x</sub> CuO <sub>4</sub>				
doping $x$	atmosphere	pressure	flow rate	power
0	O <sub>2</sub>	4 – 5 bar	0.2 l/min	70 %
$0 < x \leq 0.15$	8 % O <sub>2</sub> / 92 % Ar	3 – 4 bar	0.2 l/min	64 %
$x > 0.15$	3 % O <sub>2</sub> / 97 % Ar	3 – 4 bar	0.2 l/min	63 %

Table 1.1: Relation of the growth atmosphere to the dopant concentration. The column of power refers to the power of the halogen lamps in the mirror furnace, 100 % corresponds to the maximum power of 4 lamps of 300 W. Adapted from [21].

Considering the role of oxygen in the SC properties of the electron-doped cuprates, not only the reduction process can be manipulated, but the growth process itself can be adjusted. The oxygen atmosphere is a crucial parameter in the crystal growth of NCCO. It has been shown that, for the crystal growth of optimally doped and overdoped samples, the oxygen partial pressure in the growth atmosphere must be low, but a higher oxygen concentration is needed for the growth of underdoped samples (see Table 1.1). Furthermore, only the parent compound can be grown in a full oxygen atmosphere [30]. It has been speculated that the growth at lower oxygen partial pressure is analogous to the reduction process, since it reduces the oxygen content of the system *in situ* [23]. However even under these conditions, the reduction process is still inevitable. If this step cannot be avoided, then the crystal growth parameters should be adjusted to minimize it as much as possible. This is why a deeper understanding of the crystal growth and effects of the growth parameters of electron doped cuprates are necessary.

For the particular growth of NCCO the ideal growth conditions have been investigated and reported [21, 30]. A summary of the required atmosphere, pressure and power for the growth of NCCO for all dopant concentrations up to the solubility limit is given in Table 1.1. Most of these parameters were maintained for the crystal growth which concerns this thesis, any changes will be discussed in the appropriate Section.

While the TSFZ method has proven to be a reliable method for the growth of electron-doped superconductors, some unanswered issues still need to be addressed. Is the radial distribution of the dopant agent homogeneous or are there

differences in the outer and inner part of the rod? Are the superconducting properties of samples cut from a big crystal or directly from the as-grown rod equal for all parts of the rod? Do these properties change if the growth parameters are adjusted? To answer these questions the physical properties of two NCCO crystals with the particular dopings  $x = 0.125$  and  $x = 0.13$  were studied and they will be discussed separately in chapters 2 and 3. The specific growth conditions will be discussed in the next Section but they apply for all dopant concentrations grown in this work. In the last Chapter 4, other dopant concentrations will be discussed and a general conclusion will be made in Chapter 5.

### 1.3 Sample preparation: change in the growth rate

As mentioned in the previous Section, the conditions for a successful crystal growth of NCCO with the TSFZ method are very well established. While the oxygen atmosphere ensures the accurate oxidation state of the ions and control of the lamp power maintains the temperature of the system between the peritectic and eutectic point, another very important growth parameter has not been mentioned, the growth rate. Growth rate in the TSFZ method can be very easily manipulated by adjusting the velocity with which the stage and focal point of the lamps are moved upwards, also called pulling rate. From an analysis of a general crystal growth process, changes in the pulling rate can affect the transport of the reactants and their adsorption at the growth surface. The temperature at the liquid-solid interface is also affected because of the crystallization heat [58]. The pulling rate is also very important to avoid constitutional supercooling, a common problem when growing incongruent melting compounds [58]. Mechanical stirring of the molten zone is done by rotation of the rods, which assures uniform distribution of the reactants and heat convection. However, according to the diffusion crystal growth theory [59] the layer close to the crystallization front is less mobile and the solute transport is mainly diffusion controlled. This affects the supersaturation at the crystallization front. The amount of solute that will be deposited on the surface of a crystal in a supersaturated solution is given by

$$\frac{dm}{dt} = \left(\frac{D}{\delta}\right) A (c - c_0) \quad (1.1)$$

where  $dm$  is the mass of solute deposited over an area  $A$  in the time interval

$dt$ ,  $D$  is the diffusion coefficient of the solute,  $c$  and  $c_0$  are the bulk and interface concentrations of the solute, and  $\delta$  is the thickness of the diffusion layer next to the solid surface [58]. At supersaturation conditions the growth rate is limited by the reaction between the substrate and the surface [60]. The particles at the surface are not necessarily adsorbed immediately, they are mobile and can migrate on the surface until they find an energetically favorable crystallization site [61, 62].

The pulling rate is experimentally optimized for each material. For NCCO the reported growth parameters which yield the best results are given in table 1.2.

While these parameters apply for the general crystal growth of NCCO, they were mainly devised for the crystal growth of optimally doped and overdoped NCCO crystals. Since the present investigation focused on the underdoped regime, some disagreements were observed during the crystal growth under these conditions, particularly related to the growth rate. The main problem with a growth rate of 0.50 mm/h was the stabilization of the molten zone. If this growth rate was to be applied, the amount of flux required had to be larger than 0.45 g, which complicated the manipulation of the system during the first steps of melting and rotation. Additionally, during growth, small disturbances such as small changes in the atmosphere pressure or shaking of the feed rod, would destabilize the molten zone and the process had to be restarted. Additionally, to ensure a flat solid-liquid interface at the feed and seed rods, the rotation had to be 20/20 rpm, which was only a small adjustment of the already known parameters.

Taking these observations into consideration, it was decided to reduce the growth rate to 0.20 mm/h. This allowed for the use of flux pellets of  $\approx 0.45$  g. From direct observation of the growth process, the molten zone was easily stabilized and kept stable throughout the whole process. After the first 24 hours of growth, the surface of the crystal already showed signs of grain selection. In comparison, for a growth rate of 0.50 mm/h, the surface of the crystal showed

growth rate	0.5 mm/h
rotation feed/seed rods	20/(15 – 20) rpm
weight of the flux pellet	0.35 – 0.45 g
diameter of the starting rods	5 – 6 mm

Table 1.2: Summary of the growth parameters for a stable growth of NCCO. Adapted from [21].

several grains for at least 48 hours.

A straightforward explanation is that at slower pulling rates, the adsorption at the crystallization front can be more systematic. This means, that if the temperature at the crystallization front is reduced less rapidly, the particles at the diffusion layer are more free to find the adsorption site which most favors its attachment energy, e.g. a kink instead of a terrace [61]. At faster growth rates, some particles can be frozen at less favorable sites and thus promote the growth of dendrites or multiple grains due to constitutional supercooling [58]. Obvious disadvantages are that the slow growth rate process requires longer times to obtain a crystal and increase the need in gas supply. Despite this, the use of a slower growth rate for underdoped NCCO is advised.

Furthermore, it was noticed that the physical properties of samples grown at a slower pace showed some important differences from the formerly grown crystals with faster growth rates. A detailed characterization of the physical properties of the samples was done, particularly of NCCO  $x = 0.125$  and  $x = 0.13$ , as a function of growth rate. The crystal growth was performed in a commercial mirror furnace for CSI Corporation (Japan), type FZ-T-10000-H-VI-VP with four half-ellipsoidal mirrors. For the preparation of the polycrystalline materials and further details of the process refer to Ref. [21, 54]. The growth rates will be referred to as fast (fg) and slow (sg), for 0.50 mm/h and 0.20 mm/h, respectively. After the crystal growth, samples were cut according to the particular experiment requirements by the use of a wire saw. The orientation in the  $c$  and  $a$  axis was performed with a X-Ray Laue back scattering camera system with an accuracy of  $0.5^\circ$ . Samples will be described in each section if necessary.



## 2 NCCO $x = 0.125$

It is reported that, for NCCO, bulk superconductivity sets in at  $x = 0.13$  [20]. In order to observe how the structural and SC properties of NCCO are affected by the growth rate, the study of an NCCO sample with a dopant concentration close to the emergence of superconductivity is a suitable candidate for characterization. Two NCCO  $x = 0.125$  crystal rods were grown, one using a fast growth rate ( $x = 0.125 - fg$ ) and the other with a slow growth rate ( $x = 0.125 - sg$ ). From the as-grown rods a slab was cut along the diameter of the rod and then cut into five samples of approximately  $1 \times 1 \times 1$  mm. Figure 2.1 shows the five samples used for the investigation of magnetic susceptibility and X-Ray fluorescence, for each NCCO crystal rod. For simplicity only the samples of the fast grown crystal are shown. The samples for transport and neutron scattering measurements will be described in the corresponding section. As mentioned in Section 1.3 the samples were annealed according to their dopant concentration in an argon gas flow at  $910^\circ$  for 20 hours, followed by a cooling rate of 100 K down to room temperature. The characterization for each technique will be presented in separate sections: X-Ray fluorescence in Section 2.1, magnetic susceptibility in Section 2.2, neutron diffraction in Section 2.3 and transport measurements in Section 2.4.

### 2.1 X-Ray Fluorescence

X-ray fluorescence spectroscopy (XRF) is a non-destructive technique for the elemental analysis of various types of samples. The basic principle is widely used in many techniques. Because of the orbital arrangement of the electrons around the nucleus, each orbital level has a discrete energy level which varies according to the electrostatic attraction the electron feels to the nucleus. The required energy to remove an electron from its shell is the binding energy. When a sample is irra-

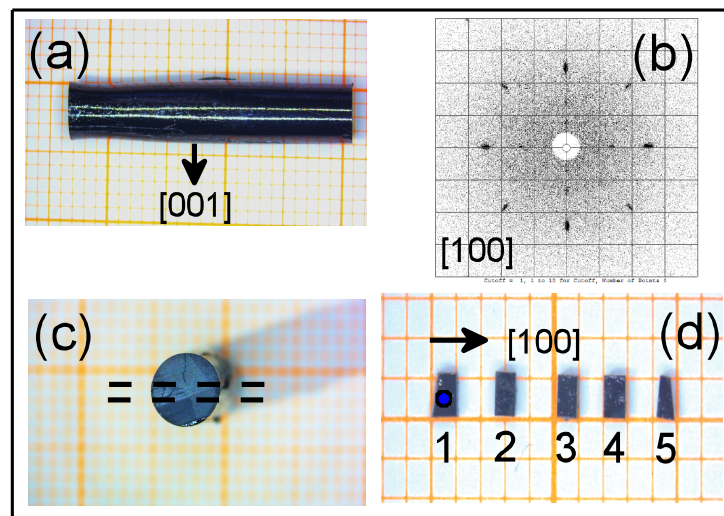


Figure 2.1: Illustration of the samples and correspondence to the as-grown rod. a) Lateral view of the as-grown rod. The vertical arrow depicts the direction of the  $[001]$  axis. b) Laue back scattering shows the  $[100]$  direction of the slab obtained from the crystal rod. c) Top view of the as-grown rod. The dashed lines indicate how the slab was cut from the rod. d) Samples 1 – 5 for the fast grown crystal. Samples 1 and 5 correspond to the outermost part of the rod and sample 3 to the middle part. The  $[100]$  axis is on the plane of the paper and the  $[001]$  axis points outside the paper, represented by the blue dot on sample 1.

diated by an x-ray beam, and if the incident photon has greater energy than the binding energy of the inner shell electron, the electron can be ejected. This electron leaves a vacancy behind which is filled by a second electron from an outer orbital level. Since the energy of the second electron is higher, it needs to release energy as it falls from a higher electron shell to a lower one, which is equivalent to the difference in energy between the two electron shells determined by the spacing between them. Since the spacing between the orbital shells of an atom is unique to each element, the excess energy which is released has a characteristic wavelength of the atomic energy levels and it is used for elemental identification [63, 64].

By using an X-ray focusing lens, XRF analysis of small regions is possible as the well-known technique of micro-XRF analysis. In XRF all elements having  $Z > 3$  can be detected and the X-ray penetration depth can be in the range of  $\mu\text{m}$ . The detection limit is in the range of ppm, although it depends on the element. Additionally XRF can be used to determine quantitative elemental compositions.

The experimental set up consists of an X-ray source, the crystal spectrometer, and the detection system. The fluorescent X-rays from the sample pass through a primary collimator. The analyzing crystal is oriented to reflect from a set of crystal planes of known  $d$ -spacing, which reflects one X-ray wavelength  $\lambda$  at a given angle  $\theta$  in accordance with Bragg's law. The analyzing crystal is rotated at half the angular speed of the detector to match the corresponding angle  $\theta$  for each wavelength, so the different wavelengths from the fluorescent X rays are reflected one by one. The intensity of each wavelength is then recorded by the detector [63].

In comparison to other techniques such as EDX, XRF has a higher energy resolution and so it has less problems with peak overlapping of transition elements causing analysis difficulties. Also, EDX can only analyse elements with  $Z > 10$ .

The XRF analysis in this work were conducted at the crystal growth facilities of the department of physics from the École Polytechnique Fédérale de Laussane (EPFL) with the Orbis PC Micro EDXRF analyzer system.

An Rh micro-focus X-ray tube was operated at 20 kV and 700  $\mu\text{A}$ . A Apollo XRF-ML50 silicon drift detector was employed to detect x-rays. The samples, 1–5 of the  $x = 0.125$  fast and slow grown crystals, were mounted with the [001] axis vertical as shown in Fig.2.1(d) on a high precision XYZ sample stage and XRF

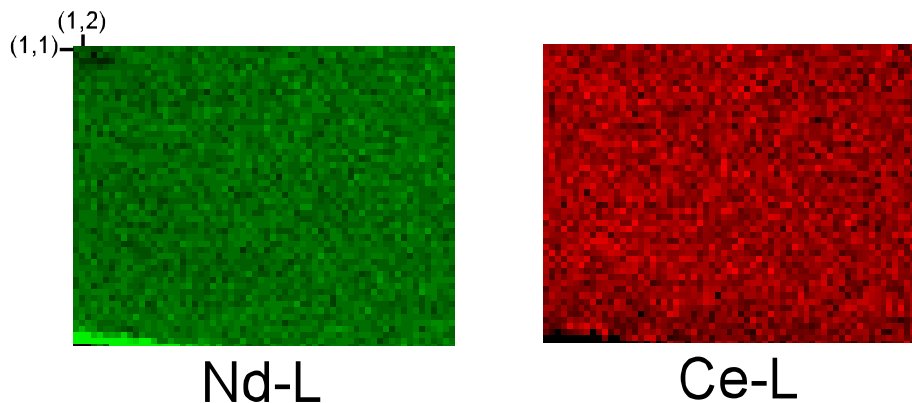


Figure 2.2: Elemental image created from spectra obtained by XRF measurement of sample 1 from the  $x = 0.125 - fg$  single crystal. Analyzed area of  $1 \text{ mm} \times 1 \text{ mm}$ , step  $15.7 \mu\text{m}$ , acquisition time  $2 \text{ s/step}$ . **Left:** 2D scanning map of the L-lines for Nd. The numbers are an example of the coordinates in the spectra. **Right:** 2D scanning map of the L-lines for Ce.

mapping was performed over the total upper surface area of the sample. The samples were scanned with a step size of  $15.7 \mu\text{m}$ . XRF analysis was performed for  $2 \text{ s}$  at each position.

### 2.1.1 Results

For a surface area of approximately  $1 \text{ mm} \times 1 \text{ mm}$  per sample which was analyzed with a step size of  $15.7 \mu\text{m}$ , a total of 3200 ( $= 64 \times 50$ ) spectra were obtained. To evaluate the concentration of Nd and Ce, fluorescent element intensity lines were measured for the total of the 10 samples. For simplicity only an example is shown in Fig.2.2.

Each spectra in the 2D map has an intensity value which is directly proportional to the atomic percentage At% of the corresponding element. In other words, the bright spots correspond to a higher concentration of the element and darker points to lower concentration. The At% average was taken from the 3200

$x = 0.125$ fast growth	
sample	dopant concentration $x$
1	$0.1268 \pm 0.0032$
2	$0.1271 \pm 0.0032$
3	$0.1276 \pm 0.0035$
4	$0.1253 \pm 0.0032$
5	$0.1292 \pm 0.0032$
mean	$0.1270 \pm 0.0032$

Table 2.1: Calculated dopant concentration from the elemental analysis of samples 1 – 5 of the  $x = 0.125 - fg$  crystal.

$x = 0.125$ slow growth	
sample	dopant concentration $x$
1	$0.1154 \pm 0.0037$
2	$0.1198 \pm 0.0034$
3	$0.1207 \pm 0.0037$
4	$0.1216 \pm 0.0034$
5	$0.1178 \pm 0.0034$
mean	$0.1191 \pm 0.0035$

Table 2.2: Calculated dopant concentration from the elemental analysis of samples 1 – 5 of the  $x = 0.125 - sg$  crystal.

spectra of the L-lines of Ce and Nd and the dopant concentration of each sample was calculated. The results are presented in tables 2.1 and 2.2

It should be considered that these are not the absolute values of dopant concentrations, since a calibration curve was not done. However, a comparison between the measured dopant concentration of the two different batches of samples can still be performed, considering their relative differences, ratios and the overall observation of their superconducting properties. For a better visualisation of the distribution of the dopant concentration along the diameter of the single crystal rod, an illustration is shown in Fig.2.3. Two main differences are evident from this representation. First, the average dopant concentration of the fast grown sample is higher than the Ce concentration of the slow grown samples and second the radial distribution of Ce of the slow grown samples has a slight gradient towards

the center of the rod. The average Ce concentration in the fast grown samples is approximately 2.14% larger than in the slow grown samples. Furthermore, for the fast grown samples, the dopant concentration does not show much change along the diameter, with only a minimal decrease close to the samples in the center, samples 3 and 4. On the other hand, the Ce concentration in the samples of the slow grown crystal shows a radial gradient. Samples from the outer part of the crystal rod have a lower concentration of Ce, and the samples from the inner part of the crystal have a higher dopant concentration. Similar gradients in the Ce concentration have been reported in the literature [57].

Since there is no fundamental difference in the preparation of the starting materials and the growth conditions are the same in both growth processes with the exception of the growth rate, the difference in the dopant concentration is attributed to the growth parameter of the pulling rate. While this observation can seem counterintuitive, the process should be analysed from a microscopic point of view. As mentioned in Section 1.3 the mechanical stirring of the melting zone assures a relatively uniform composition. At supersaturation conditions the growth is limited by the reaction between the growing blocks in the liquid and the solid surface of the seed rod. This is a diffusion limited process and the flux-seed rod interface is less mobile than the rest of the liquid. At the growth front the particles are in a continuous process of adsorption-desorption and this layer has an abundance of growth units [58]. The pulling rate can also be thought of as the cooling rate of the crystallized rod. An increase in the pulling rate forces the solid-liquid interface into more supercooled liquid [58]. If the growth interface is rich in growth units and they are limited in mobility, a fast cooling rate will freeze more units at the growth front than at a slow cooling rate. This explains the higher concentration of Ce in the fast grown samples.

The difference in the radial distribution of Ce between these two crystals can also be a consequence of this process. The growth units, although not as mobile as the rest of the liquid, can diffuse throughout the solid-liquid interface until they find an energetically favorable site. If a slow pulling rate favors a slight dopant concentration gradient towards the center of the rod, the edge of the crystal can be considered a less energetically suitable crystallization site. The edge of the crystal rod is an area where three different phases interact, the solid-liquid interface of the seed rod and the molten zone plus the additional interaction with the growth

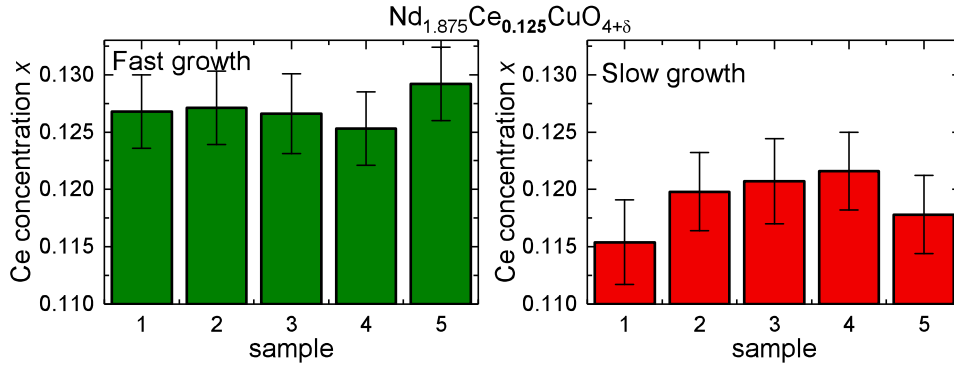


Figure 2.3: Measured dopant concentration for samples 1 – 5 of the two  $x = 0.125$  single crystals. **Left:** Samples from the fast grown  $x = 0.125$  single crystal. **Right:** Samples from the slow grown  $x = 0.125$  single crystal.

atmosphere. The growth units at the very edge of the growth front interact with the solid interface, the liquid flux and the gas atmosphere. Because of the surface tension at the liquid-gas interface the surface energy of the growth units will be higher, i.e. at the perimeter of the rod the growth units are less surrounded by the flux. This means that the area at the center of the rod is more favorable in terms of surface energy and thus it is preferred as a growth site. If the cooling rate is slow enough the particles can migrate to an attachment site which decreases their surface energy, and so a slight tendency to migrate to the center of the rod can be expected.

## 2.2 Magnetic susceptibility

The DC magnetic susceptibility of the samples was measured to detect their superconducting transition temperature  $T_c$ . As superconductors are perfect diamagnets in the superconducting state, the transition can be detected with this method. The  $T_c$  was taken at the half height of the diamagnetic transition. Zero field cooling (ZFC) measurements were performed in a Quantum Design SQUID magnetometer systems (MPMS XL-/) with an applied field of 2 Oe parallel to the [001] crystallographic axis. Additionally, in order to estimate the SC volume fraction of our samples the DC susceptibility of a lead reference sample was measured. The reference samples were prepared manually and had the same dimensions and shape as the original NCCO single crystal. The estimated SC volume

fraction corresponds to the ratio of the diamagnetic transition of the sample to the reference. Furthermore the AC susceptibility was also measured. This is defined as

$$\chi = \frac{\partial M}{\partial H} = \chi' + i\chi'' \quad (2.1)$$

where the real part  $\chi'$  describes the shielding of the magnetic field and the imaginary part  $\chi''$  describes fluctuations in magnetic flux. In the superconducting state  $\chi' = -1$ . The measurement of  $\chi'$  was less relevant in this work. For the AC susceptibility measurements the focus was on the imaginary component  $\chi''$  as means to detect inhomogeneities in the crystal lattice. A single peak was taken as a sign of homogeneity whereas the presence of satellite peaks would be indication of sample defects.

## 2.2.1 Results

In Fig.2.4 the temperature dependence of the normalized DC susceptibility and a graphic illustration of the SC volume fraction of the five  $x = 0.125 - fg$  samples are shown.

All  $x = 0.125 - fg$  showed superconductivity, at least in part of the sample. Unlike the superconducting transition of the optimally doped NCCO, the transition of these samples is gradual with a maximum transition width  $\Delta T_c = 13.6$  K.

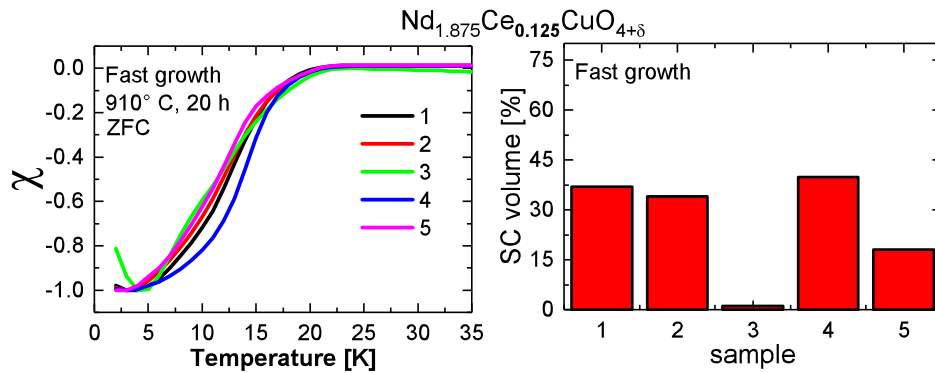


Figure 2.4: **Left:** Normalized temperature dependence of the DC susceptibility  $\chi(T)$  for samples 1 – 5 of the  $x = 0.125 - fg$  crystal. **Right:** Representation of the volume fraction of superconductivity of each NCCO sample as a function of a lead reference sample.

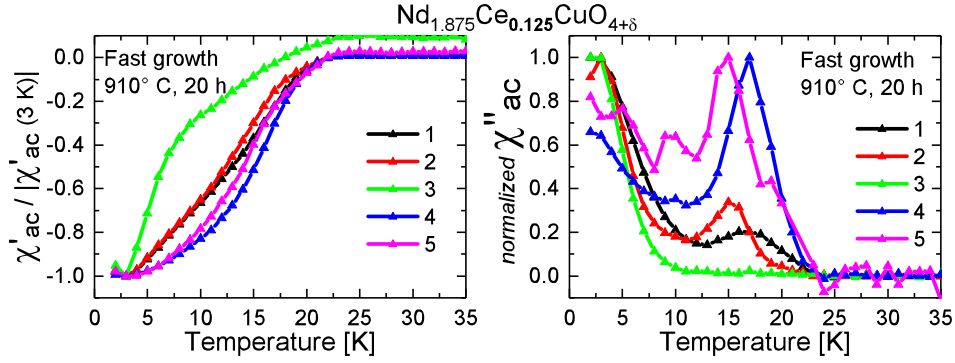


Figure 2.5: Normalized temperature dependence of the AC susceptibility  $\chi(T)$  for samples 1 – 5 of the  $x = 0.125 - fg$  crystal. **Left:**  $\chi'(T)$  normalized to  $\chi'(3\text{ K})$ . **Right:**  $\chi''(T)$  normalized to its maximum.

Sample 3 still shows a remanent of the magnetisation of Nd, which is visible as an upturn in the susceptibility below  $T = 3\text{ K}$ . Accordingly, the SC volume fraction of the five samples is shown on the right side of Fig.2.4. Their average superconductivity volume is  $26 \pm 16\%$ . However, large variation is observed. Sample 3 is the least superconducting one with only 0.03 to 1 of the SC volume fraction of sample 4, the one which shows the most superconductivity and also the highest  $T_c$ .

The AC susceptibility of the five  $x = 0.125 - fg$  samples is depicted in Fig.2.5. The susceptibility  $\chi'$  is very similar to the DC susceptibility from Fig.2.4, however the imaginary component  $\chi''$  shows more irregularities. Samples 1 and 2 have a small peak at 15 K and 17 K, respectively and the susceptibility continues to increase with decreasing temperature. The  $\chi''$  susceptibility of sample 3 is flat down to 10 K, it then has an upturn and increases constantly down to 3 K. Sample 4 only has a single peak at 17 K and sample 5 shows many irregularities above 20 K. However, they are considered a measurement artifact due to the height ratio to the highest peak and a lack of more measured points.

Furthermore, the temperature dependence of the ZFC DC and AC susceptibilities of the  $x = 0.125 - sg$  crystals, are shown in Figs. 2.6 and 2.7, respectively. In the DC susceptibility curves, the superconducting transition of the slow grown crystals is slightly less broad than the transition of the fast grown crystals and no sample shows remanence of Nd magnetisation. The transition temperature  $T_c$  of the  $x = 0.125 - sg$  samples is higher and saturates below 5 K. On the right side

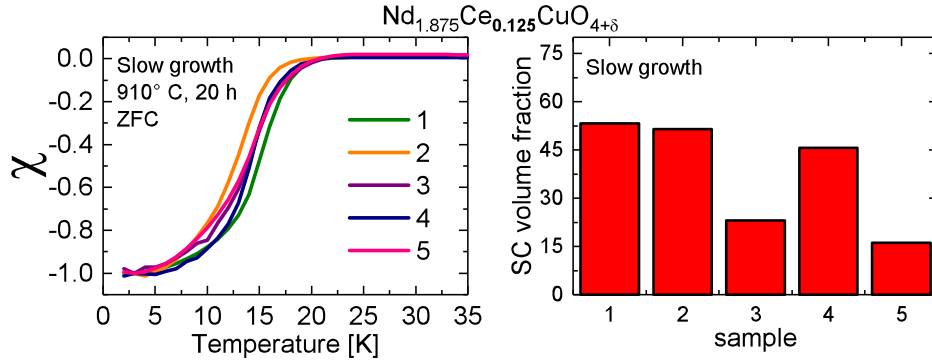


Figure 2.6: **Left:** Normalized temperature dependence of the DC susceptibility  $\chi(T)$  for samples 1 – 5 of the  $x = 0.125 - sg$  crystal. **Right:** The volume fraction of superconductivity of each NCCO sample as a function of a lead reference sample.

of Fig.2.6, the SC volume fraction of the slow grown crystals is represented. In comparison with the  $x = 0.125 - fg$  samples, the volume fraction is increased. The average volume of superconductivity is  $38 \pm 17\%$ . Interestingly, the middle sample, i.e. sample 3, also shows a decrease in its SC fraction similar to the fast grown crystals. However, it is not the sample with the least percentage of superconductivity, which in this case corresponds to sample 5. Despite the fact that both samples 1 and 5 correspond to the most outer part of the crystal rod, they do not show similar behavior and have a difference of 1 K in  $T_c$  and the SC volume fraction of sample 5 is almost 3 times smaller than that of sample 1. Since the SC volume fraction is estimated from comparison to a manually-prepared reference sample, a source of error could be a shape mismatch between the NCCO sample 5 and its corresponding lead reference sample.

The  $\chi''$  of the slow grown samples also shows some irregularities, however, all samples have a maximum close to their superconducting transition. The peak at 20 K of sample 3 seems to be split but due to a lack of points it is difficult to confirm this, thus this is considered an artifact of the measurement. Samples 2 and 5 show a second slight susceptibility increase at low temperatures but it is more pronounced in sample 5. These two samples have the smallest  $T_c$ .

After an observation of the general superconducting properties of the  $x = 0.125 - fg$  and  $x = 0.125 - sg$  crystals, a direct comparison of the  $T_c$  and the width of the transition  $\Delta T_c$  between the two sets of samples is shown in Fig.2.8.

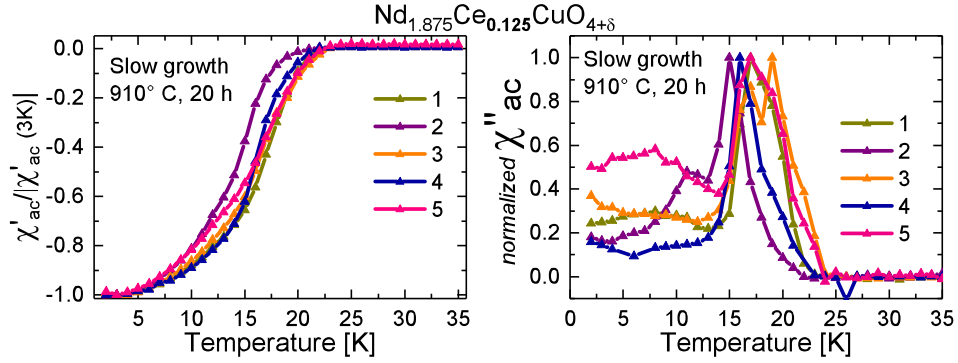


Figure 2.7: Normalized temperature dependence of the AC susceptibility  $\chi(T)$  for samples 1 – 5 of the  $x = 0.125 - sg$  crystal. **Left:**  $\chi'(T)$  normalized to  $\chi'(3\text{K})$ . **Right:**  $\chi''(T)$  normalized to its maximum.

We define the width of the transition as  $\Delta T_c = T(0.05) - T(0.95)$ , taken from the normalized magnitude of the DC superconducting transition. The average  $T_c$  of the fast grown samples is  $T_c = 12.1 \pm 1\text{K}$  with a transition width  $\Delta T_c = 13\text{K}$ . On the other hand, the slow grown samples show a higher  $T_c$  with slightly more than 1.5 K and the transition width is narrower,  $T_c = 13.7 \pm 0.8\text{K}$  and  $\Delta T_c = 11.4\text{K}$ .

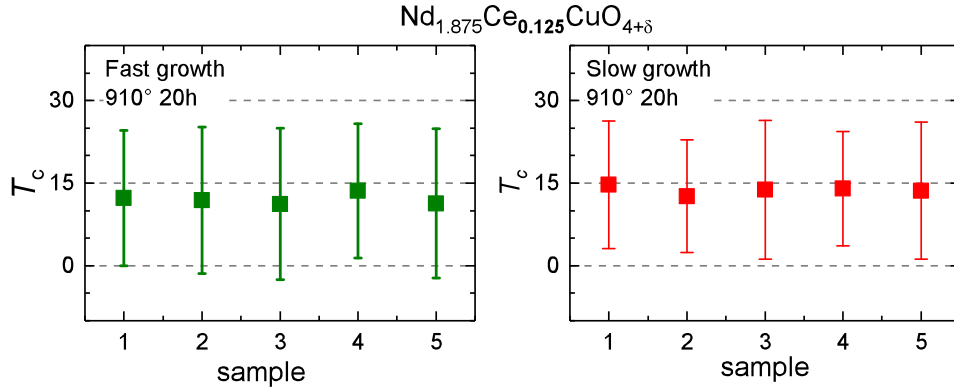


Figure 2.8: Graphic representation of the  $T_c$  and  $\Delta T_c$  for **Left:**  $x = 0.125 - fg$  single crystals. **Right:**  $x = 0.125 - sg$  single crystals. The  $\Delta T_c$  is denoted by the error bar. The dotted lines are included as a guide for visualization.

The magnetic field dependence of the sample magnetization was also measured to confirm the absence of further inhomogeneities which can result from the annealing treatment [30]. The magnetisation curves  $M - H$  for all samples from  $-600\text{Oe}$  to  $600\text{Oe}$  at  $2\text{K}$  are shown in Fig. 2.9. The hysteresis loops can be used

to calculate the critical current density  $J_c$ . The Bean critical state model indicates that the difference between the upper and lower branches of the  $M - H$  loops at a given temperature is proportional to the critical current density  $J_c(H) = \frac{\Delta M(H)}{d}$  where  $d$  is characteristic of the sample shape [65]. For a rectangular sample an adjustment to the formula must be done [66].

sample	fast growth $J_c$ [A/cm <sup>2</sup> ]	slow growth $J_c$ [A/cm <sup>2</sup> ]
1	13.0	59.7
2	n.m.	42.0
3	0.4	13.2
4	38.5	43.7
5	9.8	10.6

Table 2.3: Critical current density for all samples of  $x = 0.125$  from the fast and slow growth batches. For sample  $x = 0.125$  number 2 the  $H - M$  curve was not completed and thus the corresponding  $J_c$  is not shown.

Observations resulting from examination of Table 2.3 and a simple visual comparison of the hysteresis loops determinate that the critical current density in the slow grown samples is higher. Moreover, despite the differences in the superconducting properties between the fast and slow grown crystals, all samples have a critical field  $H_{c1} \approx 10$  Oe. Hysteresis loops have been useful for detecting sample defects from the reduction process in overdoped NCCO crystals attributed to the insertion of oxygen in the apical sites [30]. No inhomogeneities of this type were detected in the  $x = 0.125 - fg$  or  $x = 0.125 - sg$  samples.

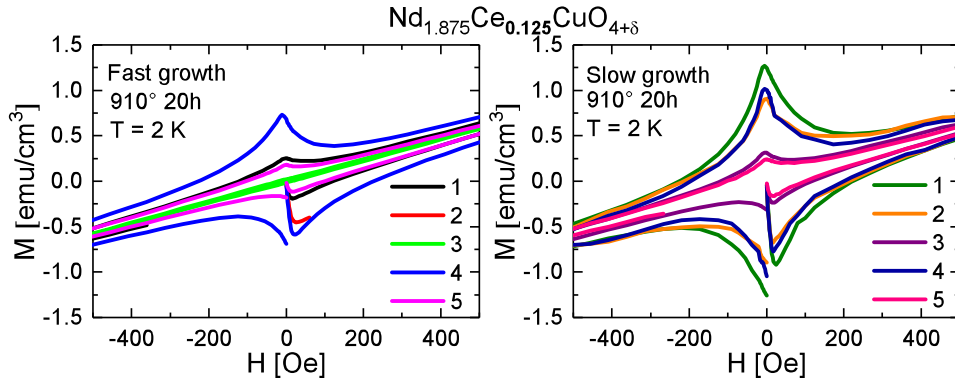


Figure 2.9: Magnetization curves recorded at 2 K of **Left:**  $x = 0.125 - fg$  single crystals. **Right:**  $x = 0.125 - sg$  single crystals .

Further discussion of these results will be conducted in Section 2.5, but a preliminary conclusion is that the five slow grown samples have better superconducting properties, with an average higher  $T_c$ , SC volume and critical current  $J_c$  than those of the fast grown samples. However, these observations seem to contradict the results from XRF which indicate that the fast grown samples have a higher Ce concentration and thus their  $T_c$  should be higher.

## 2.3 Elastic neutron scattering

The origins of any material's properties are hidden in their atomic or molecular structure. Materials characterization is a very broad field of research and there is an extensive list of techniques which can be used for this purpose, but very few methods can give information about both structure and dynamics on the atomic length scale of the studied material. For many years, neutrons have been one of the most important tools to measure the physical properties of solids, especially their magnetic properties. A thorough discussion of neutron scattering is beyond the scope of this thesis, however, the relevance of the technique and some important terminology will be discussed.

Four years after the discovery of the neutron in 1932, it was experimentally proven that neutrons could be diffracted [67]. But it wasn't until the emergence of multiple facilities of neutron research and the development of the first neutron diffractometer that this field expanded and became a widely used technique [68]. The possibility to use neutrons experimentally and the advantages of such characterization methods arise because of the fundamental properties of the neutron, given in Table 2.4.

Because of the relatively high mass of the neutron, the resulting wavelengths

properties of the neutron	
mass	$m = 1.675 \times 10^{-27}$ kg
charge	0
spin	$\frac{1}{2}$
magnetic dipole moment	$\mu_n = -1.913 \mu_N$

Table 2.4: Basic properties of the neutron [69].

of monochromatic beams are in the range of Angstroms, which allows for structural studies of crystalline solids [69]. Since neutrons have a zero charge, they do not interact with electrons and can more easily travel through matter interacting solely with nuclei [68, 69]. The energy of thermal neutrons permits the study of dynamics and the measure of excitation processes. Also, because of their own magnetic moment, neutrons feel the magnetic force of unpaired electron spins as they approach or pass close to another magnetic particle. This means that from neutron scattering measurements, information can be obtained not only on spin systems and their regular arrangement, but also on the energies of their magnetic excitations [68, 69].

Neutrons have two ways of interacting with matter. First, with nuclei via nuclear force which occurs within a very short range. This interaction can be characterized by the parameter  $b$ , the scattering length which is the probability of interaction between neutron and nuclei and varies across the periodic system without a particular pattern and even has different values for isotopes of the same element. Typical values of  $b$  are on the order of  $1 \times 10^{-12}$  cm. With neutron scattering it is possible to study light isotopes which are barely detected with other methods. Second, with magnetic moments via dipole-dipole interaction. As already mentioned, this allows for the study of magnetic properties of solids [70].

There are two methods to produce neutrons, from a nuclear reactor and from a spallation source. In the first case, the induced fission of  $^{235}\text{U}$  by the absorption of one neutron breaks one atom into two lighter nuclei, 2 – 3 neutrons and energy (about 2 MeV) are typically released [68]. As for the spallation source, protons with energies from 500 MeV to 3 GeV hit a heavy target, and neutrons are produced [68, 71] by the spallation of the target nuclei. Due to the high velocity and energies which the neutrons carry after their generation from either type of source, they need to be slowed down or moderated. This is done, for example, by collision with protons, e.g. in cooling water. Neutrons can be classified by their energy from ultra-cold to ultra-hot, although most typically used are the thermal, 5 – 100 meV, and cold neutrons, 0.1 – 10 meV. The experiments performed in this thesis were done with cold neutrons from a reactor source.

To understand the scattering process in a simple case, a neutron beam incident on a single atom is considered. The range of the nuclear force is much smaller than the neutron wavelength and so the scattering is point-like. The incident

plane wave on a nucleus is

$$\phi_i = e^{ikz} \quad (2.2)$$

The origin is considered at the position of the nucleus,  $z$  is along the direction of the wavevector of the incident beam,  $k = \frac{2\pi}{\lambda}$ . The spherically symmetric scattered wave at that point  $r$  will be

$$\phi_s = - \left( \frac{b}{r} \right) e^{ikz} \quad (2.3)$$

where  $b$  is the scattering length mentioned before. The scattering length is related to the scattering cross-section<sup>1</sup> by  $\sigma = 4\pi b^2$ .

For the scattered neutrons, two processes are possible, elastic or inelastic scattering. An elastic scattering event occurs when total energy and momentum are conserved, but in the case of inelastic scattering the neutron loses or gains energy [68]. The experiment presented in this work is of the elastic scattering type, diffraction on a single crystal. Momentum and energy conservation are given by

$$Q = k_f - k_i \quad (2.4)$$

$$E_i - E_f = \frac{1}{2}mv_i^2 - \frac{1}{2}mv_f^2 = \frac{1}{2m}\hbar^2(k_i^2 - k_f^2) = 0 \quad (2.5)$$

where  $Q$  is the scattering vector,  $k_i = k_f$  are the initial and final wave vectors [68, 71]. The scattering vector can also be written as

$$Q = 2k \sin \theta = \frac{4\pi \sin \theta}{\lambda} \quad (2.6)$$

from a scattering triangle representation [72]. In elastic scattering the moduli of the wavevectors are equal and the scattering angle  $2\theta$  is comprised between the incident and scattered beam. Diffraction is a type of scattering where the incident wave interacts with the whole assembly of atoms and the scattered waves interfere with each other [67, 72]. In the scattering condition, the scattering vector  $Q$  must be perpendicular to the scattering planes and  $Qd = 2\pi n$  where  $d$  is the

---

<sup>1</sup>The cross-section  $\sigma$ , is the effective area of the atom or sample as if it were able to scatter all incoming neutrons. It is calculated as the ratio between the outgoing current of scattered neutrons and the incident neutron flux [67].

distance between the scattering planes and  $n$  is an integer. Combining this with equation 2.6, we obtain the Bragg's equation

$$n\lambda = 2d \sin \theta \quad (2.7)$$

The case discussed above assumes the use of a monochromatic beam, however, it is also possible to perform diffraction measurements by using white radiation and a large area detector in the backscattering direction, also known as the back-reflection Laue technique. Since a wider range of wavelengths is provided, the Bragg condition is fulfilled for more than one reciprocal lattice point and the reciprocal lattice points of the crystal are recorded in a spot pattern [67, 71]. This technique is extremely useful for a preliminary alignment of the samples before a scattering experiment. Moreover it allows confirmation of the quality of the sample, i.e. that the samples are real single crystals. This is achieved by analysis of the Laue spot pattern; multiple grains or twinning are easily detected by the observation of doubled or deformed spots on the scattering pattern.

Neutron diffraction was used to study the crystal and magnetic structures of two NCCO single crystals as a function of temperature, one crystal of each growth batch. The size of both samples was approximately  $2.5 \times 2.5 \times 1 \text{ mm}^3$ . The sample weights were 63.6 mg and 60.4 mg for the NCCO  $x = 0.125 - fg$  and  $x = 0.125 - sg$  samples, respectively. The samples were aligned with the Neutron-Laue camera at the Heinz Meier-Leibniz Zentrum and it was corroborated that the samples are single crystals. Figure 2.10 shows a Laue picture of the  $x = 0.125 - fg$  crystal as an example.

The neutron diffraction experiments were performed at the neutron source Heinz Meier-Leibniz Zentrum for neutron research located in Garching. Using the triple-axis spectrometer MIRA in the two-axis mode with fixed incident neutron energy of  $E_i = E_f = 5.2 \text{ meV}$  ( $k_i = 1.59 \text{ \AA}^{-1}$ ). Contamination for higher order reflections was suppressed using a Be filter. The detector used was a  $\text{He}^3$  finger detector. Samples were mounted with the  $[001]$  axis vertical, so that the scattering plane was  $(hk0)$ .

The structural reflection  $(1, 1, 0)$  was measured at different temperatures to control the orientation of the sample, measure the lattice constant and to monitor its temperature dependence.



Figure 2.10: Laue spot pattern of the NCCO  $x = 0.12 - fg$  single crystal aligned in the  $[110]$  axis. This picture was taken with the neutron Laue camera at the Heinz Meier-Leibniz Zentrum.

The structure factor for doped NCCO samples vanishes at  $(\frac{1}{2}, \frac{1}{2}, 0)^2$ . The magnetic Bragg reflections  $(\frac{3}{2}, \frac{1}{2}, 0)$  and  $(\frac{1}{2}, \frac{3}{2}, 0)$  were measured for the  $x = 0.125 - fg$  sample and the  $(\frac{3}{2}, \frac{1}{2}, 0)$  reflection for the  $x = 0.125 - sg$  sample, by performing  $Q$  scans along the  $[hh0]$  direction. A representative example of the measured nuclear and magnetic intensities is shown in the right panel of Fig. 2.11. These reflections were measured in a temperature range of 4 K – 120 K.

### 2.3.1 Results

As preliminary characterization, the DC susceptibility of the two samples was performed. This is shown in Fig. 2.11. Their transition temperatures are 11.9 K and 13.4 K for the fast and slow grown samples, respectively. These values coincide very well with the average transition temperature of the smaller samples described in Section 2.2.

The structural Bragg reflections of the two single crystals were measured at different temperatures and their peaks, fitted to a Gaussian distribution, are shown in Fig. 2.12. From these scans the lattice constant and corresponding correlation length  $\xi/a$  were calculated. This is summarized in Table 2.5. The lattice constant  $a$  of the  $x = 0.125 - fg$  is  $1.5 \times 10^{-3} \text{ \AA}$  larger than the lattice constant of the

<sup>2</sup>The magnetic reflections of NCCO follow a set of selection rules [73].

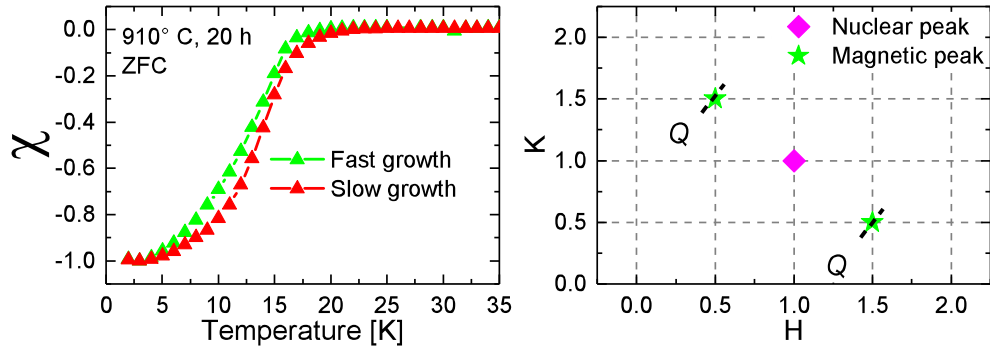


Figure 2.11: **Left:** Zero field cooling DC magnetic susceptibility of the two samples used for the neutron diffraction experiments. Their description is given in the text. **Right:** Graphic representation of the measured nuclear and magnetic peaks of the  $x = 0.125 - fg$  and  $x = 0.125 - sg$  single crystals. The dashed lines represent the scan direction.

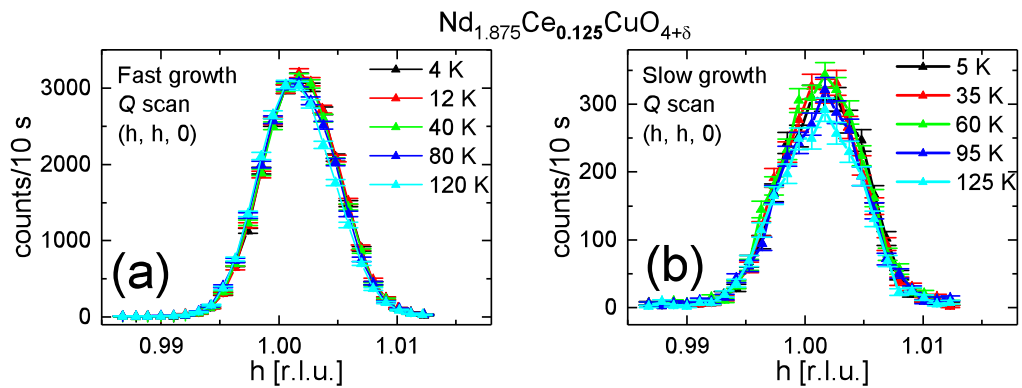


Figure 2.12: Two axis  $Q$ -scans along the  $[h, h, 0]$  direction for the two annealed  $NCCO$   $x = 0.125$  single crystals at different temperatures. (a) Fast grown sample. (b) Slow grown sample.

$x = 0.125 - sg$  single crystal. In Fig. 2.12 (b) a slight variation of the peak intensity for the slow grown sample is observed. However, from the temperature scans performed with the Neutron Laue camera, no evidence of structural transition was detected.

Furthermore, in Fig. 2.13 the magnetic Bragg peaks of the  $(1.5, 0.5, 0)$  and  $(0.5, 1.5, 0)$  reflections for the fast grown sample are shown. Figure 2.14 summarizes the temperature dependence of their integrated intensities. The  $Q$  scans were done with and without the Be filter to monitor the contribution of the higher

parameter	fast growth	slow growth
lattice constant [ $\text{\AA}$ ]	3.949	3.9475
correlation length $\xi/a$	192.5	177.6

Table 2.5: Lattice constant and correlation length of the two single crystals.

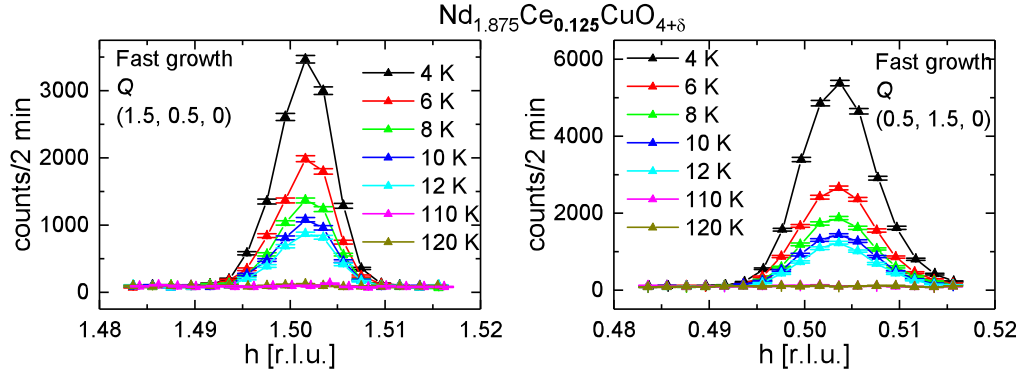


Figure 2.13: Two axis  $Q$ -scans along the  $[h, h, 0]$  directions through the corresponding Bragg peaks for the NCCO  $x = 0.125 - fg$  single crystal at different temperatures. (a)  $(1.5, 0.5, 0)$  reflection. (b)  $(0.5, 1.5, 0)$  reflection.

order reflections and possible structural background. The temperature dependence is shown on a logarithmic scale for a better appreciation of changes in the intensity. Additionally the insert in Fig. 2.14 shows the same intensities on a linear scale for comparison. The same behavior was observed for the  $(0.5, 1.5, 0)$  reflection.

The intensity of the  $(1.5, 0.5, 0)$  and  $(0.5, 1.5, 0)$  magnetic reflections is highest at the lowest temperature, at 4 K. Similar increase in the intensity at low temperatures has been reported and attributed to the polarization of the Nd moment by strong Cu–Nd interactions [73]. As the temperature increases the intensity of the magnetic reflections decreases monotonically and vanish at  $110 \pm 10$  K for  $(1.5, 0.5, 0)$  and at  $120 \pm 10$  K for  $(0.5, 1.5, 0)$ . These temperatures are slightly lower than the Néel temperature reported in the literature [26]. At 4 K the corresponding correlation lengths of the  $(1.5, 0.5, 0)$  and  $(0.5, 1.5, 0)$  reflections are  $\xi/a = 208.3$  and  $\xi/a = 156.5$ , respectively. These results are indication of long range AF order. The change of the correlation length with increasing temperature is depicted in Fig. 2.15. No significant change is seen up to the highest temperature. Ad-

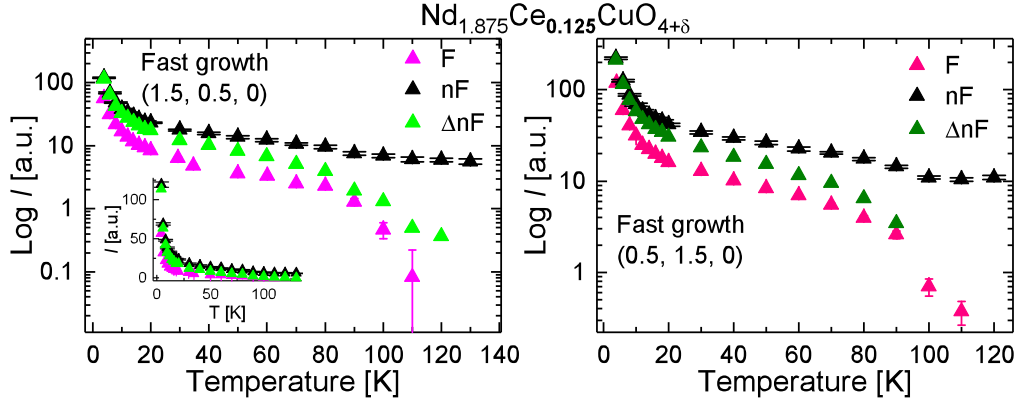


Figure 2.14: Temperature dependence of the integrated intensity  $I$  of the  $(1.5, 0.5, 0)$  and  $(0.5, 1.5, 0)$  magnetic reflections of the  $NCCO_{x=0.125}$  –  $fg$  single crystal, shown in a logarithmic scale. The measurements were taken with and without the Be filter, F and nF respectively.  $\Delta nF = I(T) - I(T_{max})$ . **Left:**  $(1.5, 0.5, 0)$ . The insert corresponds to the linear scale of the integrated intensity. **Right:**  $(0.5, 1.5, 0)$ .

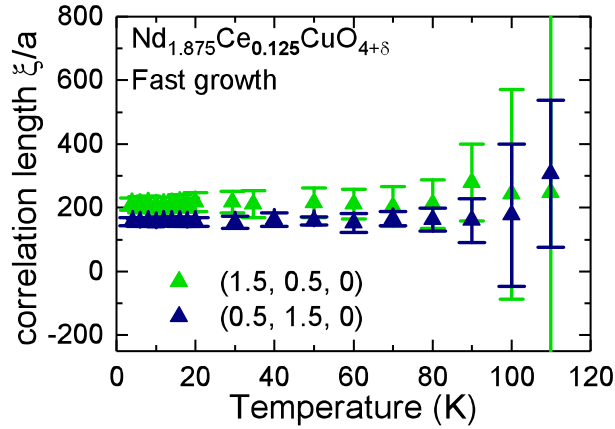


Figure 2.15: Temperature dependence of the correlation length  $\xi/a$  of the  $(1.5, 0.5, 0)$  and  $(0.5, 1.5, 0)$  magnetic reflections of the  $NCCO_{x=0.125}$  –  $sg$  single crystal.

ditionally, the rocking curves of the  $(1.5, 0.5, 0)$  and  $(0.5, 1.5, 0)$  reflections were measured and a mosaicity of  $0.45^\circ$  and  $0.4^\circ$  respectively was observed. These values are an indication of very good crystal quality.

For the  $x = 0.125$  –  $sg$  sample, the corresponding measurement of the magnetic

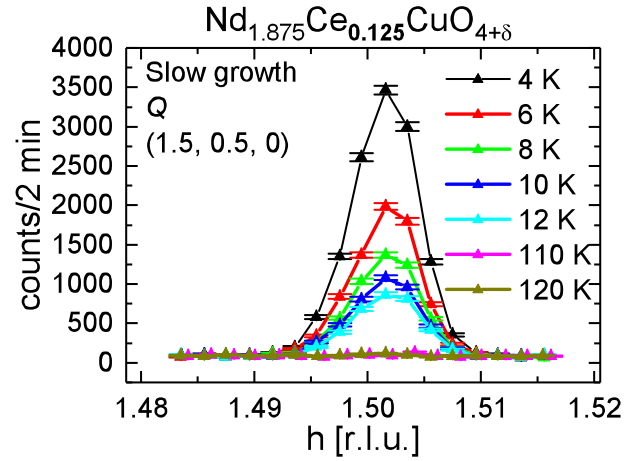


Figure 2.16: Two axis  $Q$ -scans along the  $[h, h, 0]$  direction for the  $(1.5, 0.5, 0)$  Bragg peak for the NCCO  $x = 0.125 - sg$  single crystal at different temperatures.

reflection  $(1.5, 0.5, 0)$  and its temperature dependence are shown in Figs. 2.16 and 2.17. The temperature dependence of the peak intensity shows similar behavior to the fast grown sample. The maximum intensity is seen at the lowest temperature and it decreases monotonically as temperature increases until the peak vanishes at  $80 \pm 10$  K.

From the FWHM the correlation length per unit cell was calculated. At  $T = 4$  K the correlation length was  $\xi/a = 214.7$ . No significant change with temperature was observed up to 80 K, where the intensity fades.

These results reveal two important differences between the fast and slow grown samples. The magnetic reflections of the fast grown sample persist up to  $120 \pm 10$  K while for the slow grown sample, the measured magnetic reflection fades at  $80 \pm 10$  K. This implies that the fast grown crystal is more magnetic than the slow grown sample. The temperatures where magnetic reflections vanish can be considered a guide to approach towards the Néel temperature of the samples, since the observation of a magnetic peak is related to long range AF order. Considering this, the fast grown crystal has a higher  $T_N$  than the slow grown crystal, although both crystals should have the same nominal dopant concentration and thus similar Néel temperatures. A second difference is in the in-plane lattice constants  $a$ , which were calculated from the structural analysis. This difference is significant and it indicates that the dopant concentration in both crystals is not

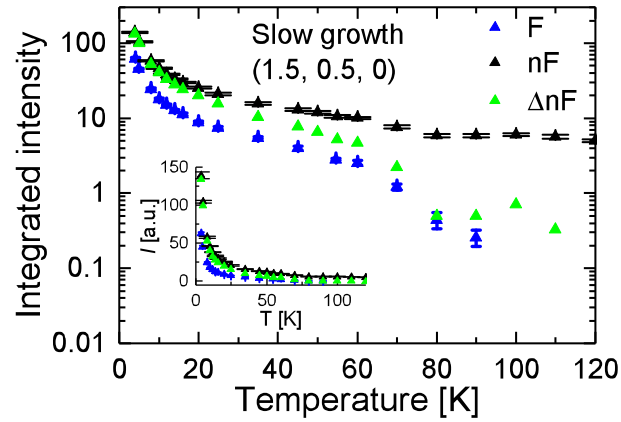


Figure 2.17: Temperature dependence of the integrated intensity  $I$  of the  $(1.5, 0.5, 0)$  magnetic reflection of the NCCO  $x = 0.125$  - *sg* single crystal, shown on a logarithmic scale. The measurements were taken with and without the Be filter,  $F$  and  $nF$  respectively.  $\Delta nF = I(T) - I(T_{max})$ . The insert shows the same data on a linear scale for comparison.

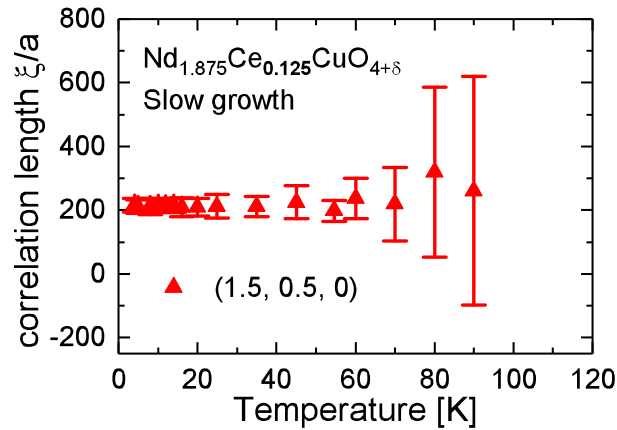


Figure 2.18: Temperature dependence of the correlation length  $\xi/a$  of the  $(1.5, 0.5, 0)$  magnetic reflection of the NCCO  $x = 0.125$  - *sg* single crystal.

similar. The correlation length of the AF Bragg peaks in the fast grown sample are also shorter than for the slow grown sample. Elastic neutron scattering on NCCO for different dopant concentrations has revealed that the correlation length decreases upon electron-doping near the AF–SC phase boundary [74]. In relation to these results, in section 2.1 the XRF analysis showed that the fast grown samples have a higher Ce concentration than the slow grown crystals. Observations from the neutron diffraction corroborates the results from the elemental analysis. Further analysis of these results will be given in Section 2.5

## 2.4 Transport measurements

Part II of this thesis fully concerns the study of the out-of-plane magnetoresistance of underdoped NCCO single crystals. In this section a special focus is given to two NCCO samples with  $x = 0.125$ , one from the fast grown and one from the slow grown batches. As it will be discussed in Part II Section 6.1.2 and Chapter 9, transport measurements are a good probe to observe changes in the spin structure and thus to identify certain features which can be attributed to long-range AF order. In the case of the electron-doped cuprates it is important to consider that these features arise from their particular magnetic structure. A scheme of the magnetic structure is provided in Part II, Chapter 6, Fig. 6.1.

In Part II Chapters 8 and 9, it will be established that, in the high field regime, a sharp irreversible feature is found in the angle-dependent magnetoresistance (AMR) of underdoped NCCO samples at field orientations around the Cu–O–Cu direction. This step-like feature originates from a field induced reorientation of the collinear AF  $\text{Cu}^{2+}$  spins and can be considered as a sign of long-range AF order. For a more detailed discussion of the origin of the features detected in the magnetoresistance of electron-doped cuprates, the reader is referred to Part II.

Quantity	fast growth	slow growth
lattice constant [Å]	3.949	3.9475
max T of Bragg reflection [K]	$120 \pm 10$	$80 \pm 10$

Table 2.6: Summary of the two main parameters obtained from the neutron diffraction measurements for the slow and fast grown samples.

The focus in this section is the observation of the step-like feature in the AMR as a mean to detect long-range AF order and to compare between the behavior of the two  $x = 0.125$  samples. A detail that should be considered before analysing the results presented in this section is that, according to the observations made in Part II Sections 8.1 and 8.2, the width of the hysteresis  $\Delta\varphi$  has a nonmonotonic temperature dependence. Additionally, the the step-like feature and  $\Delta\varphi$  in the non-superconducting (non-SC) samples is observed at the lowest temperatures, 1.4 K; while for the superconducting (SC) samples, the signs of AF are only seen above the transition temperature  $T_{c,o}$ .

For the experiment, from the as-grown crystal rod, samples of  $0.3 \times 0.3 \times 1 \text{ mm}^3$  were cut. The longest dimension corresponded to the [001] crystallographic direction. The samples were annealed at  $910^\circ\text{C}$  for 40 hours. The interlayer field-dependent magnetoresistance was measured by performing field sweeps with the field parallel to the  $\text{CuO}_2$  layers. The angle dependent magnetoresistance (AMR) was measured by rotating the field as a function of the azimuthal angle  $\varphi$  in a steady magnetic field. The angle  $\varphi$  is the angle between the direction of the applied magnetic field and the [100] crystallographic direction. Thus, the angles are defined as  $\varphi = 0^\circ$  as equivalent to  $\mathbf{B} \parallel [100]$  and  $\varphi = 45^\circ$  to  $\mathbf{B} \parallel [110]$ . A sketch with the definition of the angles and the direction of the applied current is given in Part II Chapter 7 in the right panel of Fig. 7.2. The measurements were performed in a temperature range of 1.4 – 100 K with a  $B = 14 \text{ T}$  magnetic field. The magnetoresistance is defined as  $\Delta R(B)/R(0) \equiv R(B) - R(B=0)/R(B=0)$ . A comprehensive description of the measurements method and the sample contacts are given in Part II Section 7.

### 2.4.1 Results

Figure 2.19 shows the zero-field temperature dependence of the resistance  $R$  of the two NCCO samples with  $x = 0.125$ . The resistance is normalized to the room temperature resistance  $R(300 \text{ K})$ . Both samples show partial superconductivity. Although the resistance of neither samples fully decreases to zero at the lowest temperature, the resistance of the fast grown sample decreases by  $\approx 30\%$  from the fully normal state value, while for the slow grown sample the resistance almost reaches zero. Therefore, the slow grown sample is more superconducting. The SC onset temperature is  $T_{c,o} = 16 \text{ K}$  for both samples.

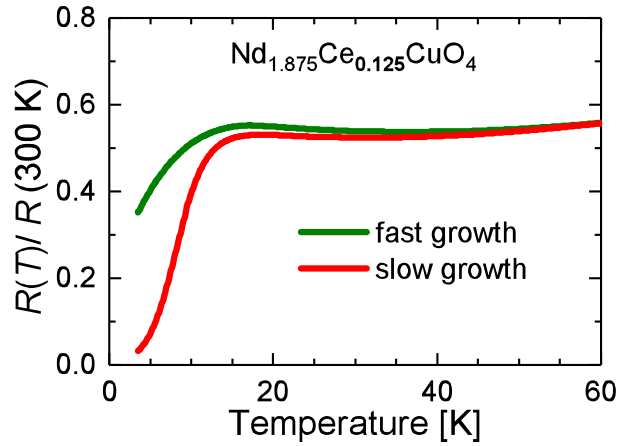


Figure 2.19: Normalised resistance versus  $T$  for NCCO from the fast and slow grown single crystals with  $x = 0.125$ .

The field-dependent magnetoresistance of the two samples for a field applied parallel to the  $\text{CuO}_2$  layers at angles close to the  $[100]$  direction at 1.4 K is shown in Fig. 2.20. In Part II the field dependence of the magnetoresistance is measured to detect the transitions from the noncollinear to the collinear state. In the case of these two samples, the application of a magnetic field does not suppress the superconductivity at the lowest temperature, and no such features are observed. For both samples the magnetoresistance increases monotonically with increasing magnetic field, but the magnetoresistance of the slow grown sample is larger at all fields and, for a field  $B = 14$  T, by almost a factor of 12. This increase in magnetoresistance is clear, since the slow grown sample is more superconducting.

In Fig. 2.21 the AMR of the same two samples at low temperature are shown. The AMR of both samples has a  $90^\circ$  periodicity with a maximum at the field orientations  $\mathbf{B} \parallel [100]$  and a minimum at  $[110]$ . In the case of the slow grown sample, shown in the right panel of Fig. 2.21, the  $B = 14$  T field does not suppress superconductivity and no sign of AF features can be observed. The AMR has a completely smooth fourfold reversible behavior. A small kink close to  $\varphi = 135^\circ$  can be seen, however, this turned out to be a measurement artifact. The AMR for this sample is very similar to the AMR of sample  $x = 0.13$ , shown in Fig. 8.11. On the left panel of Fig. 2.21 a close-up of the AMR around the  $[010]$  direction at 1.4 K for the slow grown sample is shown. The overall AMR shows some asymmetry, as shown in the inset of the Figure: the magnetoresistance at  $[100]$  is higher than

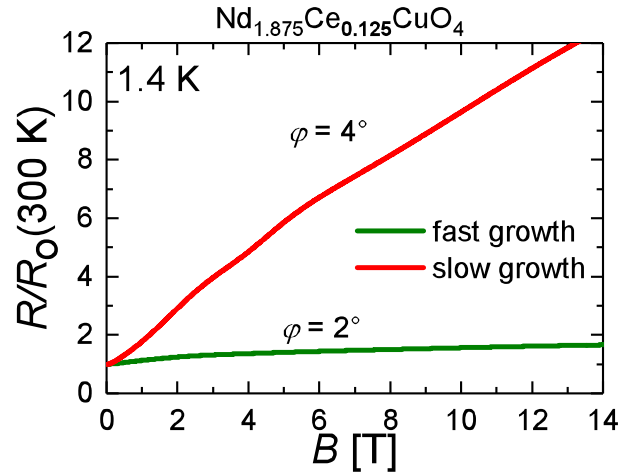


Figure 2.20: Field-dependent magnetoresistance of the two underdoped NCCO samples with  $x = 0.125$  at 1.4 K: fast grown sample (green line); slow grown sample (red line).

at [010]. This is caused by a slight misalignment of the samples, which means during rotation the magnetic field is not exactly parallel to the  $\text{CuO}_2$  plane. In the main panel it can be seen that, on top of a smooth fourfold AMR, a step-like feature appears after the field passes through the [100]/[010] directions. The steps are indicated with the black arrows in the figure. A more detailed analysis of the behavior and origin of this feature is given in Part II, Chapter 9. Considering the analysis presented in the mentioned sections, the observation of such features in the  $x = 0.125$  fast grown sample indicates the existence of long-range AF order at this dopant concentration. But more important is the fact that such features are visible at 1.4 K, when the sample is in a partially SC state. As already mentioned, for fully SC samples the step-like feature is only seen at temperatures above the  $T_{c,o}$ .

To observe and compare the behaviors of the AMR of both samples at these two temperature regions, i.e. below and above  $T_{c,o}$ , the AMR at  $T = 27\text{ K}$  is shown in Fig. 2.22. The overall amplitude of the AMR decreases and the fourfold symmetry is largely maintained. At this temperature the anisotropy of the AMR is inverted: the magnetoresistance has a maximum at  $B \parallel [110]$  and the minimum is around the  $B \parallel [100]$  field orientations. In Part II Section 8.2 it will be shown that the inversion of the anisotropy at temperatures above  $T_{c,o}$  is commonly seen in the SC samples, which implies that there is an anisotropy of the critical fields in the

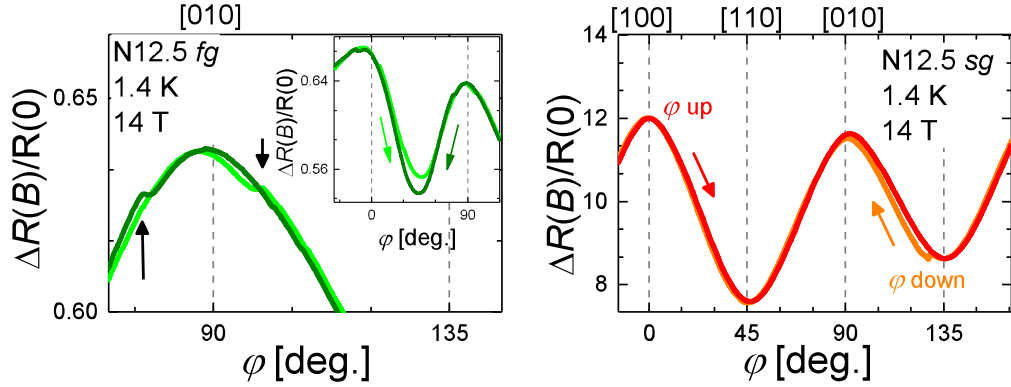


Figure 2.21: AMR of the two NCCO underdoped samples with  $x = 0.125$  at 1.4 K for an applied magnetic field  $B = 14$  T oriented parallel to the  $\text{CuO}_2$  layers. The colored arrows indicate the directions of the rotation,  $\varphi$  up and  $\varphi$  down correspond to the field rotation with increasing and decreasing angle  $\varphi$ , respectively. **Left:** Close-up of the AMR for the fast grown sample  $x = 0.125 - fg$  around  $\varphi = 90^\circ$ . The vertical black arrows point to the step-like feature observed close to the  $[100]/[010]$  directions. The inset displays the AMR in the whole angular range. **Right:** AMR for the slow grown sample  $x = 0.125 - sg$ .

resistive state. Therefore in this respect, the observed changes are consistent with the behavior of other SC samples. Additionally, the hysteretic step-like feature is present for both samples. It is worth noticing that  $\Delta\varphi$  at 27 K for the fast grown sample is smaller than at 1.4 K. The change in  $\Delta\varphi$  will be addressed in Part II, Chapter 9. For now, it is sufficient to state that the decrease of  $\Delta\varphi$  at temperatures above 20 K for the fast grown sample is consistent with the behavior of the non-SC samples. See Fig. 8.7.

Furthermore, the AMR was measured for these two samples at higher temperatures until the step-like feature was no longer resolved. The summary of the temperature dependence of the hysteresis  $\Delta\varphi$  for the applied field  $B = 14$  T is shown in Fig. 2.23. The hysteretic step-like feature is unambiguously detected in the fast grown sample up to 80 K. At 100 K it is still visible but due to misalignment in the sample and temperature fluctuations the hysteresis could not be accurately measured. In the case of the slow grown sample, the amplitude of the AMR is strongly diminished above  $\sim 62$  K and thus the hysteresis could not be measured. The overall temperature dependence of  $\Delta\varphi$  for the  $x = 0.12 - fg$

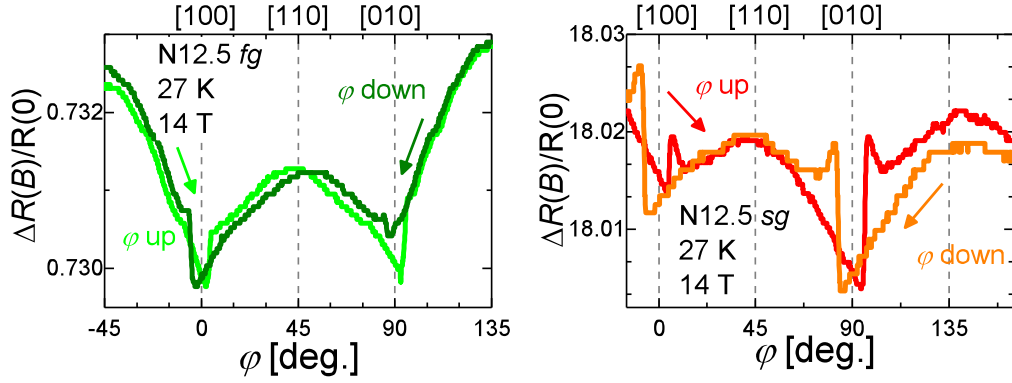


Figure 2.22: AMR of the two NCCO underdoped samples with  $x = 0.125$  at 27 K for an applied magnetic field  $B = 14$  T oriented parallel to the  $\text{CuO}_2$  layers. The colored arrows indicate the direction of the rotation. **Left:** Fast grown sample  $x = 0.125 - fg$ . **Right:** Slow grown sample  $x = 0.125 - sg$ .

sample has a very similar behavior to that observed for the non-SC samples, see Fig. 8.7. The highest value of  $\Delta\varphi$  is observed at 1.4 K. At the next measured temperature 27 K the  $\Delta\varphi$  decreases significantly. By comparison with the behavior of the non-SC samples, it can be suggested that the  $\Delta\varphi$  of the fast grown sample has a minimum close to 20 K but increases again above this temperature and reaches a maximum at  $\sim 45$  K. Above 60 K,  $\Delta\varphi$  does not change significantly. For the  $x = 0.125 - sg$  sample the hysteresis was observed for a temperature range  $T_c < T \leq 60$  K.

As already pointed out, at 27 K,  $\Delta\varphi = 4.8^\circ$  and  $8.6^\circ$ , for the fast and slow grown samples, respectively. In fact, at temperatures above  $T_{c,0}$ ,  $\Delta\varphi$  is always larger for the slow grown sample. In Part II, Chapter 9 it is discussed that one can trace a general trend of increasing  $\Delta\varphi$  as  $x$  approaches the SC regime, see the inset in Fig. 9.1. From the two  $x = 0.125$  samples, the fast grown one is more similar to the non-SC samples despite the presence of superconductivity. In this respect, it is reasonable for  $\Delta\varphi$  to be smaller for the fast grown sample, just like the non-SC in Fig. 9.1.

The hysteresis and its attributed step-like feature could be measured as long as the experimental resolution allowed for a reliable observation of the AMR, which can also be influenced by temperature fluctuations or sample misalignments. However, the highest possible temperature for the observation of the

step-like feature can be compared to the observations made from the neutron diffraction in Section 2.3, where it was indicated that the magnetic reflections of the slow grown sample fade at a lower temperature than those of the fast grown sample. In the magnetoresistance case, for the  $x = 0.125 - sg$  sample the step-like feature can be measured in a narrower temperature range than for the fast grown sample, and thus having a similar behavior as the magnetic reflections. It should be stressed that magnetotransport measurements are not a direct probe of the magnetic system, they reflect the magnetic properties of the samples while probing their conductive properties without being obstructed by the insulating precipitations. For this reason, the temperature at which the step-like feature vanishes can't be considered as a real value of  $T_N$ . If the temperature at which these features are found can be considered as a guide-line for the onset of antiferromagnetism, further investigations at high temperature on samples with well defined crystal quality and highly controlled dopant concentration should be pursued.

Overall, a very important point in this section is the highly similar behavior of the fast grown sample to the non-SC samples. The fast grown sample, despite showing a clear decrease of  $R(T)$  at  $T_{c,o}$ , the AMR at low temperature behaves both as a SC and non-SC sample. The observation of the step-like feature in the  $x = 0.125 - fg$  sample at 1.4 K is a sign of possible coexistence of the AF and SC states. However, exclusively from these results, it is difficult to judge on the origin of this coexistence. This will be further discussed in Section 2.5.

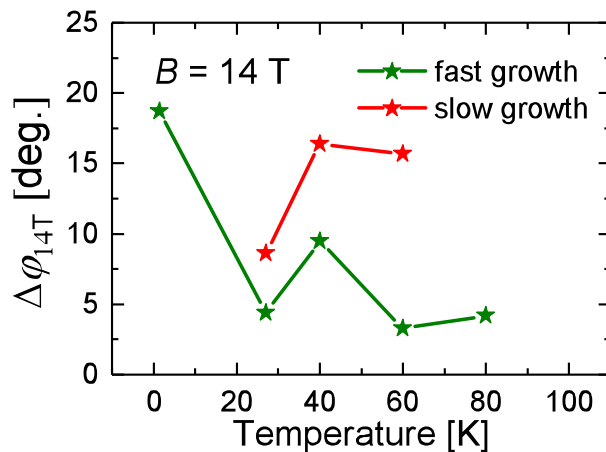


Figure 2.23: Temperature dependence of the hysteresis width  $\Delta\phi$  in the AMR of the two  $x = 0.125$  samples at  $B = 14$  T.

## 2.5 Discussion on NCCO $x = 0.125$

The results from the above presented experimental characterization clearly show different magnetic and superconducting properties between the two NCCO  $x = 0.125$  crystals. A summary of the measured quantities in this work is presented in table 2.7.

The values of  $T_N$  were taken from the temperature at which the (1.5, 0.5, 0) magnetic reflections of the two  $x = 0.125$  crystals vanished. Additionally it was shown in Section 2.3 that the (0.5, 1.5, 0) reflection of the fast grown sample disappeared at  $120 \pm 10$  K but this reflection was not measured for the slow grown sample and thus it is not shown in table 2.7.<sup>3</sup>

These results expose the observed differences between the two crystals and reaffirm the proposition that a change in the growth rate of NCCO can affect its physical properties. This is clearly shown by the higher  $T_c$  and SC volume fraction of the slow grown samples despite the lower Ce concentration.

The difference in the lattice constant measured by neutron diffraction can be directly related to the difference in dopant concentration obtained from the XRF data. The fast grown samples have a 2.14% higher dopant concentration than the slow grown samples, and the lattice constant is larger, by  $1.510^{-3}$  Å. These results agree with the knowledge that an increase in Ce concentration increases the lattice constant  $a$  due to the stretching of the Cu-O bond by the electrons added into the antibonding  $\sigma^*$  orbitals [34]. As mentioned in references [30, 54] the prepara-

---

<sup>3</sup>The uncertainty in the  $T_N$  values arises from the step size of the temperature increase for the neutron diffraction.

Quantity	fast growth	slow growth
$T_c$ [K]	$12.1 \pm 1$	$13.7 \pm 0.8$
SC vol	$26 \pm 16$	$38 \pm 17$
dopant concentration $x$	$0.1270 \pm 0.0032$	$0.1191 \pm 0.0035$
lattice constant [Å]	3.949	3.9475
$T_N$ [K]	$110 \pm 10$	$80 \pm 10$

Table 2.7: Overview of the obtained data from the sample characterization with the techniques presented in this text. The  $T_N$  is taken from the neutron diffraction measurements.

tion of the polycrystalline feed rod consists of the mixture of powders of  $\text{Nd}_2\text{O}_3$ ,  $\text{Ce}_2\text{O}_3$  and  $\text{CuO}$  of high purity according to the desired stoichiometric composition which are sintered at high temperatures in an oxygen atmosphere, thus the feed rod is made of polycrystalline NCCO. While a poorly performed weighing of the start materials can be a source of error, the results observed from XRF and magnetization demonstrate that the dopant concentration is within the desired range,  $x = 0.125$ . And so the difference in the measured dopant concentration between the two crystals is considered a consequence of the applied growth rate and not of an inherent error of the start materials.

The  $T_N$  is higher for the measured fast grown sample than for the slow grown one. This implies that the fast grown samples are more magnetic. According to the phase diagram, at a  $x$  with high  $T_N$ , the  $T_c$  and volume of superconductivity are lower than for  $x$  with a lower  $T_N$ . This is the exact behavior observed in the fast grown samples, which was discussed in Section 2.2. Furthermore, in the AMR the step-like feature was detected for both samples, but at 1.4 K it was only seen for the fast grown sample. This is a sign of long-range AF order in this sample at the lowest temperature.

Considering the shape of the phase diagram of the electron-doped cuprate superconductors [20, 26] shown for example in 1.2, and focusing on the antiferromagnetic regime, it is known that the Néel temperature  $T_N$  is maximum for the undoped parent compound which decreases with increasing dopant concentration up to the optimal doping  $x_{\text{opt}}$ , where the  $T_N$  vanishes. According to this representation, NCCO samples with higher dopant concentration show a lower  $T_N$ . However, as demonstrated from the results for the fast grown samples, this is not exactly the case. In comparison to the slow grown samples, despite having a higher Ce concentration, the magnetic features for the fast grown crystal which allow for approximation of the  $T_N$  show higher temperature critical values than for the slow grown samples.

Similarly, the relation of the  $T_c$  and the dopant concentration has a dome-like shape. This means that higher concentration of Ce results in a higher  $T_c$  up to the  $T_{c\text{opt}}$  of  $x = 0.145$ . Again, this is not the observed case for the two  $x = 0.125$  crystals; the samples with less Ce concentration have higher  $T_c$ .

Furthermore, although the relation of SC volume fraction with  $x$  is not established or discussed in the general phase diagram, from Ref. [54] it is known that

the volume of superconductivity also decreases with decreasing dopant concentration. This is however, a complicated parameter, since it is highly dependent on the annealing treatment.

In fact, considering the results from the samples 1 – 5 from the two crystals shown in figures 2.4, 2.6 and 2.3, the dopant concentration of each sample is not directly proportional to their  $T_c$  or volume of superconductivity. The observed SC properties do not show a direct correlation to the the dopant concentration of the individual samples. For example, in the case of the slow grown samples, the Ce concentration increases slightly to the center of the rod, i.e. samples 2 – 4, but the SC volume fraction decreases exactly at the middle, at sample 3. The  $T_c$  does not show a particular trend and also does not correspond to the Ce concentration in neither set of samples. A common result in both sets of samples is the decrease of SC volume fraction at the center of the rod, which is more pronounced in the fast grown samples. Sample 3 of  $x = 0.125 - fg$  even shows remanent magnetism of Nd at low temperature. Furthermore, closer examination of the transition curves of the DC magnetic susceptibility also shows that in both crystals, the transition width is largest in sample 3.

If the Ce concentration is unrelated to the obtained differences in the results between a slow grown crystal and a fast grown one, there are other important factors which can affect the superconducting properties of the NCCO samples. As already commented on in the results section, the pulling rate in the TSFZ can influence the diffusion of the building blocks at the growth front, in particular a slow grow rate allows for a better distribution of the growth units resulting in a better crystalline structure, less copper vacancies and strain centers.

Furthermore is the presence of oxygen, which is known to have a strong effect on sample properties and doping [75, 76]. The role of oxygen on the physical properties of the electron-doped cuprates is still not completely understood, however it has been suggested that its influence can be both seen as a dopant agent and as a source of disorder [31]. The relation of Ce and oxygen concentration in electron-doped cuprates is inversely proportional. As the electron carrier concentration increases, the oxygen content decreases [31]. This would imply that the slow grown samples have more oxygen than the fast grown samples.

The excess of oxygen can be traced to the growth process at the growth front. Sources of oxygen in the system are the feed rod and the growth atmosphere. Due

to the high temperatures needed to melt the flux, some evaporation of  $CuO$  is expected [21], so the starting materials experience a certain loss of oxygen during the growth process. Additional oxygen dissolves from the growth atmosphere into the molten zone. The solubility of oxygen is enhanced by a slow cooling rate of the solid-liquid interface, i.e. the growth front. The temperature of the solid-liquid interface is kept high for longer periods and so the oxygen dissolves more easily into the flux to then diffuse to the growth front. Considering that the highest concentration of oxygen would be at the gas-liquid interface, a radial decrease in oxygen would be expected. This is at the center of the growth front and thus and the center of the resulting crystal rod. Given the inversely proportional relation of oxygen and  $Ce$ , this is the observed result in the slow grown samples. For example, the measured  $Ce$  concentration increases to the center of the sample rod, which in turn corresponds to a lower content of oxygen at this part of the crystal.

If the slow grown samples are richer in oxygen than the fast grown ones, a logical question would be to ask where the excess of oxygen goes and why it should improve the superconducting properties of the electron-doped cuprates. To understand this, it should be considered that there are three possible sites for oxygen insertion: the in-plane, interstitial and apical oxygen. For example, a neutron diffraction study on  $NCO$  single crystals demonstrated that both annealed and oxygenated samples have a high number of oxygen defects in the plane and in the interstitial sites [77]. These deficiencies remain unaltered within error bars even after an annealing or oxygenation processes. Additionally, from this same study, it was observed that when the samples are annealed in an oxygen atmosphere, the occupation of the apical oxygen sites increases by 60%. Considering these premises, it can be concluded that the in-plane and interstitial sites are fixed once occupied and that the apical oxygen site is more mobile.

To understand the role of oxygen on the physical properties of electron-doped cuprates, the effect of the reduction process should be analyzed. Independent of the actual structural mechanism of the annealing process or if the oxygen is removed from the apical sites or the  $CuO_2$  layers; it is known that the reduction process also adds two electron carriers for each oxygen which is removed [78]. A discussion of the mechanism of superconductivity is not the main focus of this thesis, however in the most simple case of conductivity, electrons will propagate

without being scattered only in a perfect periodic potential and vacancies or impurities will disrupt the electron propagation and weaken superconductivity.

In this scenario a more perfect crystal lattice can function as a better medium for electron propagation. As the  $\text{CuO}_2$  layers are the conductive layers in the cuprate superconductors, it would make sense that fewer defects would enhance the superconducting properties of the system.

Taking this into consideration, it would be sensible that a higher percentage of the apical sites are filled in the as-grown crystal and that during growth the excess of oxygen also goes to the in-plane and interstitial sites to repair oxygen deficiencies in the  $\text{CuO}_2$  layers. The decrease in oxygen vacancies would result in less scattering centers. This is supported by the obtained results, the transition width is shortened for the slow grown samples and the  $\chi''$  shows less irregularities than the fast grown samples. This can be interpreted as evidence of better conductive layers. Concerning the effect of the annealing process, this analysis also implies that the reduction process is more favorable for the removal of apical oxygen and not of the in-plane oxygen, or at least to a larger extent. Additionally a side effect of a long annealing processes is the deterioration of the  $\text{CuO}_2$  layers by creating more oxygen vacancies, which then destroys superconductivity [34]. However, to confirm this hypothesis further studies on the structural composition of the slow grown samples should be carried out.

Furthermore, it has been mentioned that several approaches to the annealing process exist and many of them use a second annealing step where a small oxygen pressure is used to repair any defects [34, 79]. If this additional oxygen works as a healing agent for the  $\text{CuO}_2$  layers, this would mean that growing a NCCO crystal with a slow growth rate could help avoid this step and directly result in superconductivity with a simpler annealing process.

Another point which should be commented on, is the apparent coexistence of AF and SC in the fast grown sample during the transport measurements. The question of the coexistence between these two phases is still an unresolved issue. The origin of the coexistence could be electronic, where both phases compete with each other, or structural, where the mere majority of AF phase is destroyed by the insertion of charge carrier or annealing treatment. An additional scenario would be a phase separation, where islands of AF phase coexist within a mostly superconducting bulk material.

From the results presented in this work, it is difficult to reach a full conclusion, however, an analysis of the results can help to evaluate the two possible cases. The superconducting properties of the fast grown crystals are summarized in table 2.7. The high  $T_N$ , low SC fraction and low  $T_c$  which do not match the higher Ce concentration obtained from XRF are some of the characteristics which are improved in a crystal grown at a lower rate. Through a slow growth process a better crystal lattice is obtained which allows for an easier removal of apical oxygen and thus a higher SC volume. However these samples have a lower amount of dopant concentration and nonetheless a higher  $T_c$  and SC volume fraction. In this sense this behavior implies that the chemical composition is irrelevant up to some extent and thus the improvement of the superconducting properties could have an electronic origin.

On the other hand, this does not exclude the possibility of a phase separation. A possible scenario would be that the slow crystallization rate induced a mixture of different dopant concentrations within the same phase. This is also known as a spinodal decomposition [80]. In such a case a solution of two components separates into two phases with different chemical compositions and physical properties. This process is mainly determined by diffusion which is how the crystallization process by the TSFZ method occurs. When a non-congruent melting material is cooled down to a metastable composition, fluctuations in the composition will result in a phase separation. This process is known to improve the physical properties of certain materials. If this were the case for the slow grown crystals, a possibility would be a mixture of optimally doped and very underdoped regions, which could explain the improved superconducting properties. Unfortunately, the structural determination of such structures is highly complicated. Originally, spinodal phases can be detected by very difficult structural refinements or by the observation of satellite peaks in the diffraction pattern [81]. No evidence of such satellite peaks was seen during the neutron diffraction measurements. Nonetheless, a more detailed study with focus on the possible mixture of dopant concentrations could be attempted.

Furthermore, this work focused on the superconducting properties of samples which were annealed for 20 hours. Should the annealing process be further performed, it would be expected that the SC volume would increase. If an increase in the volume of superconductivity coincides with a decrease in the approximated

$T_N$  and the disappearance of the step-like feature at low temperature in the AMR, this would mean that the apparent coexistence of AF and SC phases is of the structural type, meaning that most of the sample becomes superconducting and the AF regions are eliminated or become less dominant in the structure. For this hypothesis to be supported, further studies of the magnetic properties of the fast and slow grown samples in relation to their annealing process should be conducted. It should be noted however, that a similar but not identical case is seen in the  $x = 0.12$  samples presented in Part II Section 8.2. Considering Figs. 8.11 and 8.15 where at 1.4 K the AMR of sample  $x = 0.12$  (b) is very similar to sample  $x = 0.13$ , showing only a smooth AMR with a  $90^\circ$  periodicity without any particular feature. However, as temperature increases and although the sample is still in the SC state, the 14 T field already suppresses superconductivity and the AF features are observed exactly as in a non-SC sample. Even the anisotropy is inverted as soon as 7 K. While this is also a case of coexistence of the AF and SC phases, in the case of the fast grown  $x = 0.125$  sample the step-like feature is seen together with superconductivity and not instead of it, as in the  $x = 0.12$  (b) sample. For the fast grown  $x = 0.125$ , the coexistence of AF and SC states seems to be a property of the sample itself. Although to corroborate this, samples of the fast grown batch should be further explored, trying different annealing times to test if the traces of AF order disappear or continue to coexist with SC. In order to fully confirm or disregard the possibility of a structural phase separation originating from a change in the growth rate of NCCO samples further investigation is needed.

### 3 NCCO $x = 0.13$

A correct characterization of the physical properties of any material requires high quality samples to avoid sample dependent results. In the particular case of the electron-doped cuprates, an issue which complicates the sample preparation is the need for a post-growth annealing process to induce superconductivity. In the ideal case, this process should be kept short to avoid sample decomposition, damage to the surface or to further generate epitaxial precipitations.

It was concluded from the discussion presented in Section 2.5 that the sample properties of the underdoped NCCO single crystals could be improved through a careful selection of the growth parameters, in particular a decrease in the growth rate. In order to investigate if the improved superconducting properties observed in NCCO samples which were grown with a slow pulling rate can also be obtained through shorter annealing process, the superconducting properties of two sets of underdoped NCCO samples with  $x = 0.13$  were measured, one from a crystal grown with a fast rate and another from a slow growth rate.

The crystals were grown as described in Section 1.3. 5 samples were obtained from each single crystal, similar to the samples shown in Fig. 2.1. It should be noted that the fast grown crystal was grown in 2006 by a former researcher at WMI [21]. However, there is no reason to believe that the growth process was different in any of the parameters listed in table 1.2 from Section 1.3. There is also no evidence of aging effects on NCCO single crystals and the samples are known to maintain their properties and crystallinity for long periods of time [21]. Since the crystal was not newly made, the uppermost part of the final rod was not available and the samples were taken from a lower cut of the rod. To further attest to the sample quality and confirm that the samples were suitable for this study, the X-Ray Laue pattern of all samples were examined and no evidence of twinning was observed. The samples were annealed at 935°C for 20 hours in an Ar atmosphere. After the first 20 hours of annealing the ZFC DC magnetic

susceptibility of the samples was measured at the same conditions described in Section 2.2. This was followed by another annealing process at the same conditions and measurement of their magnetic susceptibility. The results and a short discussion are presented in the next section.

### 3.0.1 Results

The superconducting properties of the fast grown samples are presented with the temperature dependent DC and AC magnetic susceptibility curves in Figs. 3.1 and 3.2. For simplicity, only the imaginary component of the AC susceptibility,  $\chi''$ , is shown. Figure 3.1 (a) demonstrates that all samples showed superconductivity after the first 20h of heat treatment. Samples 1 and 2 show the highest  $T_c$  of the set and there is no significant difference in the transition width between these two samples. The superconducting transition in all samples is broad and, particularly for samples 3 and 4, highly irregular. Samples 3 and 4 have the lowest  $T_c$  and in this same figure the onset temperature of these samples is shown to also be slightly lower.

The effect the second annealing process has on the susceptibility of the samples can be observed in Fig. 3.1(b). The superconducting properties of the samples improve, the  $T_c$  is increased for samples 1 – 4. In the case of samples 3 and 4 the susceptibility curve has a more homogeneous transition to the superconducting state, although some irregularities can still be observed. However, the additional 20 hours of annealing cause a 1.5 K decrease in  $T_c$  for sample 5. The average  $T_c$  of the fast grown samples after 20h of annealing is  $T_c = 11.8 \pm 2.6$  and this value increases to  $T_c = 14.0 \pm 1.7$  after the second reduction process.

The observed irregularities of the susceptibility transition curves can be due to the presence of lattice defects, such as oxygen defects in the  $\text{CuO}_2$  layers. The presence of intragrain defects can be derived from  $\chi''$  of the AC magnetization in Figs. 3.2 (a) and (b), by observation of multiple peaks. Additionally, the effect the second annealing process has on these defects is more clearly seen in these curves. For example in the case of sample 5, although the total  $T_c$  decreased after the second annealing,  $\chi''$  became smoother, which implies a decrease in the number of defects. For samples 1 – 4 multiple peaks are still visible after the second annealing process, however, the susceptibility becomes smoother in general. The change in the susceptibility strongly suggests that further annealing would

be necessary to repair defects and obtain a more homogeneous superconducting transition.

A summary of the  $T_c$  values for the fast grown samples after 20 and 40 hours of annealing is presented in Table 3.1.

$x = 0.13$ fast growth		
$T_c$	20 h	40 h
1	14.2	16.4
2	14	15.3
3	9	13.7
4	8.3	12.7
5	13.4	11.9
mean	$11.8 \pm 2.6$	$14.0 \pm 1.7$

Table 3.1: Summary of the change in  $T_c$  with annealing for samples 1 – 5 of the  $x = 0.13 - fg$  crystal.

The ZFC DC magnetic susceptibility for the samples of the slow grown crystal is shown in Fig. 3.3 (a) and (b). All samples are superconducting and have higher  $T_c$  than the fast grown crystals, which coincides with the results observed from the  $x = 0.125$  crystals. Visual examination of the susceptibility curves reveals that the superconducting transition is highly homogeneous in these samples and that the transition width is less broad. Figure 3.3(b) shows that the additional 20h of heat treatment has a small improving effect on the  $T_c$  of the samples, and in the

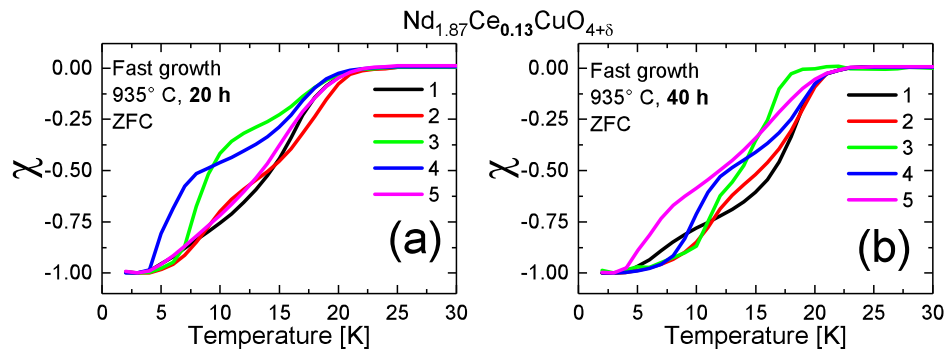


Figure 3.1: Normalized temperature dependence of the DC susceptibility  $\chi(T)$  for samples 1 – 5 of the  $x = 0.13 - fg$  crystal. (a) Samples 1 – 5 after 20h annealing. (b) Samples 1 – 5 after 40h annealing.

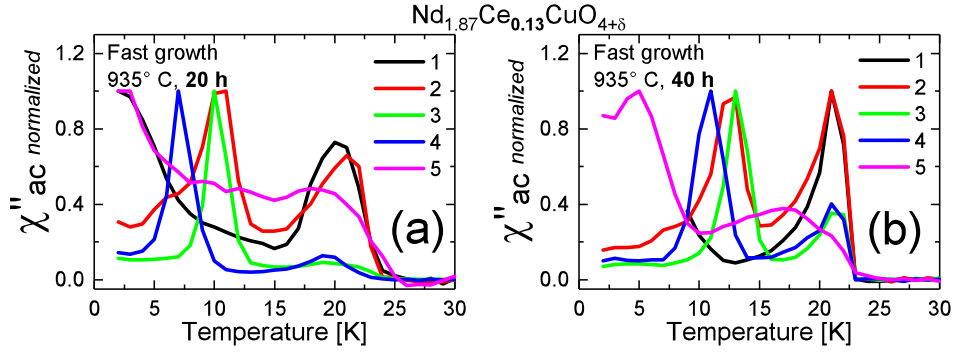


Figure 3.2: Normalized temperature dependence of the AC susceptibility  $\chi''(T)$  for samples 1 – 5 of the  $x = 0.13$  –  $fg$  crystal. (a) Samples 1 – 5 after 20h annealing. (b) Samples 1 – 5 after 40h annealing.

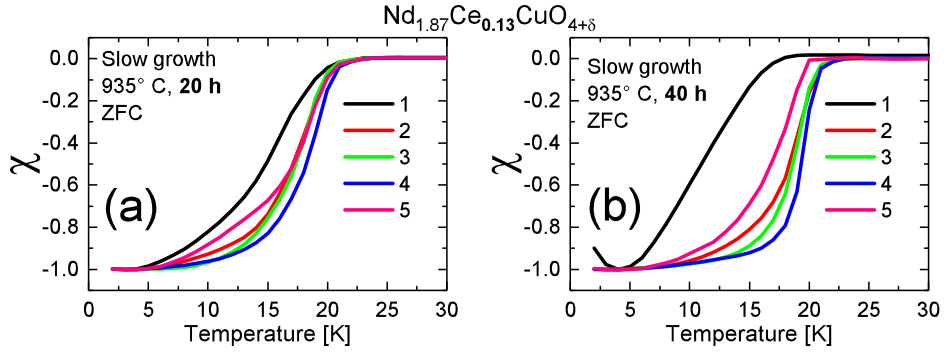


Figure 3.3: Normalized temperature dependence of the DC susceptibility  $\chi(T)$  for samples 1 – 5 of the  $x = 0.13$  –  $fg$  crystal. (a) Samples 1 – 5 after 20h annealing. (b) Samples 1 – 5 after 40h annealing.

case of sample 1 the  $T_c$  even decreases by 3.9 K. Although the  $T_c$  of samples 2 – 4 increases by  $\sim 1.2$  K, the average  $T_c$  of this sample set goes from  $16.9 \pm 1.3$  K to  $16.8 \pm 3.0$  K. The transition width becomes less broad for samples 2 – 5 after the second annealing process, but for sample 1 the effect was mostly damaging, in fact at the lowest temperatures a remanence of the Nd magnetization can be appreciated in the DC susceptibility in Fig. 3.3(b).

To compare the presence of lattice defects between the slow grown samples and the fast grown samples, the  $\chi''$  for the  $x = 0.13$  –  $sg$  samples can be seen in Fig. 3.4. After the first 20h of the reduction process, the susceptibility  $\chi''$  curves show the presence of satellite peaks for all samples indicating some inhomogeneities in the  $CuO_2$  layers. Despite these additional peaks, the transition is smoother than

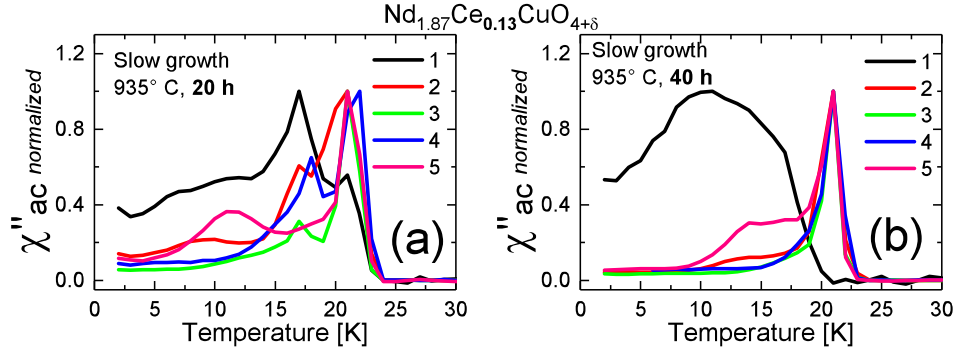


Figure 3.4: Normalized temperature dependence of the AC susceptibility  $\chi''(T)$  for samples 1 – 5 of the  $x = 0.13 - fg$  crystal. (a) Samples 1 – 5 after 20h annealing. (b) Samples 1 – 5 after 40h annealing.

$x = 0.13$ slow growth		
$T_c$	20 h	40 h
1	14.8	10.9
2	17.1	18.4
3	17.3	18.5
4	18.2	19.3
5	17.1	16.7
mean	$16.9 \pm 1.3$	$16.8 \pm 3.0$

Table 3.2: Summary of the change in  $T_c$  with annealing for samples 1 – 5 of the  $x = 0.13 - sg$  crystal.

in the case of the fast grown samples. Furthermore, after 40h of annealing the satellite peaks disappear completely in samples 2 – 4 and in sample 5 it is highly decreased. The susceptibility  $\chi''$  of sample 1 loses shape which implies sample decomposition.

Table 3.2 shows a summary of the  $T_c$  for the samples from the  $x = 0.13$  slow grown crystal and its change with annealing.

An estimation on the SC volume fraction for both sets of samples was also performed and an illustration comparing its change with further annealing is shown in Figures 3.5 and 3.6. In the case of  $x = 0.13 - fg$  set of samples, the SC volume increases except in the case of sample 2, although the decrease is a very small percentage. In average the volume fraction of the fast grown samples

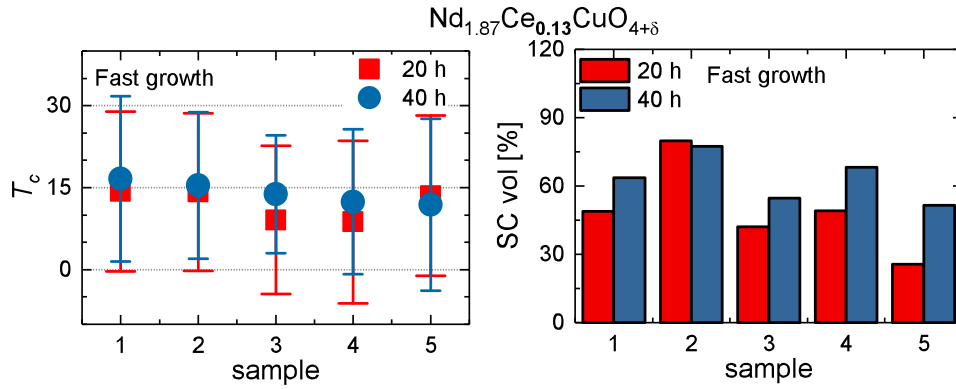


Figure 3.5: **Left:** Graphic representation of the  $T_c$  and  $\Delta T_c$  of the  $x = 0.13 - fg$  samples 1 – 5 after 20 and 40h of heat treatment. **Right:** Volume fraction of superconductivity of each  $NCCO_{x = 0.13 - fg}$  sample as a function of a lead reference sample and its change with annealing time.

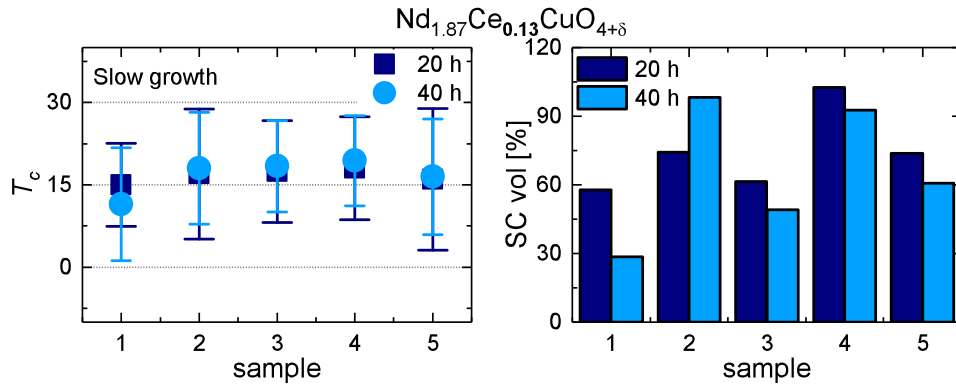


Figure 3.6: **Left:** Graphic representation of the  $T_c$  and  $\Delta T_c$  of the  $x = 0.13 - sg$  samples 1 – 5 after 20 and 40h of heat treatment. **Right:** Volume fraction of superconductivity of each  $NCCO_{x = 0.13 - sg}$  sample as a function of a lead reference sample and its change with annealing time.

increases from 49 % to 63 %.

On the other hand, additional annealing on the slow grown samples did not improve the SC volume fraction. In fact, except for sample 2, it mostly decreased, from 74.0 % to 65.9 %.

From these results two general observations can be made. Firstly, just like for the  $NCCO_{x = 0.125}$  crystals, a slow growth rate results in better superconducting properties in comparison to crystals grown with a fast growth rate. The

---

$x = 0.13 - sg$  samples have higher  $T_c$  and SC volume fraction.

Secondly, the second annealing treatment had a relevant improving effect on the SC properties of the fast grown samples. Past investigations on successive 20 hour reduction processes for NCCO samples with  $x = 0.13$  [54] have demonstrated that crystals can need up to 80h for observing the maximum of SC volume fraction, even close to 100%. From these observations, it is inferred that further annealing would have a beneficial effect on the SC properties of the samples presented in this work. It should be mentioned that the crystals studied in the example from Ref. [54] were new and obtained from the most upper cut of the crystal rod. Thus, the inhomogeneous SC transition and low  $T_c$  observed in the  $x = 0.13 - fg$  samples are not a consequence of crystal aging, or of the origin of the sample relative to the crystal rod. Evidently, the duration of the reduction process has implications in time and energy consumption. Additionally, the heat treatment can damage the sample surface, which makes the samples unsuitable for any surface investigations, such as scanning tunneling microscopy (STM).

This is not necessarily the case for slow grown samples. In fact, this sample set already shows good SC properties after only 20h of annealing treatment. While the effect of the second annealing process was a narrowing of the transition width and an increase of  $T_c$  in samples 2 – 4, the SC fraction decreased. While this observation can seem contradictory, the generation of epitaxial precipitations can be responsible for this outcome. It is possible that parts of the sample become better superconducting while other parts of the sample are decomposed due to the annealing treatment. As already mentioned, such precipitations could be detrimental to the interpretation of experimental results or even interfere with the properties of the sample.

These results can be explained considering the analysis made in Section 2.5 for the  $x = 0.125$  samples. A slow pulling rate allows for a better arrangement of the growth units at the solid-liquid interface. Through a slow cooling rate of the crystallization front, a better selection for the crystallization sites and occupation of the oxygen sites in the crystal lattice can be enhanced. This avoids the accumulation of defects in the lattice, thus in a more perfect crystal lattice, the  $\text{CuO}_2$  layers have less copper and oxygen vacancies, which allow better conditions for electron transfer and less pinning centers.

In respect to the annealing process, a lattice with less defects or straining cen-

ters can allow for a better diffusion of oxygen, which can explain why in the slow grown samples the reduction times do not need to be as long as for the fast grown crystals. Additionally, this can have an effect on the stability of the  $\text{CuO}_2$  layers. Less vacancies and defects can make them less susceptible to perturbations by the heat treatment. However, this can also mean that the samples grown under these parameters reach their limits more easily and would not endure too many reduction processes. A careful observation of their properties should be considered when working with these samples.

As mentioned in Section 1.2.1, it is still highly debated if the annealing process only removes oxygen from apical sites, from the  $\text{CuO}_2$  layers or a combination of the two. From the susceptibility  $\chi''$  curves presented in this section, it is observed that the defects in the conduction layers seem to be repaired after further annealing, in particular for the fast grown samples. It is possible that the oxygen vacancies in the layers become repaired with oxygen removal from the apical sites, since it is known that the apical position is the most mobile of the three oxygen sites. However, this scenario is mostly speculative and should be considered as a matter of further investigation.

## 4 NCCO: other dopings

Finally, to observe the effect a slow growth rate has on NCCO single crystals with even lower dopant concentrations than the ones presented in the last chapters, NCCO crystals with  $x = 0.11$  and  $x = 0.10$  were grown with a slow growth rate. In this case, no other crystals with the same dopant concentration were grown with a fast growth rate as for the  $x = 0.125$  and  $x = 0.13$  samples, so the superconducting properties measured from the obtained samples from the slow growth process will be compared with the results for samples from past investigations on a related topic [54]. Nonetheless, a general overview of the results clearly supports the conclusions made in this work without the need to present other samples.

From the as-grown crystal rod five samples were obtained for the  $x = 0.11$  in the same way presented in Fig. 2.1. In the case of the  $x = 0.10$  crystal, the slab was cut into 7 samples of  $0.3 \times 0.3 \times 1$  mm. The samples 1 and 7 correspond to the outermost part of the crystal rod. Sample 4 is not shown since it was used for other purposes and was not available for measurement. All samples,  $x = 0.11$  and  $x = 0.10$ , were annealed for 20 hours at  $900^\circ$  in an Ar atmosphere. The SC properties of the sample were measured with the ZFC DC magnetic susceptibility and the SC volume fraction of the samples was estimated by the use of a lead reference sample as described in past sections.

### 4.0.2 Results

The temperature dependent ZFC DC magnetic susceptibility of the  $x = 0.11 - sg$  samples showing the superconducting transition and a representation of the estimated SC volume fraction are shown in Fig. 4.1 (a) and (b), respectively. All five samples are superconducting and they all have very similar transition temperature and transition width. Only sample 2 has a lower  $T_c$  by  $\sim 1.1$  K. The superconducting transition for all samples is smooth and does not show signifi-

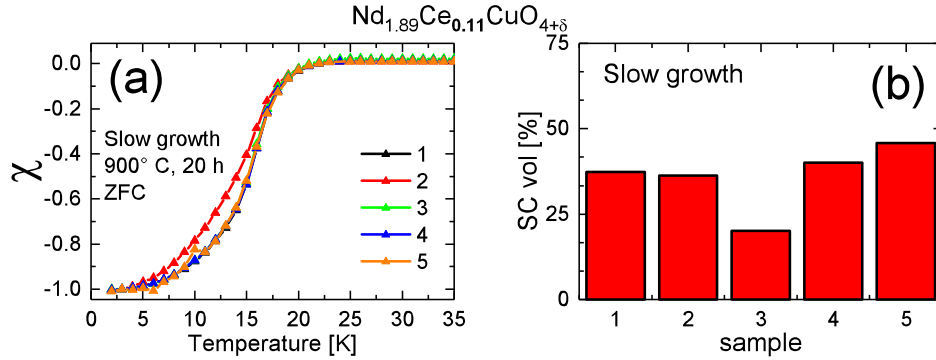


Figure 4.1: (a) Normalized temperature dependence of the DC susceptibility  $\chi(T)$  for samples 1 – 5 of the  $x = 0.11 - sg$  crystal after 20h annealing. (b) Volume fraction of superconductivity for each NCCO  $x = 0.11 - sg$  sample as a function of a lead reference sample.

cant inhomogeneities.

The average SC fraction of the  $x = 0.11 - sg$  samples is  $35.9 \pm 9.6\%$ . From the representation of the SC volume fraction seen in Fig. 4.1 (b), the sample with the least SC fraction is not sample 2 but sample 3. A decrease in the volume of superconductivity at the center of the crystal rod was also observed in the  $x = 0.125$  crystals and it was slightly less pronounced in the  $x = 0.13$  samples.

In the case of the  $x = 0.10$  single crystal, the normalized temperature dependence of the DC magnetic susceptibility of samples 1 – 7 for this crystal are shown in Fig. 4.2 (a). Surprisingly the  $T_c$  obtained for these samples, with a rather low dopant concentration, is unusually high. Sample 6 has the highest  $T_c$  of the set, with 20.5 K, which is even higher than the  $T_c$  observed for the  $x = 0.125$  samples. Until now, crystals of NCCO with  $x = 0.10$  had been grown with a fast growth rate and so during past investigations [54] the observed SC properties of such samples resulted in  $T_c \approx 5$  K and almost negligible SC volume fraction. However, the samples discussed in Ref. [54] were measured under an applied magnetic field of 100 Oe and therefore cannot be directly compared with these new results. Therefore, in the inset of Fig. 4.2 (b) the magnetic susceptibility of a  $x = 0.10$  sample obtained from a fast grown crystal, measured under a 2 Oe magnetic field is depicted. This sample had the same geometry as the  $x = 0.10$  samples presented in this section. The  $T_c$  for this sample is 7.2 K, however a step at higher temperature is observed and the general shape of the transition is very

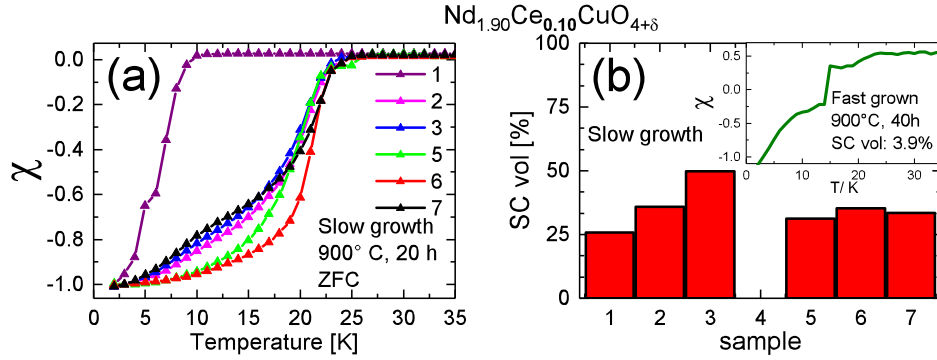


Figure 4.2: (a) Normalized temperature dependence of the DC susceptibility  $\chi(T)$  for samples 1 – 7 of the  $x = 0.10$  – *sg* crystal 20h annealing. (b) Volume fraction of superconductivity of each NCCO  $x = 0.10$  – *sg* sample as a function of a lead reference sample. The insert shows the ZFC measurement of a sample obtained from a  $x = 0.10$  – *fg* crystal measured under the same conditions as samples 1 – 7 from the slow grown crystal.

irregular.

The estimated SC volume fraction for the  $x = 0.10$  – *sg* samples is also higher than expected. For example, even sample 1 which has the lowest  $T_c$ ,  $T_c = 6.4$  K, has 27.7% in volume of superconductivity. The average SC volume fraction is  $35.2 \pm 8\%$ . Unfortunately without sample 4, it can not be known if there is also a decrease of SC volume at the middle part of the crystal. Samples 3 and 5 show a difference of 18.4% in SC volume, which can complicate any extrapolation of the observed results. However, the general behavior of the  $x = 0.10$  – *sg* samples clearly points to an improvement in the superconducting properties, in comparison with previous experiences with this dopant concentration [12, 21, 54].

Furthermore, to confirm the absence of lattice inhomogeneities, the AC magnetization was measured and the  $\chi''$  susceptibility of both sets of samples is shown in Fig. 4.3 (a) and (b). The susceptibility  $\chi''$  of the five  $x = 0.11$  – *sg* samples is very similar, showing one smooth peak and with a slight variation in its width. No satellite peaks are observed and the susceptibility fully saturates at low temperatures for all samples.

The  $x = 0.10$  samples also have very similar behavior with only one peak and, despite a slight presence of noise in the measurements, no significant transition

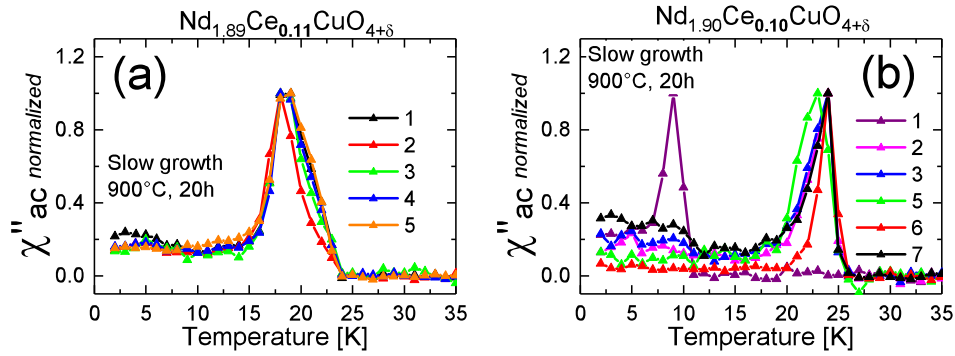


Figure 4.3: Normalized temperature dependence of the AC susceptibility  $\chi''(T)$  after 20h annealing for: (a) Samples 1 – 5 of the  $x = 0.11 - sg$  crystal; (b) Samples 1 – 7 of the  $x = 0.10 - sg$  crystal.

irregularities, except for sample 1. The results for sample 1 do not fit the behavior shown by the rest of the samples<sup>1</sup>. An explanation for this behavior could be flux inclusions, which rarely occur during a stable growth process but can be expected when there is a sudden decrease in the pressure in the growth chamber or mechanical disturbances. Nonetheless, the behavior of the rest of the samples is highly consistent and the susceptibility  $\chi''$  indicates a homogeneous superconducting transition.

Finally, an illustration of the  $T_c$  and transition width  $\Delta T_c$  for both sets of samples is shown in Fig. 4.4 (a) and (b). The superconducting properties of the  $x = 0.11 - sg$  samples have low variation and have a relative high transition temperature  $T_c = 14.9 \pm 0.5$  K, which is slightly higher than the average  $T_c$  obtained for the  $x = 0.125$  crystals, and transition width  $\Delta T_c = 12.2$ .

As for  $x = 0.10 - sg$  samples, the average transition temperature is  $T_c = 16.8 \pm 5$  K and  $\Delta T_c = 13.7$ . Considering that the inconsistent properties of sample 1 could be due to random flux inclusions, and if so this sample could be excluded, the transition temperature value changes to  $T_c = 18.9 \pm 0.9$  K.

Contrary to the belief that homogeneous and stable NCCO crystals can only be achieved for a dopant concentration  $0.12 \leq x \leq 0.18$  [57], these results indicate that superconducting NCCO single crystals can be synthesized down to at least a dopant concentration  $x = 0.10$ . By observation of the DC susceptibility obtained

<sup>1</sup>Other samples from this crystal were measured and their SC properties agree with the high  $T_c$  values presented in this work

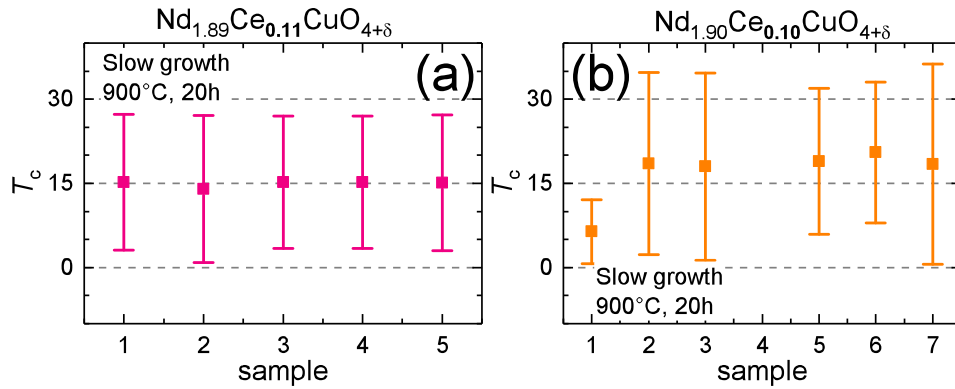


Figure 4.4: Graphic representation of the  $T_c$  and  $\Delta T_c$  of (a)  $x = 0.11 - sg$  single crystals. (b)  $x = 0.10 - sg$  single crystals.  $\Delta T_c$  is represented by the error bars. The dotted lines are included as a guide to the eye.

from these last two sets of samples, it was demonstrated that a significant increase in the transition temperature can be achieved through a slow growth rate. Additionally, an atypical high  $T_c$  was observed in the  $x = 0.10$  samples, which is worthy of further investigation.



## 5 Conclusion

The crystal growth and characterization of underdoped NCCO single crystals for the  $0.10 \leq x \leq 0.13$  dopant concentration range has been presented. The focus of this work was to identify the influence growth parameters have on the superconducting properties of single crystals. The growth parameter of interest was the pulling rate. Thus, NCCO single crystals were grown with the TFSZ method. A list of the relevant growth parameters were discussed in Ref. [21, 30], from which a variation was proposed in the speed of the pulling rate. As a result, two different growth rates were used for the growth of NCCO with  $x = 0.125$  and  $x = 0.13$ ; the fast growth rate was 0.5 mm/h and the slow growth rate 0.2 mm/h. The crystals with  $x = 0.11$  and  $x = 0.10$  were grown only with a slow growth rate.

The characterization of the  $x = 0.125$  crystals was performed with several techniques to compare the effects of the growth rate on the structure, dopant concentrations and other physical properties. The samples were prepared according to the requirements of the desired experiment. For crystals with other dopant concentration discussed in this work, only the magnetic susceptibility was analysed to investigate the effects of the change in the pulling rate.

In order to investigate if the distribution of the dopant concentration was homogeneous along the diameter of the crystal rod, an X-ray fluorescence elemental analysis was performed on five samples. These measurements were conducted at the crystal growth facilities of EPFL and the results were presented in Section 2.1. In Section 2.2 the magnetic susceptibility of the same five samples was discussed, the  $T_c$  was obtained and the superconducting volume fraction was estimated. Neutron diffractions performed at the Heinz Meier-Leibniz Zentrum and discussed in Section 2.3, were done on two single crystals. From the structural analysis the lattice constants were obtained and measurement of the temperature dependence of certain magnetic reflections gave information about the onset tem-

perature for the long range AF order. Finally, the angular dependent magnetoresistance measurements of two samples allowed for the observation of a signature feature for long range AF order. The temperature dependence of this feature and its hysteresis was measured.

The slow grown samples have higher  $T_c$  and SC volume fraction than the fast grown samples. The elemental analysis revealed that the Ce content of the slow grown samples is lower than for the fast grown samples. The measurement of the lattice constants  $a$  for the two crystals confirmed the difference in dopant concentration, since  $a$  is larger for the fast grown sample. Since for a higher dopant concentration a lower temperature for onset of antiferromagnetism is expected, a surprising result was the disappearance of the magnetic reflections for the slow grown crystal at lower temperature, thus indicating a lower Néel temperature  $T_N$ . The angular dependence of the magnetoresistance in Part II reveals that, for SC samples, the features of antiferromagnetism can be detected at temperatures above the  $T_c$ . Such an observation was made for the slow grown sample, however, in the case of the fast grown sample even in the SC state such features were detected, which implies the coexistence of these two phases.

A particular goal of this work was to determine if a change in the growth rate can produce crystals which require shorter annealing times. This was investigated by the comparison of SC properties of two NCCO  $x = 0.13$  fast and slow grown crystals. Five samples of each crystal were annealed for two nonconsecutive processes of 20 hours. Their magnetic susceptibility was measured after each reduction process to evaluate how the SC properties evolve with further annealing. The slow grown samples have a high  $T_c$  and SC volume after the first 20 hours of annealing. The second reduction process increases only slightly the  $T_c$  but does not improve the SC volume fraction. On the other hand, samples from the fast grown crystals show an important increase in  $T_c$  and SC volume.

Finally to investigate if superconductivity can be observed at lower dopant concentrations as a result of a change in the growth process, NCCO crystals with  $x = 0.11$  and  $x = 0.10$  were grown with a slow growth rate. Five samples of the  $x = 0.11$  crystal and six samples of the  $x = 0.10$  crystal were annealed for 20 hours and their magnetic susceptibility was measured. All samples were superconducting, the samples from the  $x = 0.11$  crystal showed high homogeneity and the samples from the the  $x = 0.10$  crystal showed an unexpectedly high  $T_c$ .

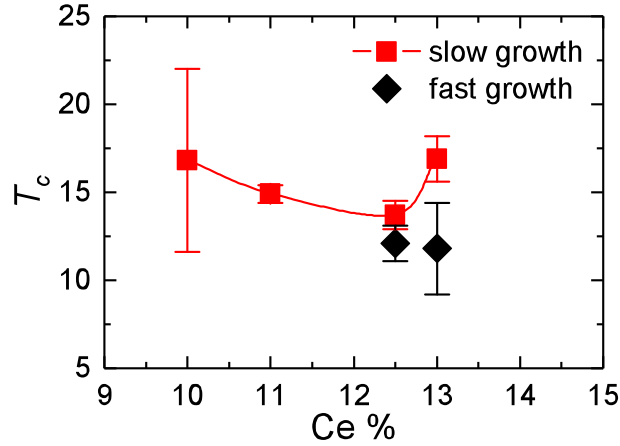


Figure 5.1:  $T_c$  of the samples studied in this work. Results for the fast and slow grown crystals are shown for  $x = 0.125$  and  $x = 0.13$  crystals.

Figure 5.1 shows a summary of the obtained  $T_c$  of all crystals synthesized in this work. A comparison to the  $T_c$  of the fast grown crystals is only done for the  $x = 0.125$  and  $x = 0.13$ . In the case of the  $x = 0.13$  samples the value of  $T_c$  depicted in Fig. 5.1 is after the first 20h of annealing. It should be noted that for the fast grown samples the  $T_c$  becomes higher with further annealing.

For the slow grown samples the  $T_c$  for  $x = 0.125$  is lower than for  $x = 0.13$ , however for lower dopant concentration,  $x = 0.11$  and  $x = 0.10$  the  $T_c$  increases. Such a decrease in the  $T_c$  at  $x = 0.125$  has been previously observed in the hole-doped superconductors. In these compounds the suppression of superconductivity has been explained by the presence of spin stripes [82]. However, no evidence of such phenomena was observed in the two samples measured for neutron diffraction and other reports have confirmed that the magnetic reflections in the electron-doped cuprates are commensurate [20, 23, 25]. Thus, the presence of spin stripes cannot be attributed to the decrease in  $T_c$  for this particular dopant concentration.

From the results presented in this work, it can be concluded that the superconducting properties of NCCO can be influenced by the growth conditions of the crystal. In all studied samples the use of a slow growth rate increased the  $T_c$  and the SC volume fraction. The sample properties along the rod diameter seem to have a slight gradient towards the center of the crystal rod. For example, the SC volume fraction decreases for the samples from the middle of the crystal, particularly in the case of  $x = 0.125$ . For the slow grown samples, the Ce concentration

slightly increases to the center of the rod which leads to an apparent contradictory relation to the SC volume fraction. The decrease in SC volume fraction at the center of the sample rod was also observed in the  $x = 0.13$  samples but less pronounced. For the  $x = 0.11$  samples the  $T_c$  and SC volume did not show any particular trend and for the 0.10 samples it was not possible to make a conclusion concerning this.

Considering the overall observations on the measured crystal properties, it can be inferred that the improvement of the SC properties is related to a reduced number of defects in the crystal lattice and a better distribution of oxygen in the  $\text{CuO}_2$  layers.

A second important conclusion from this work was the confirmation that a shorter annealing time is needed for the slow grown samples to induce superconductivity. Fast grown samples can take up to 80 hours while slow grown samples need a maximum of 40 hours, yet in some cases 20 hours is sufficient.

Furthermore, the issue of antiferromagnetism and superconductivity coexistence was analysed and briefly addressed in the particular case of the  $x = 0.125 - fg$  sample. The observation of long range AF order features together with superconductivity in the magnetoresistance could indicate coexistence of these two states. However, these data are insufficient to reach a conclusion. Considering the results from the magnetoresistance and that the high  $T_c$  and low  $T_N$  do not correspond to the measured dopant concentration, an electronic competition of these two states could be implied. However, it was also suggested that an alternative is the phase separation of better superconducting areas in the sample with AF regimes induced by the slow growth rate used to synthesize this crystal. Evidently, this issue requires further investigation to fully confirm either hypothesis.

The sample characterization presented in this work revealed new aspects of the properties of NCCO. Therefore, there are some unresolved issues which can now be addressed in a more focused manner. For example, during this work the generation of secondary phase in the samples was not reviewed. The presence of  $\text{Nd}_2\text{O}_3$  precipitations should be investigated to determine if samples from a slow grown crystal also develop this phase with annealing in the same quantities as other crystals or if such inconvenience can be reduced. Additionally, a structural study of as-grown samples from a slow growth process to analyze the occupancy

---

of the oxygen sites should be carried out. Furthermore, with samples of improved quality, a focused study on the change in oxygen occupancy due to the annealing process could be more informative.

In summary, the results presented in this work demonstrate that a slow growth rate is a very good alternative for a better and more controlled synthesis of NCCO single crystals. Although the growth process becomes more time consuming, the improved crystal properties compensate for this drawback. With samples of higher quality it is possible to conduct more reliable investigations for the characterization of the electron doped cuprate system and avoid sample dependent observations.



## Part II

# Angle-dependent Magnetoresistance of underdoped $\text{Nd}_{2-x}\text{Ce}_x\text{CuO}_4$



# 6 Introduction

The general aspects and structural characteristics of the electron-doped cuprates have already been covered in Part I. However, it is important to review some aspects which are more relevant to the study of their transport properties.

## 6.1 n-doped cuprates: general aspects of electronic and magnetic structure

The electron-doped cuprate  $\text{Nd}_{2-x}\text{Ce}_x\text{CuO}_4$  (NCCO) is known to be a superconductor in a doping range between  $x = 0.13 - 0.18$  [20]. The as-grown samples are insulating and must undergo a post-growth annealing treatment to become superconducting [20, 83]. The undoped parent compound  $\text{Nd}_2\text{CuO}_4$  (NCO) is a charge transfer insulator and shows a long-range antiferromagnetic (AF) order [20]. With increasing dopant concentration, the AF order is gradually suppressed and superconductivity sets in. Still, as discussed in Part I, in the phase diagram of the cuprate superconductors a clear asymmetry between the hole- and electron-doped sides is observed. Whether the AF and SC regimes coexist with each other is not fully understood.

Understanding the relation of antiferromagnetism or any other type of magnetic order with superconductivity in the electron-doped cuprates could be a crucial element for establishing the pairing mechanism in high- $T_c$  superconductivity [20, 34, 84].

### 6.1.1 Magnetic structure of the n-doped cuprates

The structure of the AF order of the electron-doped cuprates shows some differences with its hole doped counterpart. In the hole-doped cuprates, the Cu spins point  $\sim 45^\circ$  away from the Cu-O bond directions within the  $\text{CuO}_2$  layers and

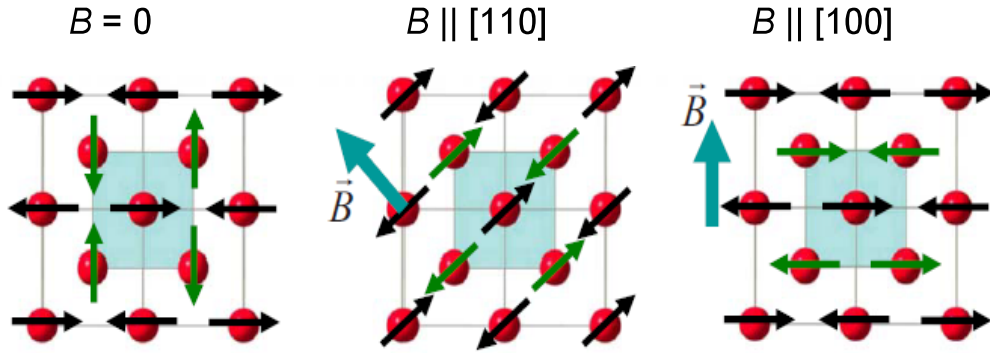


Figure 6.1: Magnetic structure of  $\text{Nd}_2\text{CuO}_4$ . From left to right: Noncollinear antiferromagnetic phase at zero field. Collinear phase above the spin crossover transition for a field parallel to the  $[110]$ . Collinear phase above the spin-flop transition for a field parallel to the  $[100]$  direction. Adapted from [20]. Only Cu-atoms of two adjacent layers (black and green arrows) are shown.

in adjacent layers they are parallel or antiparallel to each other [85, 86]. This arrangement is also referred to as collinear structure. On the other hand, in the case of the electron-doped cuprates, the spins lie along the Cu-O bonds and the staggered magnetization vectors in adjacent  $\text{CuO}_2$  layers are turned by  $90^\circ$  with respect to each other, i.e. in a noncollinear structure [20, 87, 88].

The undoped parent compounds of the electron-doped cuprates orders in a noncollinear structure at a temperature  $T_{N,\text{Cu}} \sim 270$  K. This structure is represented in the first panel of Fig.6.1. With decreasing temperature, below 100 K, the coupling of the Cu-Nd ions and competition between different interplanar interactions have a strong influence on the magnetic structure [89], which leads to the existence of three spin phases [87, 89–91]. In phases I and III, existing at temperatures between  $75 < T < 275$  K and  $T < 30$  K respectively, the Cu and Nd moments are parallel to each other along the  $[001]$  axis and exist. For a temperature range  $30 < T < 75$  K the moments of these two ions are antiparallel and this corresponds to phase II. An illustration of these temperature dependent spin phases is shown in Fig. 6.2. Although no explicit structural study has been conducted to determine if these spin phases are also present in the doped compounds, they are believed to exist in, at least, strongly underdoped NCCO [92].

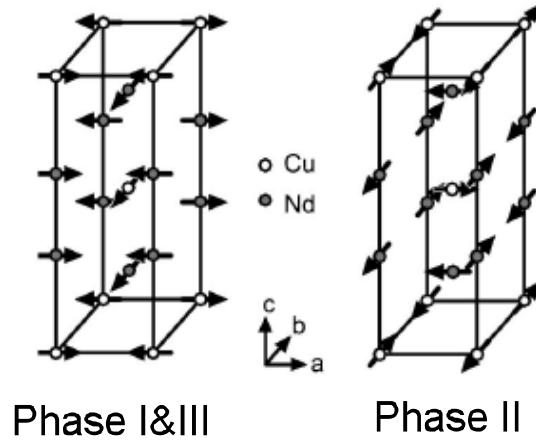


Figure 6.2: 3D magnetic structure of NCO. **Left:** Phases I&III ( $75 < T < 275$  K and  $T < 30$  K). **Right:** Phase II ( $30 < T < 75$  K). Adapted from [55].

A transformation from the noncollinear structure into the collinear one is possible if a magnetic field is applied parallel to the  $\text{CuO}_2$  planes. Particularly, if a field is applied in the  $[110]$  direction the spins rotate continuously to align themselves perpendicular to the field direction. This is known to be a second order transition which happens at a field  $B_c \simeq 1$  T [93, 94]. The collinear structure along the  $[110]$  direction is shown in the middle panel of Fig. 6.1. When the field is applied in the  $[100]$  direction, as shown in the right panel of Fig. 6.1, a first order spin-flop transition at a critical field  $B_c \simeq 4$  T occurs [94]. Furthermore, a study of the magnetic structure of  $\text{Pr}_2\text{CuO}_4$  [95] showed that for fields applied at intermediate orientations between  $[100]$  and  $[110]$ , the staggered magnetization firstly orients along  $[110]$  through a second order transition and, as the field increases, the spins rotate further to orient themselves more perpendicular to the field direction. As previously discussed, a first order spin-flop transition can only be achieved when the field is applied in the  $[100]$  direction and it was suggested that, at this field orientation, the staggered magnetization can only be exactly perpendicular to the field at a  $B \rightarrow \infty$ .

### 6.1.2 Transport properties

Due to the strong spin-charge coupling of the AF state of electron-doped cuprates, transport measurements are useful to probe transformations in the spin system. The magnetoresistance responds sensitively to changes in the magnetic structure such as the field induced spin-flop transition, mentioned in the last Section [11, 51, 96].

In this work the field- and angle-dependent magnetoresistance is measured. Magnetoresistance is a phenomenon where the resistance of a material changes with applied magnetic field. The magnetoresistance effect depends on the strength of the applied magnetic field and its direction with respect to the crystal axes and to the applied current. This is a probe of the conducting properties of the material, namely the magnetoresistance is directly related to the electron orbits at the Fermi surface (FS) [97].

An electron in a magnetic field  $\mathbf{B}$ , moving with velocity  $\mathbf{v}$ , is subject to the Lorentz force  $\mathbf{F}_L$ . The rate of change in the momentum of the electron,  $d\mathbf{p}/dt$ , is equal to:

$$\mathbf{F}_L = d\mathbf{p}/dt = e\mathbf{v} \times \mathbf{B}, \quad (6.1)$$

where  $\mathbf{p}$  is the electron's momentum and  $e$  is the electron charge [98, 99]. The Lorentz force affects only the momentum components which are perpendicular to the field while those in the field direction are constant. Since the Lorentz force is always perpendicular to  $\mathbf{v}$ , it does not change the electron's energy. Hence, in momentum space, the electron is moving on an orbit of constant energy perpendicular to the field direction. The velocity of the electron is related to the energy  $\epsilon_{\mathbf{p}}$  via  $\mathbf{v}(\mathbf{p}) = \delta\epsilon/\delta\mathbf{p}$ . The motion of the electron in its orbit is curved, and the relation:

$$\omega_c = \frac{eB}{m_e}. \quad (6.2)$$

is the angular frequency with which the electron circles its orbit, called cyclotron frequency. Thus the effect of the magnetic field is to increase the cyclotron frequency  $\omega_c$  of the electron. At low magnetic field  $\omega_c \ll 1$  the change in momentum  $\mathbf{p}$  is very small during the scattering time  $\tau$ , i.e. the electron only executes a small part of the cyclotron orbit. In the presence of an electric field, the trajectory of the electron is only slightly curved, which affects the resistivity, and thus

a magnetoresistance effect is observed. The relative change in resistivity is:

$$\frac{\rho(B) - \rho(0)}{\rho(0)} \equiv \frac{\Delta\rho(B)}{\rho(0)} \propto (\omega_c\tau)^2 \propto B^2 \quad (6.3)$$

This type of magnetoresistance is caused by the cyclotron orbits and is referred to as the orbital effect. Furthermore, if the unpaired spins of the system couple to the magnetic field, the scattering is spin dependent. Further effects include the case of spin-orbit coupling [98].

In the case of the electron-doped cuprates it is known that, in the optimally doped and overdoped regime, the magnetoresistance is mainly due to orbital effects, while in the moderately and strongly underdoped regime the behavior associated with spin-scattering dependent transport becomes more dominant [12, 44, 100]. The latter is the case discussed in this work.

An advantage of magnetotransport is that it is a selective probe of the conducting system. Transport gives information on the bulk of the sample, unlike other methods such as ARPES or scanning tunneling microscopy (STM) which mainly probe the sample surface. Other methods which directly measure the bulk magnetic structure, such as magnetisation or neutron scattering, often suffer from spurious contributions of the insulating magnetic precipitations  $\text{Nd}_2\text{O}_3$  caused by the heat treatment to induce superconductivity [32, 33].

Still, there are some unclear issues which complicate the description of the magnetoresistance effects. Various studies of the angle-dependent magnetoresistance (AMR) have considered the fourfold symmetry of the smooth part of the AMR as a signature of an AF order [101–103]. However, there are several different mechanisms which can lead to the observation of a smooth anisotropic magnetoresistance, for example, it can be due to a fourfold anisotropy of paramagnetic susceptibility. On the other hand, a twofold symmetry has also been attributed to the underlying AF order of the cuprate system [102]. However, the geometry of the in-plane resistance measurement can be the cause of this. Indeed, if the current is applied parallel to the conductive layers, the constant change in the angle between the field and the current results in a modification of the cross product  $\mathbf{v} \times \mathbf{B}$  in Eq. (6.1), which results in an angle dependence of the magnetoresistance. Therefore the observation of a two or fourfold symmetry in the AMR is not an unequivocal fingerprint of an AF order and such criteria should be reevaluated.

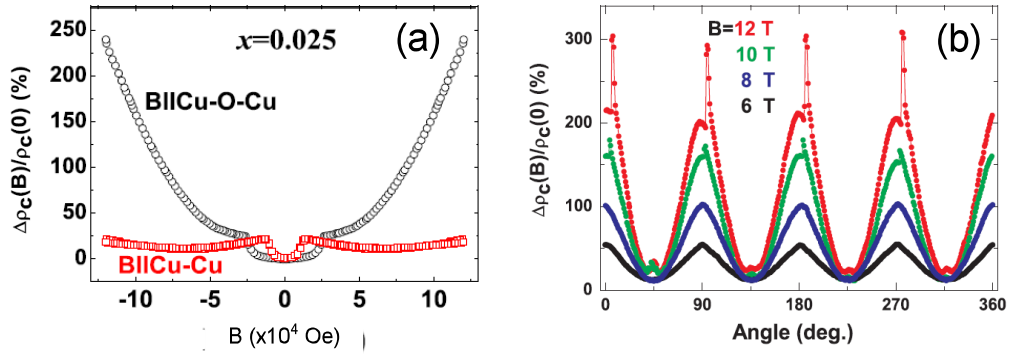


Figure 6.3: Interlayer magnetoresistance of a NCCO,  $x = 0.025$ , sample at 5 K. Reproduced from [11]. (a) Field-dependent magnetoresistance for a field oriented parallel to the conducting layers for the [100] (black) and [110] (red) directions. (b) Angular-dependent magnetoresistance measured at different magnetic fields.

On the underdoped side of the phase diagram of the electron-doped cuprates, a number of magnetoresistance studies have been conducted. Mainly the investigations have focused on strongly underdoped samples, i.e. with a dopant concentration closer to the undoped insulating parent compound. The transformation from noncollinear to collinear phase in NCCO and  $\text{Pr}_{1-x}\text{LaCe}_x\text{CuO}_4$  induced by a magnetic field has been detected in their field-dependent magnetoresistance (FDMR) [11, 51, 96]. For fields applied either in the [100] or in the [110] directions, a clear kink associated with this transition was observed. A large anisotropy in the smooth part of the FDMR was detected for  $\mathbf{B} \parallel [100]$  and  $\mathbf{B} \parallel [110]$ . As an example, the FDMR of a NCCO  $x = 0.025$  sample is shown in Fig. 6.3(a).

Under rotation of the magnetic field in the  $\text{CuO}_2$  plane, as illustrated in Fig. 6.3 (b), the AMR has a  $90^\circ$  periodicity [11, 91, 96, 104]. Furthermore, for fields  $B \geq 10$  T a sharp step-like feature with a pronounced hysteresis was found in the AMR of NCCO with  $x = 0.025$  and  $0.033$  for a field direction close to [100]/[010], and temperatures between  $2 \text{ K} \leq T \leq 5 \text{ K}$  [11]. Since the fields at which this feature was detected were much higher than the known spin reorientation transition for the  $\text{Cu}^{2+}$  system, this behavior was attributed to a transformation in the spin ordering of the  $\text{Nd}^{3+}$  sublattice [11].

Furthermore, during a former investigation done at the Walther-Meißner-Institute (WMI) [12], the FDMR and AMR of an underdoped NCCO sample with

a higher Ce concentration,  $x = 0.05$ , were measured. The field and angular sweeps are shown in Fig. 6.4 (a) and (b), respectively. At  $B_{c,\min} \approx 1$  T for  $\mathbf{B} \parallel [110]$  a kink was observed, indicating the reorientation of the  $\text{Cu}^{2+}$  spins between the noncollinear and collinear arrangement. For  $\mathbf{B} \parallel [100]$  a jump corresponding to the first order spin-flop transition was also detected at  $B_{c,\max} = 3.8$  T. Additionally, a similar but smaller difference of the FDMR between the  $[100]$  and  $[110]$  orientations, as the one observed in Fig. 6.3(a), was seen. It was concluded that this anisotropy becomes much smaller with increasing dopant concentration.

For the field rotations shown in Fig. 6.4 (b), the AMR at  $B = 1$  T oscillated with a  $90^\circ$  periodicity between a maximum at  $\mathbf{B} \parallel [110]/[1\bar{1}0]$  and minimum at  $\mathbf{B} \parallel [100]/[010]$ . With increasing field, the anisotropy was inverted. For fields  $1 < B < 3.5$  T the AMR became more flat around  $[110]$ . Still, around the  $[100]$  a dip was observed which collapsed at  $B \geq 4$  T. For fields above 8 T a hysteretic jump in the AMR around the  $[100]/[010]$  directions was observed. This anomaly resembles that observed in strongly underdoped crystals but its real origin was still not completely clear. For a better understanding of the origin of this high-field anomaly more information on its evolution with field strength and temperature, and its relation to dopant concentration is necessary.

To investigate the origin of the step-like feature observed in transport measurements done on strongly underdoped NCCO [11] and in former investigations at WMI, the interlayer field- and angle-dependent magnetoresistance of underdoped NCCO single crystals was carried out. In this work, the focus was to measure the FDMR and AMR of samples with higher Ce concentration, within the doping range  $0.09 \leq x \leq 0.13$ , which corresponds to the regime where the long-range AF order borders the bulk superconducting in the phase diagram. Besides evidence of the transition between the collinear and noncollinear states in the field- and angle-dependent magnetoresistance, the anomalous behavior in the high-field collinear state at field orientations around the  $[100]$  direction was observed. This step-like feature is similar to the hysteretic anomaly reported earlier for strongly underdoped NCCO. However, it is found to persist at temperatures strongly exceeding the Néel temperature of the  $\text{Nd}^{3+}$  system and thus a qualitative explanation of this anomaly is proposed based on the model of the field-dependent orientation of  $\text{Cu}^{2+}$  spins in the collinear state. The high-field hysteretic behavior was found on both the non-superconducting and SC samples

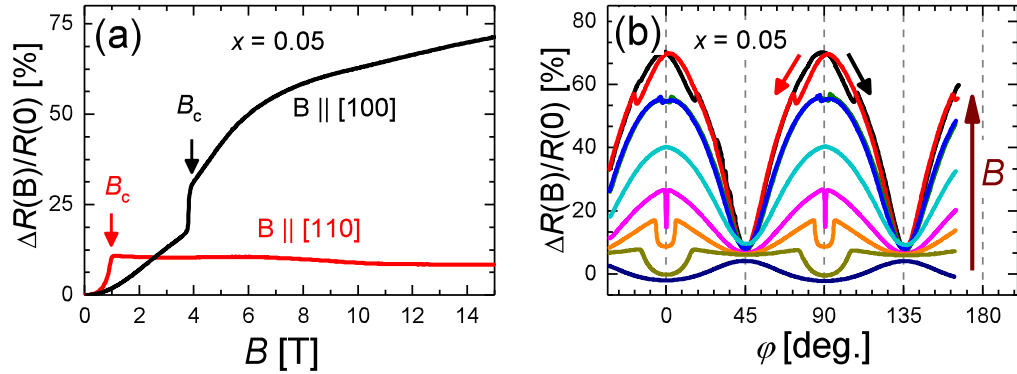


Figure 6.4: Interlayer magnetoresistance of a NCCO,  $x = 0.05$  sample, at  $T = 1.4$  K measured at the WMI [12]. (a) FDMR for a field oriented parallel to the conducting layers in the [100] (black) and [110] (red) directions. The arrows indicate the critical transition field  $B_c$  for each field direction. (b) AMR for the same sample at different field strengths. The AMR was measured for different fields  $B = 1, 1.5, 3, 4, 5, 8$  and  $15$  T. The black and red arrows indicate the angular sweep direction for the curves of the respective color. The vertical arrow (dark red) shows the increment of the field strength.

in this work, which points to the coexistence of superconductivity and antiferromagnetism, at least, near the lower edge of the SC doping range.

# 7 Experimental details

The field and angular dependence of the out-of-plane magnetoresistance was measured for underdoped NCCO samples with  $x = 0.09 - 0.13$ . The measurement of the interlayer resistance instead of the in-plane resistance has some advantages. The electron-doped cuprates are highly anisotropic materials; the ratio of the out-of-plane and in-plane resistance is of the order of  $\rho_c/\rho_{ab} \approx 10^3$  [20, 105] and thus  $\rho_c$  is easier to measure. A practical disadvantage of measuring the in-plane  $\rho_{ab}$  is that due to cracks, cavities or insulating precipitations in the lattice, the scattering processes are more susceptible to be affected by interlayer components. To avoid this effect, the sample would have to be thinned down to the order of  $1 \mu\text{m}$  and unfortunately this would also result in a very brittle sample. Furthermore, the measurement of the angle-dependent in-plane resistance can be misleading because the vector product  $\mathbf{v} \times \mathbf{B}$  from the Eq. (6.1) would constantly change as the field is rotated. By measuring the interlayer resistance, the applied current is always perpendicular to the field applied parallel to the layers and is, thus, more suitable for studying the intrinsic electronic anisotropy.

## 7.1 Samples: preparation and contacts

The crystals were grown with the traveling solvent floating zone (TSFZ) method, as described in Ref. [30]. From the as-grown crystal rod, samples were cut out in a shape which maximized the interlayer direction and minimized the cross section with approximately  $0.3 \times 0.3 \times 1 \text{ mm}^3$ . The longest dimension corresponded to the [001] ( $c$ -axis) crystallographic direction. The samples  $0.09 \leq x \leq 0.115$  were annealed in an argon atmosphere for 20 hours and the  $0.12 \leq x \leq 0.13$  for 40 hours, unless stated differently, according to the dopant concentration at temperatures:  $900^\circ\text{C}$  for  $x = 0.09$  and  $0.10$ ,  $910^\circ\text{C}$  for  $0.115 \leq x \leq 0.125$  and  $935^\circ\text{C}$  for  $x = 0.13$  [21, 54]. Two samples of  $x = 0.12$  will be presented in this thesis. The

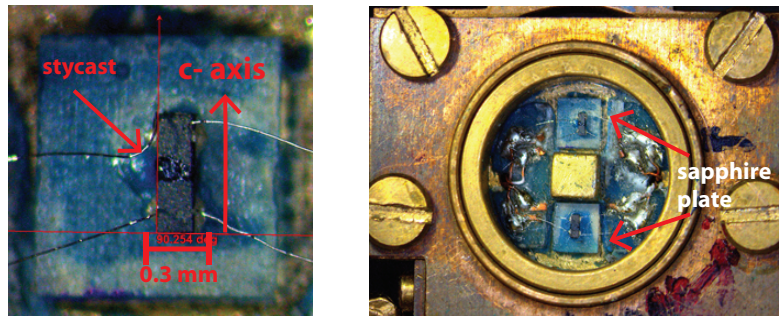


Figure 7.1: Contacted and mounted NCCO crystals for interlayer transport measurements, done under optical microscope. **Left:** Close-up of a contacted sample, glued with Stycast. The arrow indicates the direction of the [001] crystallographic axis. **Right:** Two samples glued with Stycast to the sapphire plates, mounted on the two-axis rotator.

two samples with  $x = 0.125$  were already discussed in Part I and here the results corresponding to this dopant concentration refer to the slow-grown sample.

The electric contacts were made manually under the microscope. The process, to achieve optimal contact resistances in the range  $5 - 30 \Omega$  or less, consists of several steps. A pair of carefully annealed Pt wires of  $20 \mu\text{m}$  diameter are fixed to two opposite sides of the sample using conducting two-component Ag-based epoxy, EpoTek H20E as described in Refs. [12, 44]. The sample should be heated in air up to  $140^\circ \text{C}$  for one hour to dry the fresh contacts. This is followed by another heat treatment at  $500^\circ \text{C}$  for one hour and a cooling-down ramp of  $100^\circ \text{C}/\text{h}$ . The heating leads to a strong decrease of the contact resistance; however, the mechanical stability of the contacts significantly worsens. Therefore, the contacts are subsequently reinforced by adding the silver epoxy paste and heating again at  $140^\circ \text{C}$  for one hour. The contacted samples were glued on a sapphire plate with the [001] axis of the sample parallel to it. The adhesive used for this is Stycast 2850 FT prepared with catalyst 24 LV. Due to its high thermal conductivity and small thermal expansion, it is an ideal glue for these experiments. An illustration of contacted and glued samples is seen in Fig. 7.1.

## 7.2 The rotating system

The contacted sample was mounted so that the [001] direction would be the rotating axis, and then put in a sample holder in a two-axes rotator constructed by T. Helm and D. Andreas at the WMI [12, 106]. As a result of this configuration, the *in situ* rotation of the samples with respect to a magnetic field  $\mathbf{B}$  was possible. A picture of the rotator is presented in Fig. 7.2(a). It shows two different rotation directions which can be manipulated. The one labeled  $\theta$  is controlled by a piezo-electric motor on the top of the insert outside the cryostat. The angle labeled  $\varphi$  is adjusted with a screwdriver and can be decoupled from the platform. For the purpose of this work, only rotations of the  $\text{CO}_2$  plane were performed. This was done by the mechanical rotation of the angle  $\theta$  of the two-axis rotator shown in Fig. 7.2 (a). This rotator provides an angular accuracy of  $\pm 0.01^\circ$ . To optimize the sample alignment, so the sample c-axis would be as perpendicular as possible to the field direction, the angle  $\varphi$  of Fig. 7.2 (a) was adjusted with the screwdriver to an accuracy of  $\pm 0.2^\circ$ . Due to the manual set up of the samples on the sample holders, a misorientation smaller than  $5^\circ$  was not uncommon but it could be compensated by in-situ rotation of the sample. The effects of the sample misalignment were small shifts in the values of the critical fields  $B_c$  in the FDMR and a slight asymmetry in the measured AMR (see, for example inset in Fig. 2.21).

A definition of the angles with respect to the crystallographic axes of the sample is shown in Fig. 7.2(b). The angle  $\theta$  was always set equal to  $90^\circ$ , thus the field was directed parallel to the (001) plane and its orientation was defined by the azimuthal angle  $\varphi$ :  $\varphi = 0^\circ$  is defined as equivalent to  $\mathbf{B} \parallel [100]$  and  $\varphi = 45^\circ$  to  $\mathbf{B} \parallel [110]$ . The field was rotated as a function of angle  $\varphi$  of Fig. 7.2(b). This angle  $\varphi$  should not be confused with the one from the two-axes rotator. Henceforth, the angle  $\varphi$  will refer to the angle between the applied magnetic field parallel to the  $\text{CuO}_2$  layers and the crystallographic axes as defined in Fig. 7.2(b).

### 7.2.1 The experimental setup

The interlayer resistance  $R_c$  was measured using the a.c. 4-probe method to assure a correct measurement of the sample resistance without measuring the contact and lead resistances. The current was obtained by a lock-in amplifier's oscil-

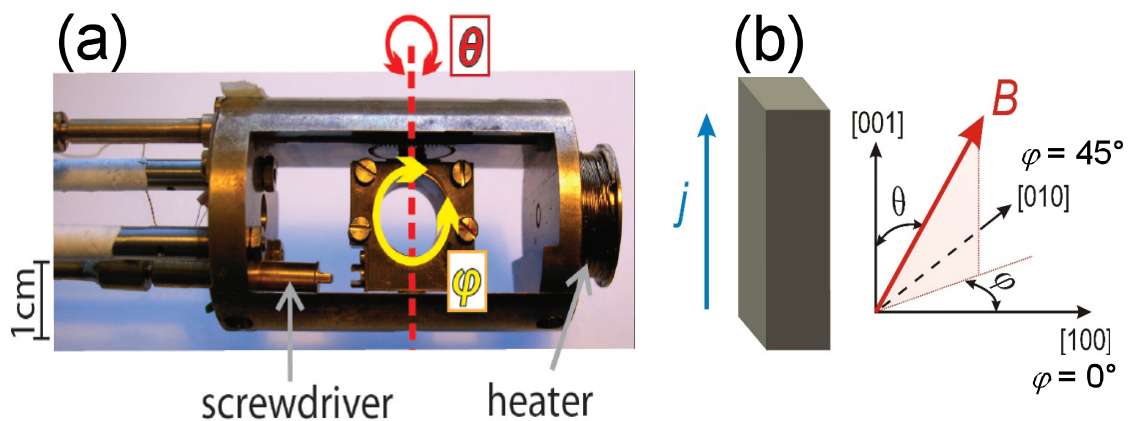


Figure 7.2: (a) Illustration of the two-axes rotator used in this work and definition of the rotator angles. Variation of the angle  $\theta$  was controlled by the piezo-electric motor. The screwdriver was used to adjust the angle  $\varphi$ . (b) Definition of the sample angles in relation to the crystallographic axes. For the sample angles:  $\theta$  is the angle between the  $c$ -axis and the field direction, and  $\varphi$  is the angle between the field direction and the  $[100]$  direction. The angles  $\theta$  and  $\varphi$  for the rotating system in (a) should not be confused with the sample angles with the same label in (b). In this work, only in-plane rotation was performed, which corresponds to the sample angle  $\varphi$  as defined in (b). The angles are defined as  $\varphi = 0^\circ$  as equivalent to  $\mathbf{B} \parallel [100]$  and  $\varphi = 45^\circ$  for  $\mathbf{B} \parallel [110]$

lator output<sup>1</sup>. A high-ohmic resistor (100 k $\Omega$ ) is connected in series to the internal a.c. voltage generator of the lock-in amplifier. The current, adjusted with the output voltage from the lock-in amplifier, is applied to one pair of the sample contacts. With the other pair of contacts, the voltage is measured to obtain the sample resistance. The sample is connected in series to a reference resistor, of either 10  $\Omega$  or 100  $\Omega$ , which was used for the fine tuning of the current. The resistance of the high-ohmic resistor  $R_{\text{high}}$  is much bigger than the reference,  $R_{\text{ref}}$ , and sample,  $R_{\text{sample}}$ , resistances and thus they can be neglected. Therefore, the measured current was  $I_{\text{meas}} = U_{\text{osc}}/R_{\text{high}}$ . This current is considered constant and stable despite the temperature and field dependence of the sample and leads resistance. The measured current is adjusted and the sample resistance is evaluated by  $R_{\text{sample}} = U_{\text{sample}}/I_{\text{meas}}$ .

For the application of a steady magnetic field up to 14 T, a <sup>4</sup>He superconducting magnet system from Cryogenics Ltd. was used. The magnet consists of two concentric superconducting coils, the outer one made of NbTi and the inner one of Nb<sub>3</sub>Sn. The coils are cooled in a liquid <sup>4</sup>He bath in a cryostat. The external current was applied by a superconducting magnet power supply Oxford IPS 120–10. For the temperature control a variable temperature insert (VTI) was used as described in Ref. [107], and resistive temperature sensors, Cernox and RuOx, were used. The thermometers were measured by a LakeShore Model 340 temperature controller or by AVS45/46 resistance bridges from Picowatt.

### 7.3 Measurement sequence

Measurements of the interlayer resistance  $R_c$  were carried out at fields  $B \leq 15$  T, in the temperature interval 1.4 to 115 K. The field-dependent magnetoresistance was measured by performing field sweeps with a field parallel to the Cu–O–Cu (crystallographic [100] or [010] axis), Cu–Cu ([110]/[1 $\bar{1}$ 0] axis), and some intermediate directions within the layer plane (see Section 7.2). The angle-dependent magnetoresistance was measured in a steady magnetic field by rotation in the CuO<sub>2</sub> layers as a function of the azimuthal angle  $\varphi$ . The strength of the magnetic field will be specified when necessary, in most cases and for comparison purposes the field used in the rotation experiments was  $B = 14$  T. The field de-

<sup>1</sup>Stanford Research Systems DSP, model 830

pendence of the resistance measured during the field sweeps will be referred to as FDMR and the angular dependence of the resistance as AMR. In accordance with the tetragonal crystal symmetry of NCCO and the axial symmetry with respect to the applied current direction, the AMR showed a  $90^\circ$  periodicity. Therefore, in what follows, the discussions regarding the directions  $[100]$  and  $[110]$  are also valid for the equivalent directions  $[010]$  and  $[\bar{1}\bar{1}0]$ , respectively.

## 8 Results

For a better overview of the results obtained in this work, they will be separated into two sections: non-superconducting (non-SC)<sup>1</sup> and superconducting (SC) samples, respectively. Figure 8.1 shows the zero-field temperature dependence of the resistance  $R_c$  of the NCCO samples. The resistance is normalized to the room temperature resistance  $R(300\text{ K})$ . The samples  $0.09 \leq x \leq 0.115$  were non-superconducting (non-SC). The resistance of the  $x = 0.115$  sample showed a tiny,  $\approx 3\%$  downturn below  $T = 7.7\text{ K}$ . Although this indicates the presence of a very small fraction of superconducting volume, this sample is referred to as non-SC.

The  $0.12 \leq x \leq 0.13$  samples showed a superconducting transition. Two  $x = 0.12$  samples are shown, sample  $x = 0.12(a)$  was annealed for 60 hours and  $x = 0.12(b)$  for 40 hours. This was done to test if annealing time influenced the observation of the hysteretic step-like feature of the AMR. The main comparison between the two samples is presented in Section 8.3. By measurement of the magnetic susceptibility of the SC samples, the SC volume fraction was estimated, as it was described in Part I. The samples  $x = 0.12(a)$  and  $x = 0.13$  had the largest superconducting fraction, close to 100%. The samples  $x = 0.125$  and  $x = 0.12(b)$  had an estimated 69.5% and 20% SC fraction, respectively. The SC transition of the  $x = 0.12(b)$  is broader than the transition of  $x = 0.12(a)$  and it does not show zero resistance at the lowest temperatures. This behavior clearly indicates the presence of both bulk SC and non-SC phases in the crystal.

---

<sup>1</sup>For comparison purposes, the results on the sample  $x = 0.05$  obtained in Ref. [12] shown in Fig. 6.4 will be considered. Additional measurements on a  $x = 0.10$  sample can be found in Ref. [13]

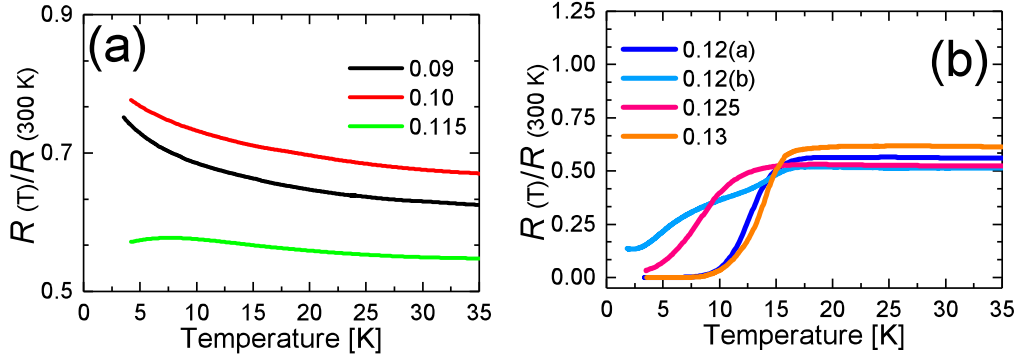


Figure 8.1: Normalised  $R$  versus  $T$  for NCCO underdoped single crystals. (a) Non-superconducting samples with  $x = 0.09 - 0.115$ . (b) Superconducting samples with  $x = 0.12 - 0.13$ . Two samples of  $x = 0.12$  are shown, the sample  $x = 0.12(b)$  is less superconducting.

## 8.1 Non-superconducting NCCO samples

Figure 8.2 presents the low-temperature FDMR of the  $x = 0.09$  and  $x = 0.115$  samples, for a magnetic field applied in the  $[100]$  and  $[110]$  directions. The FDMR is defined as  $\Delta R(B)/R(0) \equiv R(B) - R(B = 0)/R(B = 0)$ . For sample  $x = 0.10$  a behavior very similar to sample  $x = 0.09$  was observed. The magnetoresistance became more negative with increasing field for the samples  $x = 0.09$  and  $x = 0.10$ . In the case of sample  $x = 0.115$ , the magnetoresistance first increases by 2% and 1% for the  $[110]$  and  $[100]$  directions, respectively. This shoulder-like shape at  $B < 3\text{ T}$  is most likely related to the small fraction of superconductivity already discussed in the beginning of this chapter. Between 2.3–2.6 T the resistance starts to decrease and then it has a slight bending upwards around 5–8 T.

In the field sweep, both samples show a clear kink at  $B_c = 1\text{ T}$  for  $\mathbf{B} \parallel [110]$ , which is pointed out by the vertical red arrow in Fig. 8.2. This corresponds to the second order transition from the noncollinear to the collinear phase. A similar feature was observed in the same field range for the  $x = 0.05$  sample [12] depicted in Fig. 6.4 in Section 6.1.2 and it has also been reported for even lower doped samples where AF order is present [11, 51, 96].

For  $\mathbf{B} \parallel [100]$ , the transformation between the noncollinear and collinear states at  $B_c$  is less evident for the non-SC samples presented in this work. Such is the case of sample  $x = 0.09$  shown in Fig. 8.2(a). As a reminder, for this field orien-

tation, the FDMR of sample  $x = 0.05$  showed a distinct jump at  $B_c = 3.8$  T [12]. For higher Ce concentrations, the field-derivative of the resistance, shown in the inset of Fig. 8.2(a), has a step at  $\approx 3.8$  T which is likely associated with this transition. This was the same for sample  $x = 0.10$ . Unfortunately, due to the small fraction of superconductivity in sample  $x = 0.115$ , the shape of the FDMR was quite unusual and did not allow to observe the field effects on the underlying AF order.

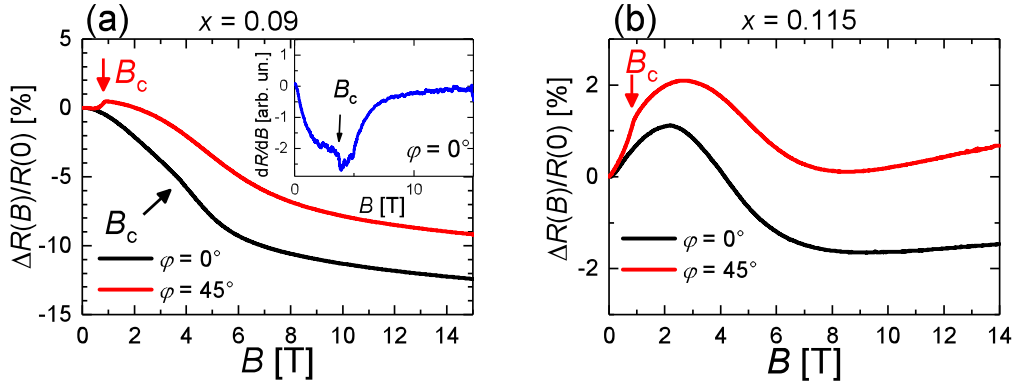


Figure 8.2: Field-dependent magnetoresistance of underdoped non-SC NCCO samples at  $T = 1.4$  K with  $x = 0.09$  (a) and  $x = 0.115$  (b). The inset in (a) shows the derivative  $dR/dB$  for the  $x = 0.09$  sample in field along the  $[100]$  direction.  $B_c$  is the critical field of the transition between the noncollinear and collinear AF spin configurations.

Considering the data of the FDMR in Fig. 6.4, the smooth part of magnetoresistance for the  $x = 0.05$  sample shows very different behaviors at  $\mathbf{B} \parallel [100]$  and  $\mathbf{B} \parallel [110]$ . In the former, the FDMR has a strong positive slope above the  $B_{c,max}$ , while in the second case the FDMR stays more or less flat with increasing field. A qualitatively similar, though somewhat stronger, anisotropy has been found on lower doped samples,  $x = 0.025$  and  $0.033$  [11, 96] as well as on low-doped  $\text{Pr}_{1.3-x}\text{La}_{0.7}\text{Ce}_x\text{CuO}_4$  [51]. However, as doping is increased to  $x = 0.09 - 0.115$ , this anisotropy becomes much weaker and even inverts; the  $\Delta R(B)/R(0)$  curves have negative slopes and follow an almost parallel field dependence, only saturating towards high fields. This confirms the suggestion made in Ref. [12], that the anisotropy of the FDMR for these two relevant directions becomes smaller with increasing dopant concentration.

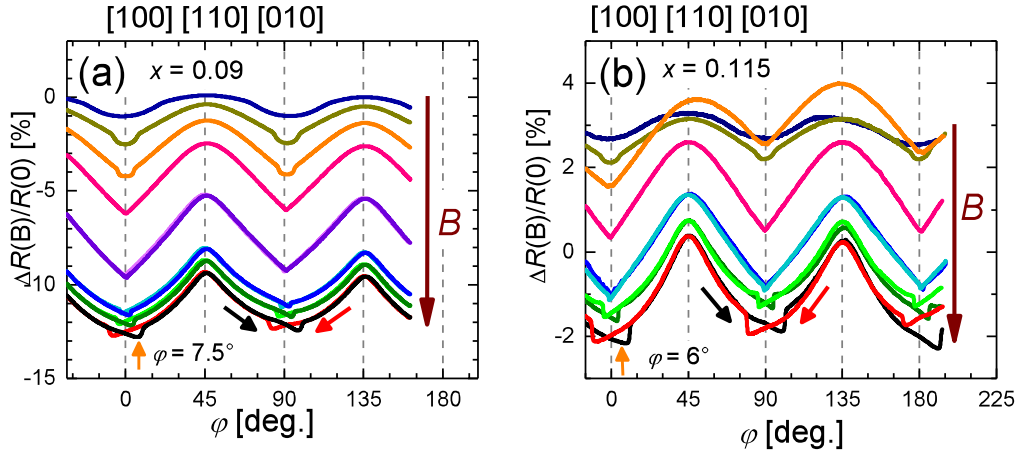


Figure 8.3: AMR of non-SC samples with  $x = 0.09$  and  $x = 0.115$  at  $T = 1.4$  K for field rotations in the plane of  $\text{CuO}_2$  layers at different field strengths: a) AMR of  $x = 0.09$ . The field is (top to bottom):  $B = 1, 1.5, 3, 4, 5, 8$  and  $15$  T. b) AMR of  $x = 0.115$ . The field is (top to bottom):  $B = 1, 2, 3, 4, 6, 10$  and  $14$  T. The black and red arrows indicate the angular sweep directions. The orange arrows indicate the angle  $\varphi$  where the field sweeps in Fig. 8.9 were done.

In Fig. 8.3 (a) and (b) the AMR for the  $x = 0.09$  and  $x = 0.115$  samples at  $T = 1.4$  K and different magnetic fields  $1 \text{ T} \leq B \leq 15 \text{ T}$  are shown<sup>2</sup>. The three non-SC samples,  $x = 0.09 - 0.115$ , showed very similar behaviors. Below  $\sim 5$  T the AMR patterns are fully consistent with the FDMR shown in Fig. 8.2. At  $B = 1$  T, as the field orientation is varied within the  $ab$ -plane, the magnetoresistance oscillates with a  $90^\circ$  periodicity between a minimum at  $\mathbf{B} \parallel [100]$ , corresponding to the noncollinear spin arrangement, to a maximum at  $\mathbf{B} \parallel [110]$ , where the collinear AF state is already more stable at this field. With increasing field the fourfold symmetry is maintained and the AMR becomes more negative, as expected from the FDMR shown in Fig. 8.2. In the case of sample  $x = 0.115$  at  $B = 3$  T, consistently with the increase in  $R_c$  seen during the field sweeps, the AMR also increases. For fields  $1 \text{ T} < B < 3.5 \text{ T}$  the collinear state becomes more stable in an increasingly broader angular interval around  $[110]$ . At the same time, the stability range of the noncollinear state around the  $[100]$  becomes more narrow, which is manifested in a narrowing of the dip in the AMR around  $[100]$ : the

<sup>2</sup>The AMR of sample  $x = 0.115$  was measured for fields up to  $B = 14$  T.

spin-flop feature, seen very clearly in the AMR of the  $x = 0.05$  sample in Fig. 6.4, but also for  $x = 0.09$  and  $x = 0.115$ , shifts towards [100] and eventually collapses at  $B > B_{c,\max} = B_c(\varphi = 0^\circ)$ . At 4 T the AMR around [100] has a sharp and fully reversible minimum. This is clearly observed in the AMR curves of both samples (pink) in Fig. 8.3. For sample  $x = 0.05$ , there is still a very narrow dip at  $B = 4$  T, indicating that the real spin-flop field  $B_{c,\max}$  is slightly higher than the value 3.8 T obtained from the field sweep shown in Fig. 6.4(a). The discrepancy is caused by a small  $\approx 1^\circ$  tilt from the exact [100] direction during the field sweep. Due to the strong angular dependence of  $B_c$  near [100] such a tilt reduces it by  $\sim 0.2 - 0.3$  T.

Moreover, at fields  $B \geq 6$  T, a new feature emerges in the AMR around the [100] direction. Now the resistance minimum shifts from the exact [100] position. As the angle increases from negative values (black curves in Fig. 8.3), the resistance continues to decrease as the field passes through the directions corresponding to  $\varphi = 0^\circ/90^\circ$ . With continuing rotation, at a critical angle  $\varphi^*$ <sup>3</sup> the resistance sharply jumps up. The same jump is observed upon decreasing  $\varphi$  from the positive side, through  $0^\circ$ , at  $-\varphi^*$ . Thus, the AMR exhibits a hysteresis in the angular range  $\Delta\varphi \approx 2\varphi^*$  around the [100]/[010] directions. Beyond this interval the angular dependence is fully reversible. The width of the hysteresis  $\Delta\varphi$  increases with increasing magnetic field, for example for the  $x = 0.09$  sample, it changes from  $\Delta\varphi \approx 2^\circ$  at  $B = 6$  T to  $\Delta\varphi = 18.5^\circ$  at  $B = 15$  T. The field dependence of the hysteresis width for sample  $x = 0.09$  at different temperatures is depicted in Fig. 8.4.

Despite the opposite overall AMR anisotropy, the anomaly around  $\varphi = 0^\circ/90^\circ$  observed for the samples of this work, and even in sample  $x = 0.05$  [12], resembles the sharp hysteretic feature reported in strongly underdoped NCCO samples,  $x = 0.025$  and  $x = 0.033$  [11]. However, the latter measurements were done at temperatures lower than 5 K. Hence, for a better understanding of the temperature dependence of this anomaly, the AMR of all samples in this work was measured at  $T \geq 4.2$  K. Figure 8.5 illustrates a nonmonotonic variation of the hysteretic step-like feature at three different temperatures, for the samples  $x = 0.09$  and  $x = 0.115$ .

At increasing temperature, the  $90^\circ$  periodicity of the AMR is maintained, while its amplitude decreases. In the main panel of Fig. 8.5 (a) a clear hysteresis is ob-

<sup>3</sup> $\varphi^*$  is taken from the middle of the step in the high-field AMR around [100].

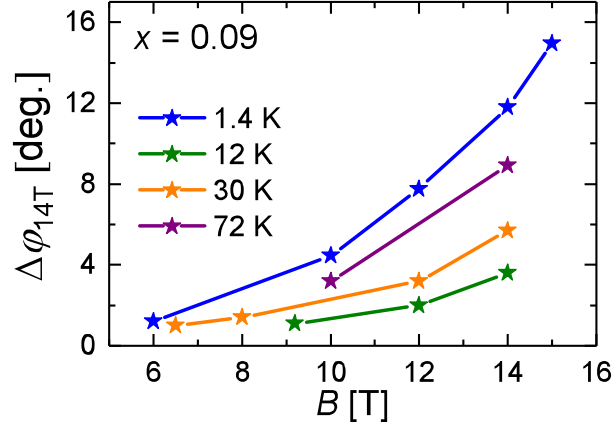


Figure 8.4: Field dependence of the hysteresis  $\Delta\varphi$  of the  $x = 0.09$  sample at different temperatures. Here  $\Delta\varphi = \varphi_{\text{up}}^* - \varphi_{\text{dn}}^*$ .

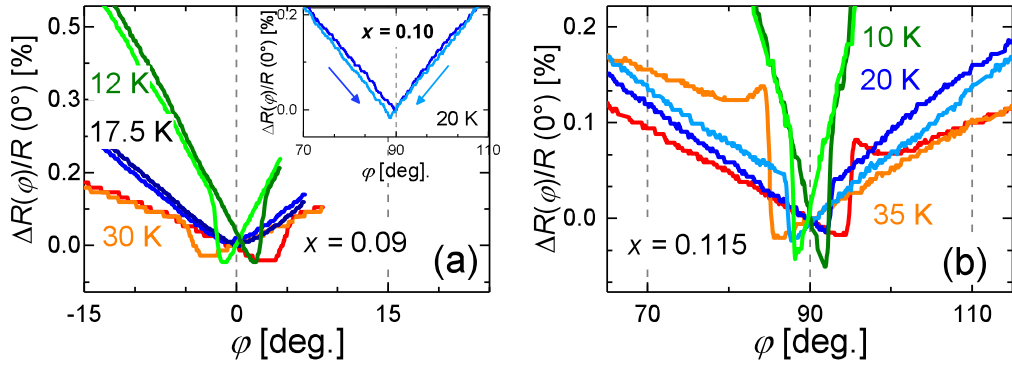


Figure 8.5: Close-up of the hysteresis in the AMR of two underdoped NCCO samples at 14 T and different temperatures. The magnetoresistance here is defined as  $\Delta R(\varphi)/R(0^\circ) = R(B, \varphi) - R(B, \varphi = 0^\circ)/R(B, \varphi = 0^\circ)$ . (a)  $x = 0.09$  at  $T = 12, 17.5,$  and  $30$  K. The inset shows a close-up of the 14 T AMR of the  $x = 0.10$  sample at  $T = 20$  K. The arrows indicate the directions of rotation. (b)  $x = 0.115$  at  $T = 10, 20,$  and  $35$  K.

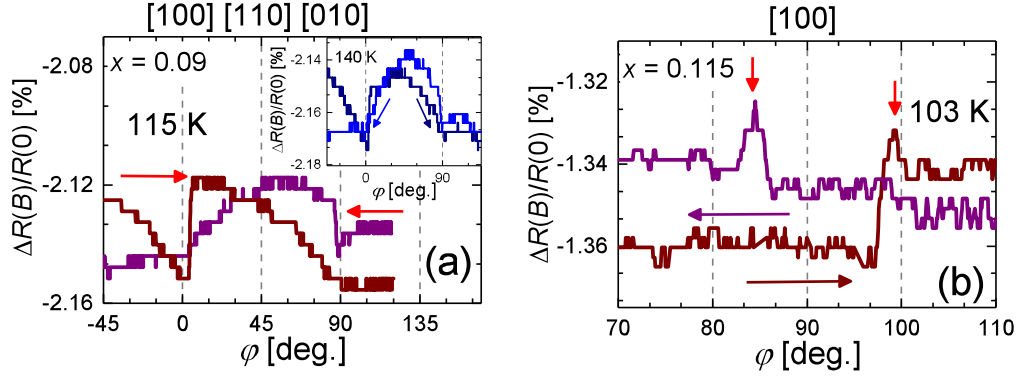


Figure 8.6: AMR of underdoped NCCO samples at  $T > 100$  K, 14 T. (a)  $x = 0.09$  at  $T = 115$  K. The inset shows the AMR of the same sample at  $T = 140$  K. The dark blue arrows indicate the direction of the rotation. (b) Close-up of the AMR around the [010] direction for the  $x = 0.115$  sample at  $T = 103$  K. The red arrows in both panels point to the step-like feature.

served at 12 K (green lines) for sample  $x = 0.09$ . At this temperature the anomaly is similar to that at 1.4 K, although the height of the resistance step is about 2 times smaller and the hysteresis width is reduced to  $\Delta\varphi \approx 3^\circ$ . At 17.5 K (dark blue lines) it seems to vanish but reappears at 30 K (orange-red lines) and becomes broader than at 12 K. Similarly, in the inset of Fig. 8.5 (a), the hysteresis in the AMR is also almost collapsed at 20 K for sample  $x = 0.10$ , which, as well as in the other two samples, reappears at higher temperature (not shown in Figure). In the case of sample  $x = 0.115$  the hysteresis is very narrow at 10 K and only slightly wider at 20 K, but at 35 K the hysteresis is broader than at these two other temperatures.

Above 35 K the size of the resistance step continuously decreases together with the overall AMR amplitude; however it can be traced as long as the angular variation of the magnetoresistance is reliably measured. For example, in Fig. 8.6 (a) and (b), clear steps near the [100]/[010] directions can still be resolved at 115 K and 103 K for the samples  $x = 0.09$  and  $x = 0.115$ , respectively. An apparent breakdown of the  $90^\circ$  periodicity is observed in Fig. 8.6(a). This is most likely caused by small temperature fluctuations and weak misalignment of the crystal. The persistence of the AMR step-like feature was confirmed by the performance of several angular sweeps in this and in the other samples. For sample  $x = 0.115$  the  $90^\circ$

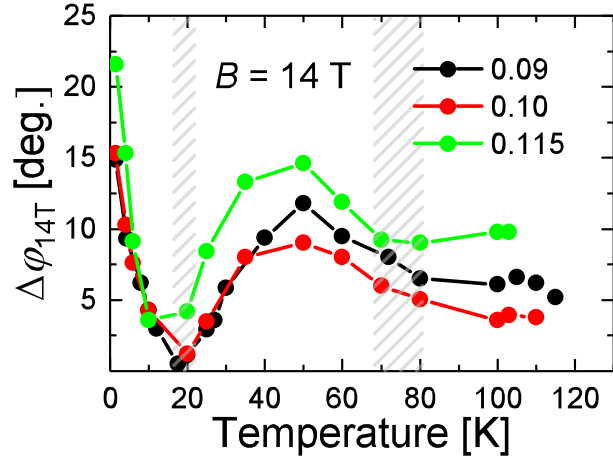


Figure 8.7: The width of the hysteresis in the AMR recorded at  $B = 14$  T, as a function of temperature, for three non-SC samples. The hatched boxes divide the diagram in three parts with different behavior of  $\Delta\varphi(T)$ .

periodicity is still observed at the highest temperature. For samples  $x = 0.09$  and  $x = 0.10$ , the AMR could still be measured at  $T = 140$  K, see inset in Fig. 8.6(a). However, the step-like feature is hardly discernable at such high temperatures since the amplitude of the AMR is already at the border of experimental accuracy. In the case of sample  $x = 0.115$  in Fig. 8.6 (b) a close-up of the the step-like feature is shown, which at 103 K has a peak-like shape.

Figure 8.7 depicts the overall temperature dependence of the hysteresis width for 14 T,  $\Delta\varphi_{14T}(T)$ , of the non-SC samples. It becomes evident that all the non-SC samples showed very similar behavior. From low to high temperature, the hysteresis  $\Delta\varphi$  is widest at  $T = 1.4$  K. It then narrows with increasing temperature, and possibly even vanishes at a temperature slightly below 20 K. Above 20 K, the hysteresis reappears and grows with temperature showing a broad maximum at  $\sim 50$  K. For temperatures  $50 \text{ K} < T < 70 \text{ K}$ ,  $\Delta\varphi$  tends to shrink and eventually saturates at a level of 5-10° above 70 K.

Furthermore, the hysteretic behavior of the AMR gives rise to an interesting memory effect in the FDMR. To observe it, a certain measuring sequence must be followed. To illustrate this effect, a sequence of low- $T$  field sweeps for the non-SC samples is shown in Figs. 8.8<sup>4</sup> and 8.9. Considering Fig. 8.8(a), the measuring

<sup>4</sup>Figure 8.8 corresponds to a  $x = 0.10$  sample studied by Ahmed Alshemi at the WMI [13]. The FDMR revealed a likely presence of excessive oxygen typical of insufficiently annealed NCCO

sequence was performed as follows: at  $T = 1.4\text{K}$  a field sweep up is done at  $\varphi_0 = -0.6^\circ$  (curve 1). At a constant field  $B = 14\text{T}$ , the field is rotated to a positive angle  $\varphi_1 = 10^\circ$ . At this angle the field is driven out (curve 2).

In Fig. 8.8 (a), for the field down sweep (curve 2), the resistance increases as the field decreases from  $B = 14\text{T}$ . In the high-field region, at  $B^* \approx 10.5\text{T}$ , the FDMR exhibits a step. Below this point the FDMR changes the slope and increases monotonically. At lower fields the kink feature associated with the transition between the noncollinear and collinear spin structures is observed. Once at  $B = 0\text{T}$ , the field was increased again (curve 3) and subsequently decreased (curve 4) without any intermediate change in the orientation. The two subsequent field sweeps up and down (curves 3 and 4) done at the same orientation show a fully reversible behavior. The kink at  $B_c$  is observed in the low-field region but in the high-field regime the FDMR does not show any sign of the high-field step.

In the case of samples  $x = 0.09$  and  $x = 0.115$  only the curves corresponding to the down-sweeps are depicted in Fig. 8.9, together with the up-sweep at  $\varphi = 0^\circ$ . The angles  $\varphi = 7.5^\circ$  and  $\varphi = 6^\circ$  at which these curves were recorded are indicated with the vertical orange arrows in Fig. 8.3(a) and (b), respectively. The sample  $x = 0.09$  was first turned in a magnetic field of  $15\text{T}$  from a negative  $\varphi$  to  $+7.5^\circ$  and then the field was driven out (orange curve).

For this sample the half-width of the hysteresis in the AMR dependence measured at  $B = 15\text{T}$ ,  $T = 1.4\text{K}$  was  $\varphi^*(15\text{T}) \approx 9^\circ$ . The jump at  $B^*$  is more pronounced for sample  $x = 0.115$ . Nonetheless, the steps at  $B^*$  were always obtained by following the described sequence: a high enough magnetic field must be applied and turned through  $\varphi = 0^\circ$  up to an angle  $\varphi_1$  within the region of  $\Delta\varphi$ , such that  $|\varphi_1| < \varphi^*$ . At this angle the step at  $B^*$  will be observed upon decreasing the field. In Fig. 8.8 (b) it is seen that the position of the step in the field down-sweep also depends on the field orientation. For a small  $\varphi_1$ , i.e. closer to  $\varphi = 0^\circ$ , the step at  $B^*$  shifts to lower fields at which the magnetoresistance relaxes back to the reversible behavior. If the field is driven out at an angle closer to  $\varphi^*(B, T)$ , the step is observed at higher fields. For example for a down-sweep at  $\varphi = 3^\circ$  the step appeared at  $B^* = 6.3\text{T}$ , while for a field sweep at  $\varphi = 18^\circ$  the step was

---

crystals. This is probably a reason of a relatively sharp magnetoresistance kink at the spin-flop transition at  $\mathbf{B} \parallel [100]$ . This sample should not be confused with the other  $x = 0.10$  sample presented in other partes of this thesis.

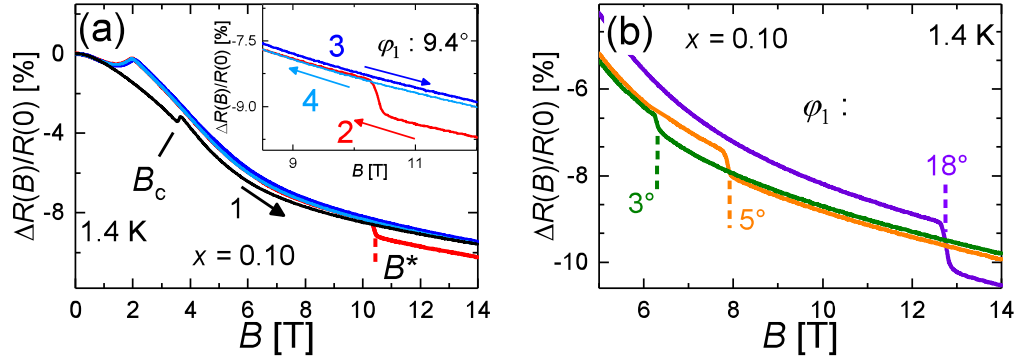


Figure 8.8: Consecutive magnetoresistance field sweeps performed on a  $x = 0.10$  sample at  $T = 1.4$  K, at different orientations near the  $[100]$  direction. (a) Curve 1 in the main panel is obtained at  $\varphi_0 = -0.6^\circ$  and the other curves at  $\varphi_1 = 9.4^\circ$ . The inset is a close-up of the FDMR in the high field regime, showing the jump at  $B^*$  and subsequent up and down field sweeps (curves 3 and 4). The colored arrows indicate the directions of the corresponding field sweeps, see text. (b) Magnetoresistance down-sweeps at different angles  $\varphi_1$ . Vertical dashed lines point to the respective positions  $B^*$  of the irreversible step-like feature. Before each down-sweep the field was increased from 0 T to 14 T at  $\varphi = 0^\circ$ .

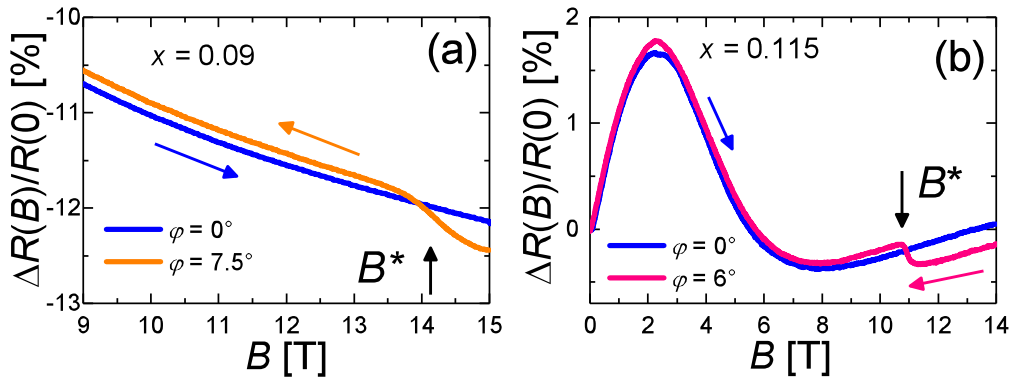


Figure 8.9: Irreversible high-field feature in the FDMR of the: a) (close-up)  $x = 0.09$ . Field up-sweep (blue line) at  $\varphi = 0^\circ$ . Field down-sweep (orange line) at  $\varphi = 7.5^\circ$ . b)  $x = 0.115$ . Field down-sweep (pink line) at  $\varphi = 6^\circ$ . See text for a description of the angle- and field-sweep sequence.

observed at  $B^* = 12.9, \text{T}$ <sup>5</sup>. Additionally, the height of the magnetoresistance step at  $B^*$  decreases with  $\varphi_1$  (compare the step heights between the green and purple curves in Fig. 8.8 (b)). This is consistent with the field dependence of the AMR hysteresis loop in Fig. 8.3, which becomes narrower and smaller in magnitude when lowering the field.

Further discussion and an explanation of the origin of the hysteresis and its related step-like feature will be provided in Chapter 9.

---

<sup>5</sup>For this sample the exact  $\varphi^*$  is not known. The down-sweeps were done at angles  $\varphi_1 \leq 23^\circ$ . For  $\varphi_1 = 23^\circ$  the step at  $B^* = 13.9 \text{T}$ .

## 8.2 Superconducting NCCO samples

With the study of the transport properties of the non-SC samples and after identifying the experimental characteristics of the step-like feature in the AMR and the accompanying hysteresis, the presence of this anomaly in the SC-samples was investigated. Due to the very high upper critical field along the layers, superconductivity in samples with  $x \geq 0.12$  could not be fully suppressed by the maximum field, 15 T, even at temperatures  $\sim 1 - 2$  K below the SC onset temperature  $T_{c,o}$ . Moreover, even a minor misalignment ( $< 1^\circ$ ) from the exactly in-plane field orientation had a strong effect on the mixed-state resistivity. Therefore in this part the main focus is on temperatures above  $T_{c,o}$ . However, for comparison purposes a short overview of the FDMR and AMR below  $T_{c,o}$  will be given. In Section 8.3 additional data will be shown to make a short comparison between the two  $x = 0.12$  measured during this work;  $x = 0.12(a)$  and (b). Here, the results discussed for  $x = 0.12$  refer to sample (a), unless specifically stated.

Figure 8.10 shows the low-temperature FDMR of the  $x = 0.13$  and  $x = 0.12$  samples, for a magnetic field applied parallel to the  $\text{CuO}_2$  layers, in the [100] and [110] directions. The inset in Fig. 8.10 (a) allows to observe that at very low fields the FDMR for the two directions behaves almost identically, but above  $\sim 1.5$  T the FDMR for  $B \parallel [100]$  increases more strongly than at [110]. In fact, unlike in the non-SC samples, the overall FDMR for the SC samples increases significantly with field. Given that these samples are in the SC state, an increase in resistance

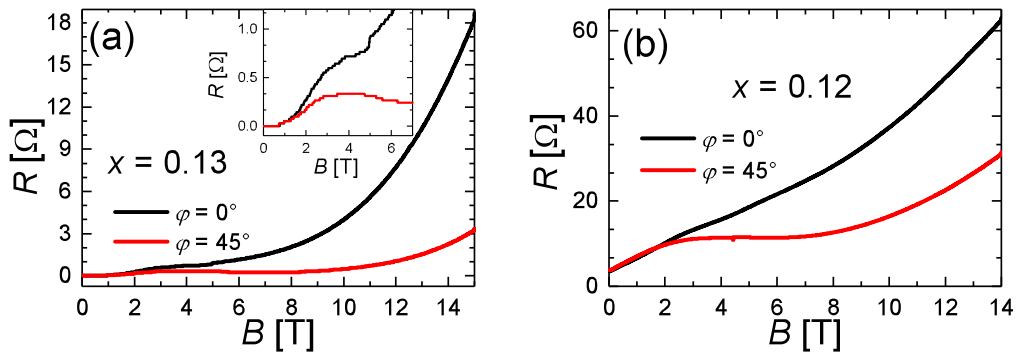


Figure 8.10: FDMR of underdoped SC NCCO samples at  $T = 1.4$  K: a)  $x = 0.13$  sample. The inset shows a close-up of the FDMR at low fields; (b)  $x = 0.12$  sample.

under magnetic field is expected. At 15 T the FDMR for the [100] direction is six times bigger than for the [110] direction. For sample  $x = 0.12$ , the FDMR increases with a steep slope at low fields and at  $\sim 2$  T the slope changes for the [110] direction. The FDMR at  $\mathbf{B} \parallel [100]$  increases monotonically but for the [110] direction, it flattens slightly and then changes slope again and increases until  $B = 14$  T. For both samples, between 2 T and 6 T a small shoulder is observed in the FDMR, which is more pronounced in the  $x = 0.12$  sample. The other SC samples showed very similar behavior. No evidence of spin reorientation at  $B_c$  was observed.

The AMR was measured at different magnetic fields  $B = 2 - 14$  T. For simplicity only few curves are shown in Fig. 8.11. The AMR of samples of  $x = 0.12$  and  $x = 0.125$  showed almost identical behaviors. Similarly to the non-SC samples, the FDMR oscillates with a  $90^\circ$  periodicity. It is important to mention that  $B_{c,2\perp} \ll B_{c,2\parallel}$ , and so a sample misalignment in the c-axis would cause a  $\varphi$ -dependence with a  $180^\circ$  periodicity; however, the observed  $90^\circ$  periodicity cannot be explained by sample misalignment. Additionally, in this case the anisotropy is opposite to the non-SC samples with maximum at  $\mathbf{B} \parallel [100]$  and minimum at  $\mathbf{B} \parallel [110]$  and hence consistent with the FDMR shown in Fig. 8.10. The AMR for

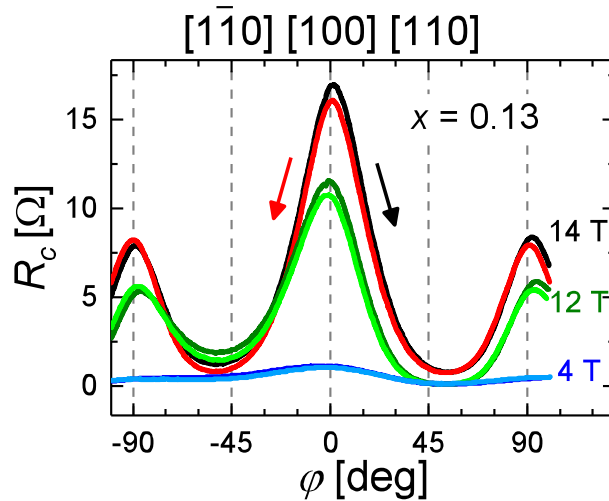


Figure 8.11: AMR of SC NCCO  $x = 0.13$  sample  $T = 1.4$  K for different magnetic fields rotated in the plane of the  $\text{CuO}_2$  layers. The black and red arrows indicate the angular sweep directions for the curves of the respective color.

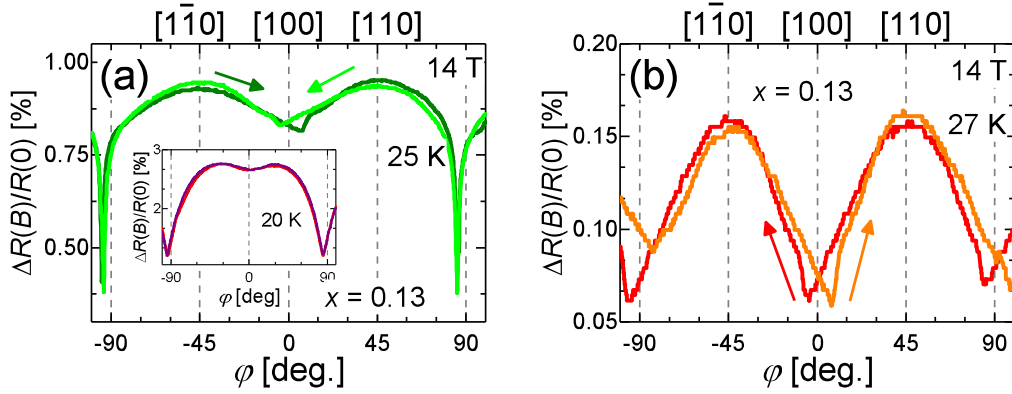


Figure 8.12: AMR of the SC NCCO  $x = 0.13$  sample at  $T > T_{c,o}$  for  $B = 14$  T. (a) AMR at  $25$  K. The inset shows the AMR of the same sample at  $T = 20$  K. The arrows indicate the direction of the rotation. (b) AMR at  $27$  K.

sample  $x = 0.13$  shows some asymmetric behavior: at  $\varphi = 0^\circ$  the resistance is two times bigger than at the two other equivalent positions,  $\varphi = \pm 90^\circ$ . This is due to the sample misalignment discussed in Section 7.2. Obviously, since the field  $B = 14$  T applied parallel to the  $\text{CuO}_2$  layers is insufficient to suppress superconductivity, the magnetoresistance is determined by the conducting properties of the SC mixed state while the normal state's properties don't play a significant role. Therefore, no evidence of hysteresis and its associated step-like feature were observed at this temperature.

Figure 8.12 (a) and (b) shows the  $14$  T AMR of the  $x = 0.13$  sample at different temperatures, right below and above  $T_c$ <sup>6</sup>. With increasing temperatures towards  $T_{c,o}$ ,  $4.2$  K  $< T < 25$  K, additionally to the considerable decrease of the AMR amplitude, the  $90^\circ$  periodicity was lost in the mixed state, see the inset in Fig. 8.12 (a). Here, the AMR has two sharp dips at  $\varphi = \pm 90^\circ$  and a shallow local minimum at  $\varphi = 0^\circ$ . At  $25$  K, in the main panel of Fig. 8.12 (a), the step-like feature begins to develop around  $\varphi = 0^\circ$ , although at the equivalent positions  $\varphi = \pm 90^\circ$  a strong dip in the resistance is observed. This strong asymmetric character of the AMR is attributed to sample misalignment in the c-axis of the sample. During rotation the field orientation at  $\varphi = 0^\circ$  is not exactly in the plane and the AMR has contributions of the out-of-plane components.

<sup>6</sup>The SC onset temperature observed in the  $R_c(T)$  was  $25$  K

At temperatures above  $T_{c,o}$ , the behavior of the SC samples is very similar to that presented for the non-SC samples. The AMR of the  $x = 0.13$  sample at 27 K is shown in Fig. 8.12 (b). The AMR recovers the  $90^\circ$  periodicity and its anisotropy is inverted with a maximum at  $\mathbf{B} \parallel [110]$  and minimum close to  $\mathbf{B} \parallel [100]$ . Similar to non-SC samples, the hysteresis and accompanying step-like feature are clearly observed. The hysteresis width  $\Delta\varphi$  has a similar field dependence as that shown in Fig. 8.4 for the  $x = 0.09$  sample and increases with magnetic field. All the SC samples exhibit a well discernible AMR and the step-like feature close to the  $[100]/[010]$  direction at  $T > T_{c,o}$ . The inversion of the anisotropy observed in this sample with respect to  $T_{c,o}$ , from an AMR at  $T < T_{c,o}$  with maximum at  $\mathbf{B} \parallel [100]$  to an AMR at  $T > T_{c,o}$  with maximum at  $\mathbf{B} \parallel [110]$  was only observed for the SC samples.

Similar as for the field sweeps shown in Figs. 8.8 and 8.9 for the  $x = 0.09$  sample, which describe the memory effect derived from the hysteresis in the AMR, the same measuring sequence was applied to the SC samples and the step at  $B^*$  was observed. The step had the same angular and field dependence observed in the non-SC samples.

Finally, Fig. 8.13 shows the temperature dependence of the hysteresis  $\Delta\varphi$  for the SC-samples for  $B = 14$  T. The hysteresis and the step-like feature were detected as long as the experimental resolution allowed for a reliable measurement of the AMR. However, due to the smaller overall AMR magnitude, the maximum temperature was lower than for the non-SC samples. Within the available temperature range the behavior is again similar to that of the non-SC samples described in Fig. 8.7. For the SC-samples the step-like feature is only observed at  $T < T_{c,o}$ . From this temperature forward  $\simeq 20$  K, increases and exhibits the highest values around 40 – 45 K, which is slightly lower than for the non-SC samples..

### 8.3 Effect of annealing on the AMR of two $x = 0.12$ samples

Two  $x = 0.12$  samples, with different annealing times were measured. Sample  $x = 0.12$  (a) was annealed for 60 hours and sample (b) for 40 hours. Here, a short presentation of the observed differences between the field- and angle-dependent magnetoresistance of the two samples is made.

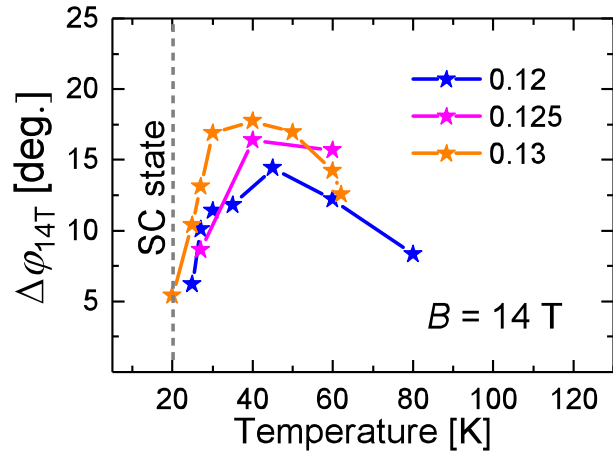


Figure 8.13: Temperature dependence of the hysteresis width in the AMR of the SC samples at  $B = 14$  T.

The FDMR of both  $x = 0.12$  samples was very similar. Figure 8.10(b) in the last Section showed the FDMR of sample  $x = 0.12$  (a), and this is representative for both samples. The shoulder-like behavior between 2 T and 6 T for a  $\mathbf{B} \parallel [110]$  was more pronounced for sample (b), slightly resembling the behavior of sample  $x = 0.115$  seen in Fig. 8.2.

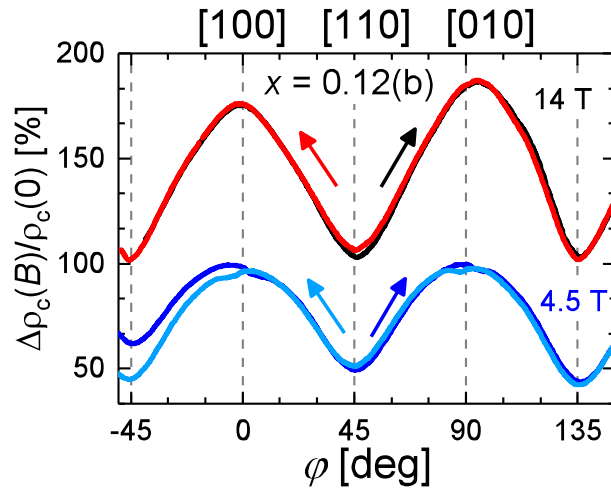


Figure 8.14: AMR of SC NCCO  $x = 0.12(b)$  sample  $T = 1.4$  K for different magnetic fields rotated in the plane of the  $\text{CuO}_2$  layers. The colored arrows indicate the angular sweep directions for the curves of the respective color.

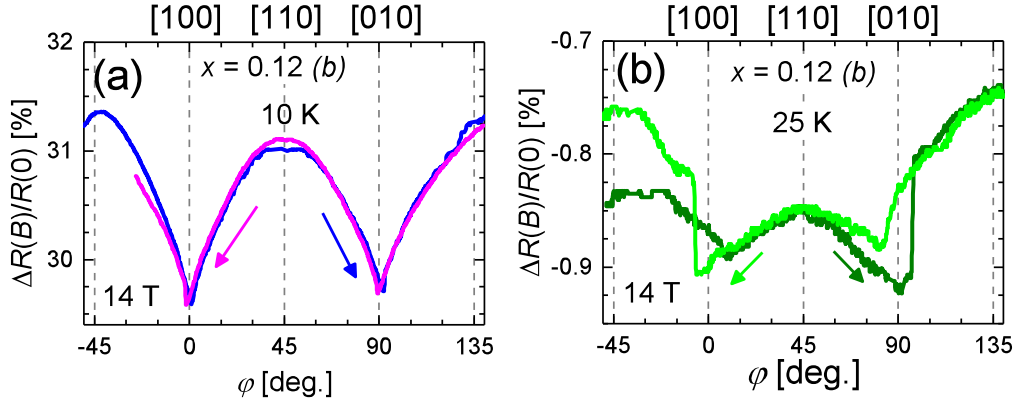


Figure 8.15: AMR of the NCCO  $x = 0.12$ (b) sample at different temperatures  $T > 1.4$  K for  $B = 14$  T. (a)  $T = 10$  K. The arrows indicate the direction of the rotation. (b)  $T = 25$  K.

The AMR of sample  $x = 0.12$ (b) at  $T = 1.4$  K is shown in Fig. 8.14. Interestingly, only for the two  $x = 0.12$  samples, at fields between 4 – 4.5 T and in the SC state, a small bend in the AMR was observed when the field was rotated through the [100]/[010] directions, see Fig. 8.14, (blue curves). However, this feature did not follow the same field dependence of the hysteresis observed in the other non-SC or SC samples. At fields  $B > 4.5$  T this bend was not observed. Thus, the small feature of the AMR for  $x = 0.12$  at 4 – 4.5 T cannot be related to the high-field hysteretic anomaly. In the non-SC samples, a dip around the [100] direction is observed at low fields and this is associated with the transformation from non-collinear to collinear states. However, above  $B_c = 4$  T this dip closes. The bend observed in the two  $x = 0.12$  samples could originate from the above-mentioned spin reorientation of the underlying AF system. However, it is not clear as to why this first feature should appear at  $B > 4$  T but then no sign of the high-field step-like feature is observed. It is possible that oxygen defects create pinning centers in the [100] direction which affect the transport in the mixed state. This could be tested by annealing samples with the same doping for longer times and testing if the feature at  $B = 4 - 4.5$  T disappears.

Figure 8.15 shows the AMR of sample  $x = 0.12$ (b) at higher temperatures. Only for this SC sample, the hysteretic step-like feature was detected already at 7 K. As already commented on in the beginning of this chapter, the  $R(T)$  for this sample did not show a full SC transition down to the lowest temperatures, therefore with

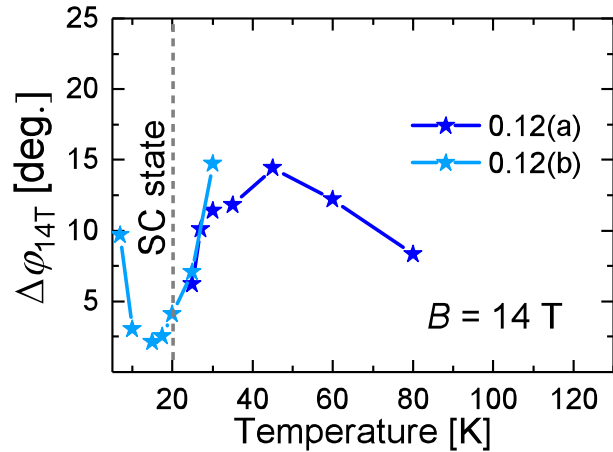


Figure 8.16: Temperature dependence of the hysteresis width in the AMR of the two  $x = 0.12$  SC samples at  $B = 14$  T. The AMR of sample  $x = 0.12(b)$  was not measured above 30 K.

increasing temperature the normal state is reached and the features of AF are visible. At 7 K the anisotropy of the AMR was already opposite and at 10 K the AMR looked very similar to that of the non-SC samples, as seen in Fig. 8.15 (a). With increasing temperature the hysteresis continued to shrink, as it did for the non-SC samples, but the temperature where it vanished was slightly lower,  $\sim 15$  K.

In Fig. 8.16 the temperature dependence of the hysteresis width for the two  $x = 0.12$  samples is shown. Sample  $x = 0.12(b)$  was the only SC sample for which the hysteresis  $\Delta\varphi$  was detected at  $T < T_{c,o}$ . Therefore, it is possible to observe that, similarly to the non-SC samples and starting from low temperature, the  $\Delta\varphi$  narrows with increasing temperature and has a minimum at  $\sim 15$  K. Above this temperature  $\Delta\varphi$  becomes wider again. The minimum  $\Delta\varphi$  for this sample is observed at slightly lower temperatures than for the non-SC samples.

The case of these two  $x = 0.12$  samples, resembles to some extent the data presented for the two  $x = 0.125$  samples presented in Part I. The  $x = 0.125$  fast-grown sample showed partial superconductivity and still the step-like feature was observed at the lowest temperatures. In this case, the  $x = 0.12(b)$  sample, which was annealed for a shorter time, did not show evidence of the step-like feature at 1.4 K despite not being fully SC. For this sample, only when temperature was increased to 7 K, were the features of antiferromagnetism visible. The anisotropy

of the AMR in the  $x = 0.125$  fast-grown sample in the SC state was the same as for other SC samples, yet the step-like feature was visible. For the  $x = 0.12$ (b) sample, the anisotropy of the AMR was inverted below  $T_{c,o}$ .

Unfortunately, the fast-grown  $x = 0.125$  sample, was not measured between  $T = 1.4$  K and  $T = 20$  K and it is not possible to make a direct comparison of the behavior in the hysteresis width of the AMR.

Considering the cases between the  $x = 0.125$  and  $x = 0.12$  samples, it seems that the apparent coexistence of the SC and antiferromagnetic states is different in both sets of samples. Although the case of the  $x = 0.125$  samples is further discussed in Part I, a short comparison can be made between these samples.

The difference between samples  $x = 0.12$  (a) and (b) is the annealing times. In the next Section, it will be discussed that the step-like feature is a sign of AF order. Since the signs of antiferromagnetism in sample  $x = 0.12$  (b) appear below  $T_{c,o}$  but not at the lowest temperature (including the inversion of anisotropy in the AMR), it can be concluded that the applied magnetic field suppresses the remaining superconductivity in the sample and so it is brought to the normal state. Superconductivity in this sample is weaker, due to the shorter annealing treatment. However, the AMR of sample  $x = 0.12$  (a) behaves like that of a fully SC sample. It is already known that the duration of the annealing process influences the volume of SC fraction [54]. But, additionally from the results presented here, it can be implied that because of the shorter annealing process there is an inhomogeneous coexistence of the AF and SC states and, as SC is suppressed by a magnetic field, the underlying antiferromagnetism can be detected. On the other hand, for the  $x = 0.125$  fast-grown sample, the coexistence of AF and SC states, seems to be inherent to the crystal, meaning that it cannot be influenced by annealing.

To reach a certain conclusion in this respect, further measurements are needed, to compare the effect of annealing in the SC fractions and how it reflects in its transport properties.



## 9 Discussion

The data presented in the previous sections demonstrate the existence of a hysteretic anomaly in the high-field AMR for underdoped NCCO, both non- and SC samples in a wide temperature range. It is shown that the hysteresis  $\Delta\varphi$  has a nonmonotonic temperature dependence which is similar in all samples. Figures 8.7 and 8.13 show the temperature dependence of  $\Delta\varphi$  for all samples measured in this work. As already discussed in the previous two sections,  $\Delta\varphi$  is largest at  $T = 1.4$  K for all non-SC samples. With increasing temperature,  $\Delta\varphi$  becomes more narrow and seems to vanish near  $\sim 20$  K. Above this temperature, the step-like feature reappears for the non-SC samples and is firstly observed above the superconducting transition in the SC samples.  $\Delta\varphi$  has a flat maximum  $\sim 40 - 45$  K. Above  $\sim 70 - 80$  K  $\Delta\varphi$  does not change much until it is not detected anymore due to the reduction of the overall AMR.

In an earlier study of the out-of-plane AMR of a strongly underdoped NCCO with  $x = 0.025$  [96], it was detected that the fourfold symmetry was lost at  $T = 30$  K and 70 K. Another study on the same  $x$  revealed a particular temperature dependence of  $B_c[110]$  around 30 K [91]. These sharp changes were attributed to the successive transitions between AF phases I, II, and III, characterized by different mutual orientations of  $\text{Cu}^{2+}$  and  $\text{Nd}^{3+}$  [87, 89–91, 96]. The experiments presented in this work on stronger doped samples,  $x \geq 0.09$ , did not show such sharp changes of the overall out-of-plane AMR. However, the nonmonotonic  $\Delta\varphi(T)$  dependence in Figs. 8.7 and 8.13 can be divided in three distinct temperature regions separated by the hatched boxes in the Figures. By analogy with the stronger underdoped crystals, these three areas with similar behavior in  $\Delta\varphi$  can be associated with the spin phases III, II and I of the parent compound NCO, respectively. This would imply that, in contrast to the parent compound and very underdoped NCCO, which have a transition between the phases III and II at  $T_{N,2} \approx 30$  K, the samples in this work have a lower critical

temperature  $\simeq 20$  K for this transition. This difference can be attributed to the increase in dopant concentration  $x$ . The samples in this work are very close to the SC doping range and thus, significant changes in the electronic and magnetic properties in comparison to strongly underdoped crystals can be expected.

As can be noticed from Fig. 8.5 and 8.6 the total amplitude of the AMR continuously decreases with increasing temperature. Thus, the step-like feature could only be detected as long as the AMR was within the resolution of the experiment. The maximum temperature at which the step-like feature was reliably detected for all samples is shown in Fig. 9.1. From this Figure an  $x$  dependence could be assumed, as it seems that the maximum temperature where the step-like feature is observed decreases with increasing dopant concentration. In fact, in similar transport studies of hole-doped cuprate superconductors, a relation has been suggested between the temperature where the AMR appears and the temperature where AF order is established [102, 108]. In particular, in a study of  $\text{La}_{2-x}\text{Sr}_x\text{CuO}_4$  films [102], the twofold AMR disappears at a temperature  $T_D$  and for a sample with  $x = 0.15$  the AMR is not observed above  $T_{c,o}$ . It was suggested that the AMR originates from the AF order or from a spin-density-wave (SDW) transition. However, as mentioned in Section 6.1.2, there are other mechanisms which can lead to the observation of a two- or fourfold AMR, and in general, the magnetoresistance is not a direct probe of the magnetic properties of the system.

The hysteretic behaviour of the AMR and the accompanying step-like feature can hardly be explained within a nonmagnetic or an ordinary paramagnetic scenario. Therefore, this behavior can be considered as an evidence of the AF phase in the samples of this work with increasing dopant concentration up to the superconducting regime of the phase diagram, with  $x = 0.13$ . The high-field hysteretic anomaly occurs entirely in the collinear state and must be caused by some discontinuous change of the spin structure within this state. As mentioned in section 6.1.1, the step-like feature has been attributed to a rearrangement of the antiferromagnetically ordered  $\text{Nd}^{3+}$  spins [11]. However, the magnetic moment of  $\text{Nd}^{3+}$  increases considerably below 5 K [88], the Néel temperature of the  $\text{Nd}^{3+}$  subsystem has been determined by low temperature specific heat measurements at  $T_N = 1.7$  K, for the undoped parent compound, and at even lower temperatures for the doped NCCO [88, 109]. Although the copper ions exercise an effective magnetic field on the  $\text{Nd}^{3+}$  ions by a Cu-Nd exchange interaction [87], the  $\text{Nd}^{3+}$

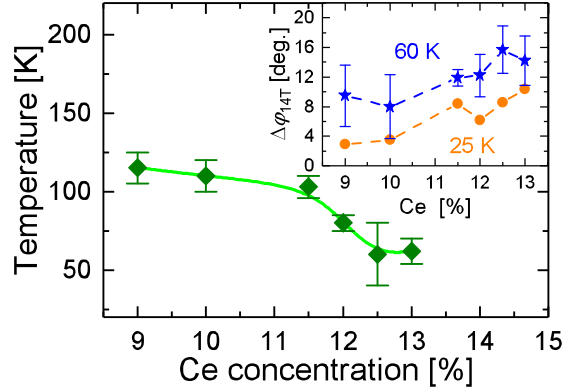


Figure 9.1: Maximum temperature at which the hysteresis  $\Delta\varphi$  was resolved for all underdoped NCCO samples. The error bar corresponds to the step size in temperature where the next measurement was conducted. The inset depicts The width of the hysteresis in the 14 T AMR patterns obtained at  $T = 25$  and 60 K for different SC and non-SC samples, plotted against the nominal doping level  $x$  (sample  $x = 0.12(b)$  is not shown).

ions are not in an ordered structure at the temperatures where the discussed behavior is observed,  $T \leq 5$  K, and thus above  $T_{N,Nd}$  no sign of this feature should be possible. The data presented in this work, clearly demonstrates the presence of the hysteretic anomaly in the AMR at temperatures up to  $\sim 100$  K  $\gg T_{N,Nd}$ . Therefore, its origin should rather be associated with the  $\text{Cu}^{2+}$  spins, which remain ordered at these temperatures, as at least known for lower dopant concentrations.

In the inset of Fig.9.1 the hysteresis width  $\Delta\varphi$  obtained for different  $x$  at  $T = 25$  K and 60 K is shown for comparison. At both temperatures  $\Delta\varphi$  shows an increase with dopant concentration, although there is a significant scattering. At the higher temperature, since the amplitude of the AMR decreases, the feature is also weakened; this is the source of the relatively large error bar. Additionally, a certain dependence of the hysteresis on the sample quality should also be taken into account. Nevertheless a general trend of increasing  $\Delta\varphi$  is observed.

More importantly, since this feature is attributed to the high-field reorientation of the  $\text{Cu}^{2+}$  spins within the collinear AF state, it can be considered as an unequivocal fingerprint of long-range AF order.

Beyond attributing the origin of the feature to a particular spin system, dis-

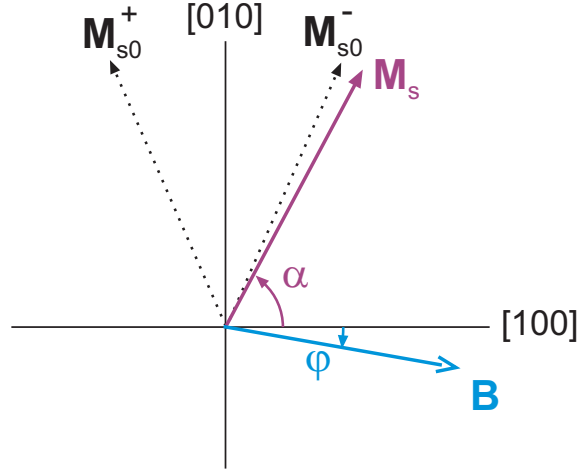


Figure 9.2: Schematic diagram of the equilibrium orientation of the  $\text{Cu}^{2+}$  staggered moment  $M_s$  in the field  $B = 14 \text{ T}$  applied at angle  $\varphi_1 = -10^\circ$  from the  $[100]$  direction, obtained from Eq. (9.1). Dotted arrows show the two equilibrium directions of  $M_s$  for  $B \parallel [100]$ .

cussing how this hysteretic anomaly develops is important. Although the transport measurements shown in this work do not give direct information on the real spin orientations, a model of the possible field-induced effect on the antiferromagnetically ordered  $\text{Cu}^{2+}$  spin system can be proposed.

Some information about the magnetic structure of the electron-doped cuprate superconductors should be kept in mind to devise such a model. The field-induced transformation between the noncollinear and collinear structures is of first order for a field applied in the  $[100]$  direction and of second order for the  $[110]$  direction [93–95]. The staggered magnetization can only be exactly perpendicular to the  $[100]$  direction at a field  $B \rightarrow \infty$ . Additionally, for fields applied at intermediate orientations between  $[100]$  and  $[110]$  the staggered magnetization firstly orients along  $[110]$  through a second order transition and, as the field increases, the spins rotate further to orient themselves more perpendicular to the field direction [95].

The equilibrium direction of the  $\text{Cu}^{2+}$  staggered moment  $M_s$  in the high-field collinear state is mainly determined by the balance of the contributions of the pseudodipolar and Zeeman terms to the energy, which can be expressed as [94, 95]:

$$E \approx E_0 [\pm G \sin 2\alpha - 2K^2 \sin^2(\varphi - \alpha)] , \quad (9.1)$$

---

where  $E_0$  is determined by the in-plane exchange interaction,  $G = (\Omega_{\text{opt}}/\Delta_0)^2$  with  $\Delta_0$  being the in-plane spin-wave gap and  $\Omega_{\text{opt}}$  the splitting of the in-plane spin-wave spectrum caused by the interplane pseudodipolar interaction, and  $K = g\mu_{\text{B}}B/\Delta_0$  characterizes the Zeeman splitting. The angles  $\varphi$ <sup>1</sup> and  $\alpha$  give the directions of the field  $\mathbf{B}$  and staggered moment  $\mathbf{M}_s$ , respectively, and are defined in Fig. 9.2. The sign “ $\pm$ ” in front of the first term in Eq. (9.1) takes into account the tetragonal symmetry of the system. The equilibrium direction of  $\mathbf{M}_s$  is determined by minimising  $E$  with respect to  $\alpha$ . An important result is that for  $\varphi = 0^\circ$  there are two equilibrium directions,  $\mathbf{M}_{s,0}^+$  and  $\mathbf{M}_{s,0}^-$ . Evidently, the other two solutions with the staggered magnetization vectors turned by  $180^\circ$  are physically the same.

Considering the FDMR results from the non-SC samples, including the  $x = 0.05$  sample, the critical fields  $B_c$  for the transition between the noncollinear and collinear states at  $\mathbf{B} \parallel [100]$  and  $\mathbf{B} \parallel [110]$  give the typical values  $B_{c,\text{max}} = 4 \text{ T}$  and  $B_{c,\text{min}} = 1 \text{ T}$ , respectively. The coefficients in Eq. (9.1) [94]:  $K = B/B_{c,\text{min}}$  and  $G \approx (B_{c,\text{max}}/B_{c,\text{min}})^4$  can thus be calculated and the dependence of the energy on the angle  $\alpha$  can be rewritten as:

$$E \propto [\pm \sin 2\alpha - 0.0078 \text{ T}^{-2} \cdot B^2 \sin^2(\varphi - \alpha)]. \quad (9.2)$$

Due to the different signs on the first term in Eq. (9.2), two branches of the energy dependence on the direction of the staggered moment are obtained. To illustrate this, Fig. 9.3 shows the case for a field of  $B = 14 \text{ T}$  directed at  $\varphi = 0^\circ$  and  $10^\circ$ . The dotted lines in Fig. 9.3 illustrate that, for a field at  $\varphi = 0^\circ$ , the energy exhibits two equal minima at  $\alpha_0^- = 63.7^\circ$  and  $\alpha_0^+ = 116.3^\circ$ , respectively. Hence, if the field is applied exactly parallel to  $[100]$  and increased from zero to  $14 \text{ T}$  the resulting collinear state is expected to have two domains with two different  $\mathbf{M}_s$  as shown by the dotted arrows in Fig. 9.2. However, this degeneracy only applies for a field applied in the  $[100]$  direction. For example, in a similar scenario but for a field applied at angle  $\varphi_1 = -10^\circ$  the energy in Eq. (9.2) exhibits only one global minimum, at  $\alpha_1 = 59.8^\circ$ , see Fig. 9.3. Consequently, if the field is ramped up from zero at a constant  $\varphi$ , only one direction of  $\mathbf{M}_s$  should be realized in the collinear state. This  $\mathbf{M}_s$ , represented by the lilac arrow in Fig. 9.2, is smoothly dependent on the field strength. At the critical field  $B_c(\varphi)$  the spins will align almost parallel

---

<sup>1</sup>The angle  $\varphi$  is defined in the interval  $(-\frac{\pi}{2}, \frac{\pi}{2})$

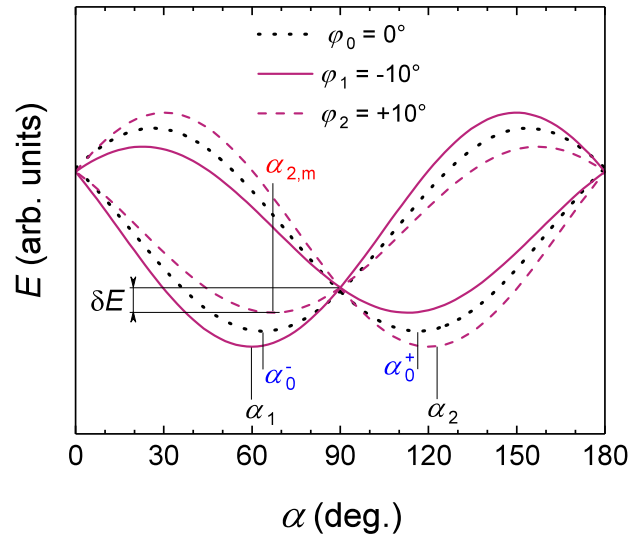


Figure 9.3: Dependence of magnetic energy on the orientation of the  $\text{Cu}^{2+}$  spins calculated from Eq. (9.2) for  $B = 14$  T, aligned parallel to the  $[100]$  axis or at an angle of  $\pm 10^\circ$  from this direction.  $\alpha$  is the angle between the staggered magnetization vector  $\mathbf{M}_s$  and  $[100]$ . At  $\varphi = 0^\circ$  the state is doubly degenerate with the equilibrium angles  $\alpha_0^\pm = 90^\circ \pm 26.3^\circ$ . In the tilted field there is only one stable state with  $\alpha_1$  and  $\alpha_2$  for  $\varphi_1$  and  $\varphi_2$ , respectively.  $\delta E$  is the energy barrier between the metastable state at  $\alpha_{2,m}$  and the stable state at  $\alpha_2$ .

---

to [110] and then asymptotically approach the direction perpendicular to the field at  $B \rightarrow \infty$  [95].

During field rotations, further considerations should be made. In the high-field regime, regardless of the field orientation; the spins are ordered in a collinear structure. Consider, for example, that the sample is turned at a high field from  $\varphi_1 = -10^\circ$  to  $\varphi_2 = 10^\circ$ , passing through the direction  $\mathbf{B} \parallel [100]$ . For a field direction at  $\varphi_1 = -10^\circ$  the global minimum of the energy is at  $\alpha_1$  and for  $\varphi_1 = +10^\circ$  at  $\alpha_2$ . With a continuous rotation from the negative side towards  $0^\circ$ , the energy minimum approaches  $\alpha_0^-$ , see Fig. 9.3. When  $\varphi$  crosses zero to the positive side, there is a discontinuous jump of the energy minimum. The global minimum must change from  $\alpha < \alpha_0^-$  to  $\alpha > \alpha_0^+$ . With further rotation this minimum further shifts towards  $\alpha_2$  as  $\varphi$  reaches  $\varphi_2$ . However, the other branch of Eq. (9.2) still has a local minimum at angle  $\alpha_{2,m} < 90^\circ$ . Before the spins can "fall" to the minimum at  $\alpha_2$ , the energy barrier  $\delta E$  between the two minima,  $\alpha_{2,m}$  and  $\alpha_2$  (Fig. 9.3), must be overcome. If  $\delta E$  is high enough, most of the spins will remain in the metastable state with  $\alpha_{2,m}$ . But as the field is further tilted away from [100], the barrier becomes smaller and at a critical angle  $\varphi^*$  the spins relax to the equilibrium orientation at  $\alpha > 90^\circ$ . Evidently, this scenario also applies for a rotation in the opposite direction.

The above-presented field-induced spin reorientation should result in a clear effect in the magnetoresistance, due to strong spin-charge coupling in the system. The hysteretic jump in the AMR at a critical angle  $\varphi^*$ , is fully consistent with the described scenario. Thus, this model explains, at least qualitatively, the existence of the hysteresis in the angular sweeps.

However, the observed dependence of the  $\Delta\varphi$  on the field strength cannot fully be explained with this model and remains an open question. Consider Fig. 9.4. According to Eq. (9.2), as the field increases, for example from 8 T to 14 T, the energy minimum shifts closer to  $90^\circ$  and the energy barrier between the metastable and stable states is also reduced. This would imply that the hysteresis width  $\Delta\varphi$  should reduce with increasing field since the energy barrier becomes smaller and smaller. This obviously contradicts the data in Fig. 8.4, which shows a clear increase of  $\Delta\varphi$ , as the field increases. Therefore, the theory should be further developed to explain how the angular range where the metastable  $\mathbf{M}_s$  orientation

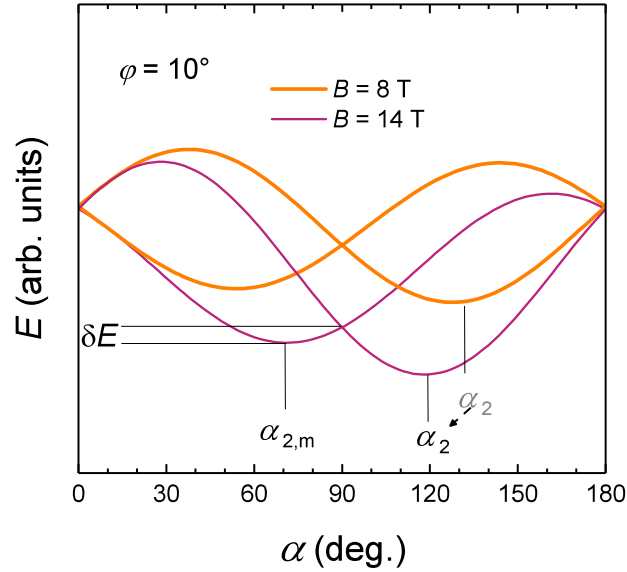


Figure 9.4: Dependence of magnetic energy on the orientation of the  $\text{Cu}^{2+}$  spins calculated from Eq. (9.2) for two different fields aligned at an angle of  $10^\circ$ . In the tilted field there is only one stable state with  $\alpha_2$ .  $\delta E$  is the energy barrier between the metastable state at  $\alpha_{2,m}$  and the stable state at  $\alpha_2$ .

can persist can be expanded by increasing the magnetic field.

So far, only the  $\text{Cu}^{2+}$  spin system has been considered. However, the  $\text{Nd}^{3+}$  spins appear to be indirectly involved in the observed phenomena. During the studies of the low-temperature angle-dependent magnetization, which is strongly dominated by  $\text{Nd}^{3+}$ , an anomaly was detected for fields slightly tilted from the  $[100]$  axis [11, 110]. Due to the exchange interaction between Cu-Nd, the orientation of the paramagnetic  $\text{Nd}^{3+}$  spins is sensitive to the changes described above. This may be a reason for an enhancement of the hysteretic feature at low temperatures, at which the magnetic susceptibility of  $\text{Nd}^{3+}$  rapidly grows [11].

In summary, the behavior of the step-like feature can be understood with the model above-described as a field-induced reorientation of  $\text{Cu}^{2+}$  spins within the collinear antiferromagnetic state and, therefore, can be considered as a signature of long-range AF order. Thus, the presence of the hysteresis in the AMR for the SC samples implies that superconductivity and steady AF order coexist at least in the narrow interval  $0.12 \leq x \leq 0.13$  on the border of the SC doping range. Interestingly, a weak hysteretic anomaly has also been detected in the interlayer

---

magnetoresistance of a SC sample with  $x = 0.13$  for an out-of-plane rotation in a  $B = 28$  T magnetic field [44]. While the exact reason for the latter anomaly needs a separate investigation, it is most likely related to the AF ordered magnetic system. Considering the results presented in Part I of this work, it is possible that a slight inhomogeneity of cerium distribution or oxygen defects are the reasons for the existence of two phases in a crystal. However, the behavior of  $\Delta\varphi$  shown in the inset of Fig. 9.1, despite the scattering, hint towards a systematic  $x$ -dependence of the hysteresis. If this is indeed the case, it would mean that the hysteresis and hence the AF state are intrinsic to each of the doping levels presented in this work. For clarifying the situation, more thorough magnetization and spectroscopic studies of high-quality SC crystals on the lower edge of the SC doping region would be very interesting.



# 10 Addendum: As-grown NCCO

In Part I it was mentioned that the electron-doped cuprate superconductors are non-superconducting in their as-grown state and therefore the crystals must be annealed. The effects of the annealing treatment were observed in the experimental results discussed in Part I of this work. Since the effect of the annealing process is still not well understood, an investigation of the transport properties of an as-grown NCCO crystal can provide information with respect to the magnetic properties of a doped crystal before annealing. In particular, by studying the behavior of the step-like feature in a doped but non-SC sample and comparing it with the samples discussed in the last sections.

As it has been proved in section 8.2, a superconducting NCCO crystal with  $x = 0.13$  shows evidence of long-range AF order in the AMR at temperatures above  $T_{c,o}$ . Therefore, if the FDMR and AMR of an as-grown  $x = 0.13$  sample are measured, a direct comparison of the magnetotransport properties at this dopant concentration between the non-SC and SC states can be made. For the measurements, a  $x = 0.13$  as-grown (ag) sample,  $0.4 \times 0.4 \times 1$  mm, from the same batch as that presented in Section 8.2 was selected. Sample contacts and further experimental parameters were maintained the same as discussed in chapter 7. The temperature range used for these measurements was 1.4 K – 30 K.

## 10.1 Results

Figure 10.1 shows the normalised zero-field temperature dependence of the resistance  $R$  of the  $x = 0.13$ (ag) sample. As expected, the sample is not superconducting, with a minimum  $R$  at 86 K. The temperature dependence of the resistance for the non-SC samples presented in section 8.1 was very similar, although for those samples the minimum was observed at lower temperatures.

In order to identify the low temperature characteristic field  $B_c$  for this sample,

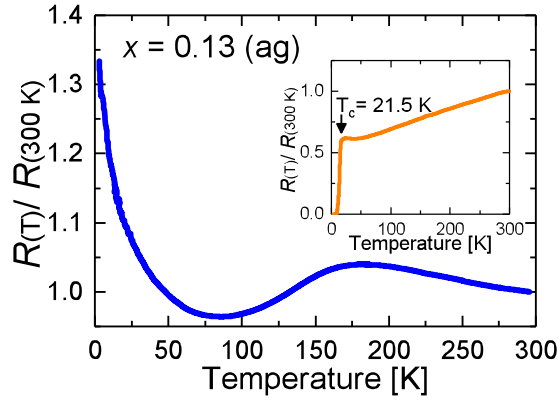


Figure 10.1: Normalised  $R(T)$  for NCCO  $x = 0.13$  as-grown sample. The resistance is normalised to the room temperature value  $R_c(300\text{ K})$ . For comparison, the inset shows the normalised  $R(T)$  curve for the annealed NCCO  $x = 0.13$  sample already discussed in section 8.2.

field sweeps with a magnetic field applied parallel to the  $[100]$  and  $[110]$  directions at  $1.4\text{ K}$  were performed. The FDMR of sample  $x = 0.13(\text{ag})$  is shown in Fig. 10.2. The magnetoresistance is defined the same as in Section 8<sup>1</sup>.

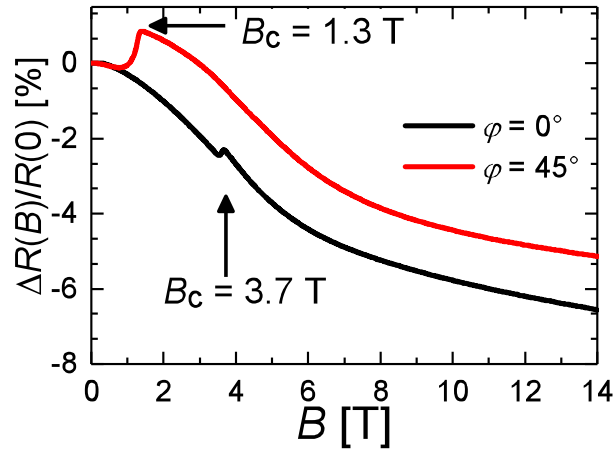


Figure 10.2: Field dependent magnetoresistance of the NCCO  $x = 0.13$  as-grown sample at  $T = 1.4\text{ K}$ .  $B_c$  is the critical field for the transformation between the noncollinear and collinear spin structures.

The magnetoresistance of the as-grown sample becomes more negative with increasing field, similarly to the FDMR of annealed non-SC samples with  $x =$

<sup>1</sup> $\Delta R(B)/R(0) \equiv [R(B) - R(B = 0)]/R(B = 0)$

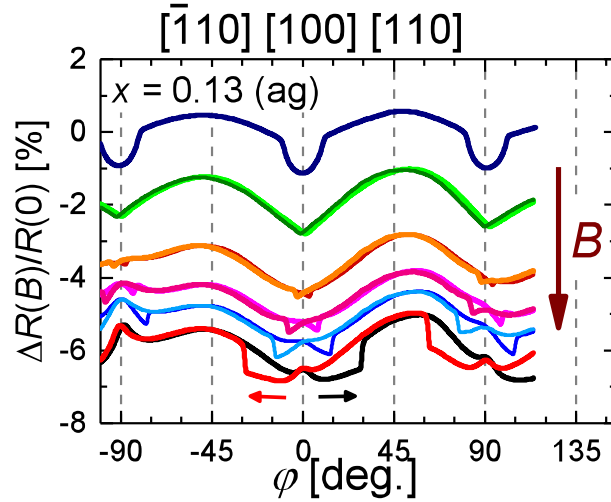


Figure 10.3: AMR of the NCCO  $x = 0.13$  as-grown sample at  $T = 1.4$  K for increasing magnetic fields oriented parallel to the  $\text{CuO}_2$  layers. The red and black arrows indicate the directions for the rotation of the field. The AMR was measured for the fields  $B = 2 - 14$  T (from top to bottom) with a step of 2 T. The AMR at  $B = 12$  T is not shown.

0.09 – 0.115 seen in Figs. 8.2. The FDMR for both presented directions follows a similar, almost parallel, behavior. At  $B = 14$  T the FDMR for the field applied in the  $[110]$  direction is only 1.5% higher than for the  $[100]$  direction. For a field applied in the  $[110]$  direction, there is a large kink at  $B_c = 1.3$  T, which corresponds to the second order transition to the collinear state. In comparison with the non-SC samples, this feature is observed at a slightly higher field. The kink itself is also twice as big as the one observed, for example, in the  $x = 0.09$  annealed sample at the same conditions, but almost ten times smaller than that of annealed sample with  $x = 0.05$ . Furthermore, it is very evident that the feature at  $B_c$  for  $\mathbf{B} \parallel [100]$  is a sharp magnetoresistance kink at 3.7 T. Such a prominent feature at  $B_c$  was only seen in strongly underdoped NCCO annealed samples, for example for  $x = 0.05$  shown in Fig. 6.4. However, for  $x \geq 0.09$  the spin-flop transition was hardly discernible in the  $R(B)$  dependence and only determined through examination of the field derivative of the resistance  $dR/dB$ .

The AMR of the  $x = 0.13(\text{ag})$  sample at 1.4 K measured at different fields is shown in Fig. 10.3. The AMR behaves very similar to the low temperature AMR of the annealed non-SC samples. As expected from the observed anisotropy of the

FDMR shown in Fig. 10.2, the AMR has a maximum at  $\varphi = 45^\circ$  and minimum at  $\varphi = 0^\circ$ . At  $B = 2$  T the collinear state is stable around the [110] but a dip around [100] is observed, indicating the angular range where the spins in adjacent  $\text{CuO}_2$  are noncollinear. At  $B = 4$  T, which is above the detected  $B_{c,\text{max}}$ , this dip has "closed" and the spins are stable in the collinear state for all field orientations.

At fields  $B \geq 6$  T the step-like feature is clearly observed in the AMR and the  $\Delta\varphi$  increases with magnetic field reproducing the observed behavior in the other non-SC samples. Above 10 T a peculiar change in the behavior around the [100] direction is observed. As the field approaches  $\varphi = 0^\circ$ , the magnetoresistance increases slightly and has a second maximum at  $B \parallel [100]$ . With continuing rotation the AMR decreases again, then it flattens until an angle  $\varphi^*$  where it suddenly increases. The hysteresis at 14 T for this sample,  $\Delta\varphi = 55^\circ$ , is wider than for any other non-SC sample presented in Section 8.1.

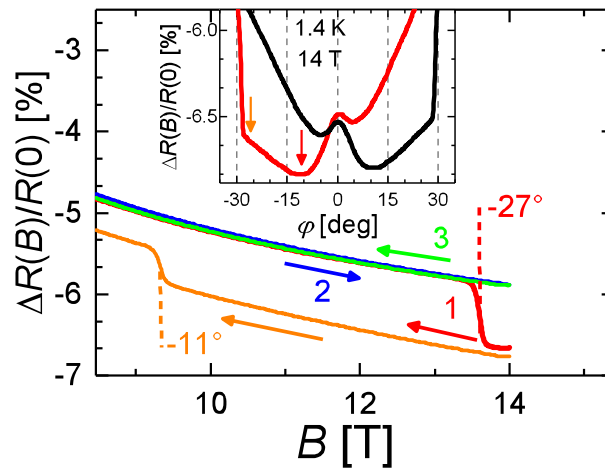


Figure 10.4: Consecutive magnetoresistance field sweeps of the NCCO  $x = 0.13(\text{ag})$  sample at  $T = 1.4$  K at two different orientations near the [100] direction. Curves 1 – 3 were recorded at  $\varphi_1 = -27^\circ$ . Additionally a field sweep was done at  $\varphi_1 = -11^\circ$ . The inset shows a close-up of the 14 T AMR at the same temperature around  $\varphi = 0^\circ$  and the arrows indicate the angles at which the field sweeps were performed.

To further confirm that the observed hysteresis in this sample produced the same memory effect at a field  $B^*$  as the one measured in the other samples discussed in this work, the field sweep sequence described in section 8.1 was applied to this sample at  $T = 1.4$  K. The results are shown in Fig. 10.4. In a steady 14 T

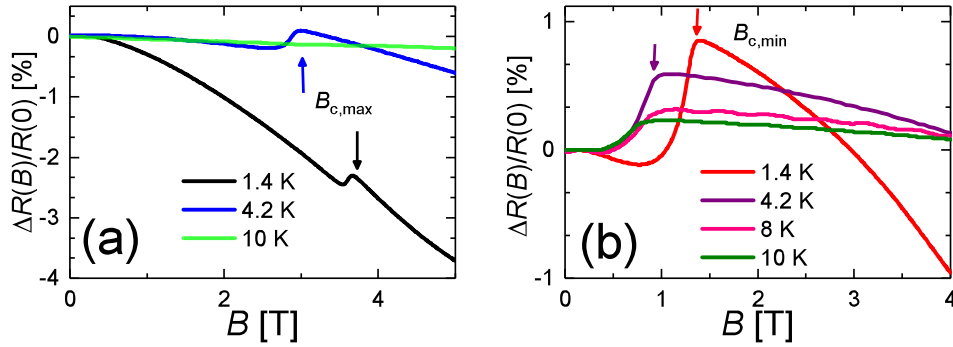


Figure 10.5: Close-up of the FDMR of the NCCO  $x = 0.13$  as-grown sample at different temperatures. (a) Close-up of the first order spin-flop transition feature at  $B_{c,max}$ . (b) Close-up of the second order transition feature at  $B_{c,min}$ .

magnetic field, the field was rotated from a high angle to  $\varphi_1 = -27^\circ$  and the field was decreased. At  $B^* = 13.7$  T a kink is observed in curve 1 in the main panel of Fig. 10.4. Below 13.4 T the FDMR behaved similarly to that presented in Fig 10.2. The field was then increased (curve 2) and decreased (curve 3) without any change in the orientation. As a result, a hysteresis in the FDMR is observed, as expected. Additionally, a down-sweep was performed at  $\varphi_1 = -11^\circ$  (orange line). In this case, the kink is observed at a lower field,  $B^* = 9.4$  T. These results confirm that, in as-grown samples, the hysteresis and its associated step-like feature have similar behavior in stronger underdoped but annealed samples.

Furthermore, the temperature dependence of the features corresponding to the transformation between the noncollinear and collinear states in the FDMR was investigated. Figures 10.5 (a) and (b) show a close-up of the FDMR at different temperatures for a field applied parallel to the [100] and [110] directions, respectively. For a field applied parallel to the [100] direction, the spin-flop feature is only visible in the FDMR at temperatures below 4.2 K. For temperatures between 4.2 K and 10 K the FDMR for this field orientation was not measured. At 10 K the FDMR is almost flat and no feature is detected even in the field derivative  $dR/dB$ . A simple comparison of the value of  $B_c$  at 1.4 K and 4.2 K in Fig. 10.6 (a) demonstrates that the spin-flop feature shifts to a lower field when temperature increases, from  $B_c = 3.7$  T to 2.9 T. In Fig. 10.6(b) the AMR at  $B = 2$  T at  $T = 4.2$  K and 8 K is shown. It is seen that, at this field strength, the dip around the [100] is narrower than at 1.4 K. This is another indication that the  $B_c$  has shifted to lower

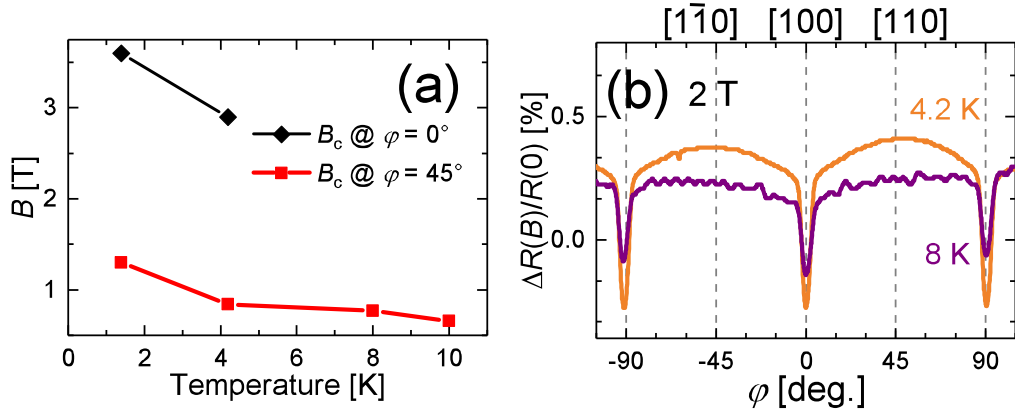


Figure 10.6: (a) Temperature dependence of the features at  $B_c$  for  $\varphi = 0^\circ$  and  $\varphi = 45^\circ$  for the NCCO  $x = 0.13$  as-grown sample. (b) AMR of the  $x = 0.13$  as-grown sample at two different temperatures at 2 T.

fields. In the case of the annealed non-SC samples, such decrease in  $B_c$  was not observed. However, it is not possible to determine the exact  $B_{c,\max}$  at 8 K (see Fig. 10.6(b)), since the FDMR at this direction was not measured. The AMR at 4 T (not shown) looked very similar to the one at 1.4 K, thus meaning that the  $B_{c,\max}$  had been surpassed. The width of the dip at 8 K seems very similar to the one at 4.2 K, it is possible that there is not a big change in the  $B_c$  in this temperature interval.

The second order transition for  $\mathbf{B} \parallel [110]$  also shifts to lower fields with increasing temperature, as shown in Fig. 10.6(a). Moreover, this transformation is detected in the FDMR up to 10 K. A representation of the temperature dependence of these features is depicted in Fig. 10.6.

The AMR measured at higher temperatures is shown in Fig. 10.7. At 4.2 K, shown in Fig. 10.7 (a), the AMR does not change significantly from that at 1.4 K. At  $B = 2$  T the AMR is almost flat around the  $[110]$  direction and, as already mentioned, the dip around  $[110]$  is more narrow than at 1.4 K for the same field. With increasing field the hysteretic step-like feature around  $[100]$  appears and  $\Delta\varphi$  for a 14 T field decreases only by  $2^\circ$  in comparison with the hysteresis at 1.4 K for the same field. However, at 8 K and 10 K, as depicted in Fig. 10.7 (b), the AMR is fully reversible for all field orientations and the step-like feature vanishes.

A further increase in temperature to  $T = 20$  K revealed that the resistance had no angular dependence and only a flat curve was observed. The AMR was mea-

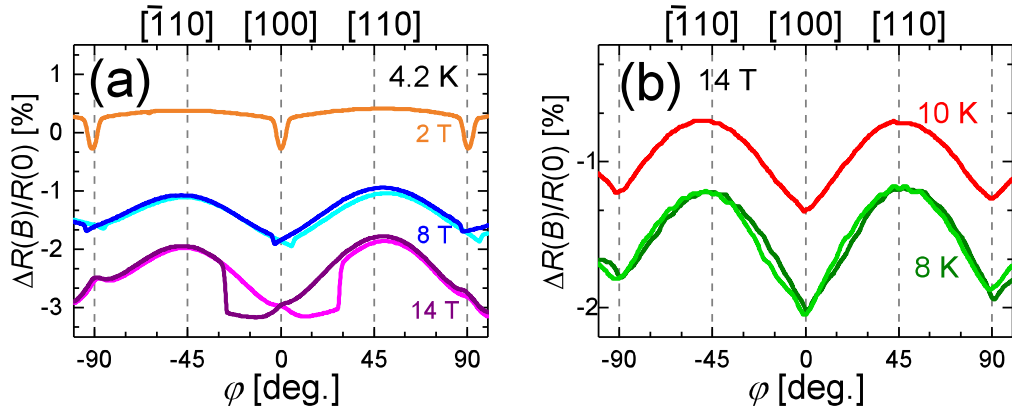


Figure 10.7: AMR of the NCCO  $x = 0.13$  as-grown sample at different temperatures: (a) AMR at  $T = 4.2$  K for increasing magnetic fields; (b) AMR at 8 K and 10 K for a 14 T applied field.

sured for temperatures up to 30 K without any sign of angular dependence of the resistance.

## 10.2 Discussion

Considering the above-presented results, the similarities between the as-grown and the annealed non-SC samples can be summarized as follows:

- Evidence of a transformation between the noncollinear and collinear states in the FDMR;
- Observation of the hysteretic step-like feature in the high-field AMR.

Within these two characteristics, certain differences arose and they will be addressed in the text.

Concerning the evidence of the transition from the noncollinear to the collinear structure for the NCCO  $x = 0.13$  as-grown sample, it was found in the FDMR for fields  $\mathbf{B} \parallel [100]$  and  $\mathbf{B} \parallel [110]$  in the temperature range 1.4 K – 4.2 K and 1.4 K – 10 K, respectively. The features attributed to these transformations at  $B_c$  were very pronounced, similar to that observed in the annealed  $x = 0.05$  sample. Additionally, it was observed that the transition field, in both orientations, decreases with increasing temperature.

The temperature dependence of  $B_c$  has been analysed for  $\mathbf{B} \parallel [110]$  in an NCCO sample with  $x = 0.025$  at  $T > 10$  K [91]. It was found that the  $B_c$  increases with temperature at  $T \leq 30$  K, but it decreases at higher temperatures. This change in the temperature dependence was attributed to the change in spin structures III and II. However, this temperature range is in a regime where the AMR could not be measured and thus it is not possible to conclude if the shift to lower fields is related to the change in spin phase.

Regarding the rotation of the azimuthal field within the  $ab$ -plane at low temperature, the AMR showed similar behavior to that observed in the annealed non-SC samples. The AMR has a  $90^\circ$  periodicity with a maximum at  $[110]$  and a minimum at or close to  $[100]$ . The step-like feature has a field-strength dependent hysteresis which is wider than for any annealed underdoped sample discussed in this work. In this sense, the hysteresis of the 15 T AMR of the  $x = 0.05$  sample discussed in Section 6.1.2 would be the most similar to the  $x = 0.13(\text{ag})$  sample. As it was discussed in chapter 9,  $\Delta\varphi$  depends on  $x$ . However, to determine if the width of the hysteresis in as-grown samples also changes with dopant concentration, the study of transport properties of as-grown samples with other dopant concentration is necessary. With the observation of the step-like feature as a signature of long-range AF order, it is confirmed that in the as-grown state of a  $x = 0.13$  NCCO sample long-range AF order is present.

In spite of the resemblance to the annealed non-SC samples, important differences were noticed. At temperatures as low as 8 K, the hysteresis in the AMR was no longer observed. Moreover, there was no measurable AMR at temperatures above 10 K. This observation contradicted the results from the behavior of the annealed non-SC samples, where it was found that the hysteresis shows a general temperature dependence and vanishes at  $T \approx 20$  K but reappears with increasing temperature. Moreover, the AMR could be measured up to temperatures even above 100 K. Therefore, such a difference in the temperature dependence is surprising. It should be kept in mind that the measurement of magnetoresistance is indeed a measurement of conductive properties. Also, it is known that the annealing process adds charge carriers to the lattice in the electron-doped cuprates [20, 33]. Changes in the amount of charge carriers can affect the transport, making it less sensitive to changes in the spin structure. On the other hand, similar studies of as-grown optimally doped PCCO samples have detected a sizable AMR at

high temperatures [104]. Therefore a certain conclusion cannot be reached in this matter.

The observed differences between the annealed samples and the as-grown one indicate that a minor structural change can directly affect the measured properties of the sample. Due to the limited number of experimental results in this respect, only a qualitative explanation for the observed results can be proposed. It should be remembered that, as discussed in Chapter 9, the hysteretic step-like feature in the high-field AMR is caused by a rearrangement of the  $\text{Cu}^{2+}$  spins within the AF collinear state. The nonmonotonic temperature dependence of the hysteresis with  $\Delta\varphi$  was attributed to the transitions between the AF phases III, II and I. The influence of the  $\text{Nd}^{3+}$  spins in the system was considered, both as a reason for the formation of the different spin phases and as source for an enhancement of the AMR features at low temperatures. This is caused by the participation of  $\text{Nd}^{3+}$  in the 3D long-range AF order in NCCO already below the  $T_N$  of  $\text{Cu}^{2+}$  plus an effective exchange interaction between the  $\text{Cu}^{2+}$  and  $\text{Nd}^{3+}$  [87]. Therefore, the AMR of an as-grown sample was expected to behave most similar to annealed non-SC samples.

Considering this, in Part I of this work, it has been noted that the real effect of the annealing process is not fully understood. One of the most accepted scenarios is that the reduction process eliminates excess of oxygen which occupies the apical sites in the  $T'$  structure. As a consequence, there is a small shrinkage of the lattice constant  $c$  which is more pronounced in the underdoped samples [111, 112]. Whatever small this change may be, it could have repercussions on the magnetic and electric environment felt by the  $\text{Cu}^{2+}$  and  $\text{Nd}^{3+}$  ions, since the Coulomb and exchange interactions become weaker with increasing distance. Additionally, in the as-grown state the apical oxygen between the  $\text{Cu}^{2+}$  and the  $\text{Nd}^{3+}$  ions could act as an additional barrier which impedes their interlayer interaction. During the measurement of the AMR, the applied magnetic field can cause the polarization of the unordered  $\text{Nd}^{3+}$  spins. Such polarization should create a local magnetic field in the system which can be felt by the  $\text{Cu}^{2+}$  spins. In an annealed sample the absence of apical oxygen allows for a better Nd-Cu interaction. So, if in an as-grown sample this interaction is deteriorated, the  $\text{Nd}^{3+}$  spins can only "act" at low temperatures, where the magnetic moment of the  $\text{Nd}^{3+}$  spins is strongly enhanced. Indeed, in the case of the  $x = 0.13(\text{ag})$  sam-

ple, evidence of the step-like feature is only observed at temperatures below 5 K. Additionally, an enhancement of the AMR is also seen in the annealed non-SC samples at the lowest temperatures.

In Section 9 it was discussed that the particular temperature dependence of the hysteresis  $\Delta\varphi$  in the NCCO system can be attributed to the transition between spin phases III, II and I. Unfortunately it is not known how the annealing process affects the spin phases of NCO, although from neutron diffraction measurements reported in the literature [87] no difference has been observed between two heat-treated samples in argon and oxygen, respectively. If there are no spin structures in as-grown samples, this could be another structural reason why the step-like feature is not seen since very low temperatures. The hysteresis would have a very steep decrease with temperature.

In summary, evidence of the transformation from noncollinear to collinear state was observed in the FDMR of an NCCO as-grown sample with  $x = 0.13$  at temperatures up to 4.2 K for a field aligned to the [100] direction and up to 10 K for the [110] direction. The hysteretic anomaly in the AMR was found for a limited temperature range,  $1.4 \text{ K} \leq T \leq 4.2 \text{ K}$ . Already above 10 K no evidence of angular dependence of the resistance was detected. Although the reasons for such unexpected behavior are unknown, it was argued that the structural effects of the annealing treatment on the sample, such as shrinkage of the lattice constant  $c$  and change in magnetic environment felt by the  $\text{Cu}^{2+}$  and  $\text{Nd}^{3+}$  ions, may be a reason for the obtained data. Nonetheless, further investigation on the transport properties of as-grown samples and the effect of the annealing process is necessary to determine if the observed results are typical of the as-grown state of the NCCO family.

# 11 Conclusions and Outlook

A systematic study of the interlayer field- and angle-dependent magnetoresistance of NCCO single crystals was done in a wide temperature range,  $1.4\text{ K} \leq T \leq 140\text{ K}$  in order to investigate the origin of the hysteretic anomaly in the AMR. The underdoped samples, either superconducting or non-superconducting, had a Ce concentration which corresponds to the doping range around the border of the superconducting region:  $0.09 \leq x \leq 0.13$  [20].

Two pronounced features have been observed on non-SC samples on top of a smooth  $90^\circ$ -periodic AMR background reflecting the square electronic/magnetic anisotropy of the system. The first one is observed during rotations in the intermediate field range,  $1\text{ T} \leq B \leq 4\text{ T}$ . A clear dip around the Cu–O–Cu direction is seen as the field is turned to the [100] direction from [110], which corresponds to the field-induced transition from the noncollinear to the collinear AF state. The second feature and the main focus of this work, is seen at higher fields. Around the [100] direction a remarkable hysteretic anomaly is found in the AMR. Additionally, a memory effect from the AMR could be measured through a particular measuring sequence. At a high field, the spin system is brought to a metastable state through rotation of the field to an angle  $\varphi < \varphi^*$ , and then the field is decreased. Through this sequence the relaxation of the spins at a field  $B^*$  during field sweeps could be detected.

A qualitative model is proposed in this work, which ascribes the generation of the step-like feature to a reorientation of the AF ordered  $\text{Cu}^{2+}$  spins in the high-field collinear state. Particularly, it is suggested that the spins remain frozen in a metastable state when the rotating magnetic field passes through the [100] direction. With further rotation of the field, at a critical angle  $\varphi^*$ , the spins relax to their equilibrium state. This conclusion is reached by considering that the direction of the staggered moment in the collinear state is not exactly perpendicular to the applied field but is actually inclined by an angle depending on the field

strength, as was shown earlier for undoped  $\text{Pr}_2\text{CuO}_4$  [95]. This model qualitatively explains the presence of the hysteresis and its step-like feature in the AMR high field regime in this work.

The hysteretic step-like feature was traced up to the highest temperatures used in this work,  $\sim 100$  K, significantly above  $T_{N,\text{Nd}}$ . This implies that this feature is originated from the antiferromagnetic  $\text{Cu}^{2+}$  system, as opposed to the low-temperature antiferromagnetism of  $\text{Nd}^{3+}$  ions, which was suggested to be responsible for the similar behavior in low-doped NCCO [11].

The temperature dependence of the hysteresis width  $\Delta\varphi$  was analyzed and a nonmonotonic behavior, which prevails for all dopings, was identified. This behavior is probably caused by the change in spin phases reported to occur in the parent compound NCO [87, 93]. This suggestion should be verified by direct investigations into the magnetic structure in this doping range.

The hysteresis width  $\Delta\varphi$  is found to become wider for stronger magnetic field. Unfortunately, within the existing theoretical model [94, 95] the reason for such field dependence is still unclear. Actually, it is natural to expect that when the Zeeman energy significantly exceeds the other relevant energy terms, the staggered moment will align exactly perpendicular to  $\mathbf{B}$  and the hysteresis will vanish. Thus, it would be interesting to perform the AMR experiment at higher magnetic fields to check at which field  $\Delta\varphi(B)$  reaches a maximum and starts to diminish.

Finally, a very important notion of this work is that the step-like feature is a clear indicator of long-range AF order in electron-doped cuprates. This is proposed considering that the origin of the step-like feature is in the collinear AF order of the  $\text{Cu}^{2+}$  spins. Even in the case where the qualitative model presented in the previous section were not fully accurate, the hysteresis is a sign of a magnetically nontrivial state. Extrapolating from a very low  $x$ , where the same behavior is observed and where the AF order of the  $\text{Cu}^{2+}$  spins is fully established, it is natural to associate the hysteresis with some rearrangement of the AF  $\text{Cu}^{2+}$  spins. The observation of the step-like feature can help avoid the ambiguity of conclusions derived from a fourfold or twofold smooth AMR.

Furthermore, the observation of hysteretic step-like feature in the SC samples at  $T > T_c$  indicates that the long-range AF survives up to the SC range of the phase diagram. However, the real origin of this coexistence is yet to be resolved.

---

This could be a result of spatial inhomogeneity of the samples, as an intrinsic property of the material or due to the post-growth annealing treatment, or an electronic effect where the two phases compete with each other.

While these results provide an understanding of the step-like feature in the underdoped regime of the phase diagram, additional questions remain and further work is necessary to fully comprehend these observations. For instance, from the results presented in section 6.1.1 on the  $x = 0.05$  NCCO, as doping is increased to  $x = 0.09$ , the anisotropy inverts and becomes much weaker. This implies that the dominant mechanism of magnetoresistance changes upon increasing the doping level, at least for the magnetic field aligned in the [100] direction. It could be interesting, for example, to investigate at which exact dopant concentration the anisotropy is inverted. Another possible investigation would be to analyse if there is a relation between the evolution of the conductive properties seen in AMR with the emergence of superconductivity.

Another important issue is the presence of the step-like feature in other electron-doped cuprates. While similar transport studies on  $\text{Pr}_{2-x}\text{Ce}_x\text{CuO}_4$  (PCCO) have not reported the presence of the step-like feature or hysteretic behavior in the AMR [101, 104], the spin-flop and noncollinear-collinear transitions in the FDMR have been detected. It is, thus, important to revisit the transport properties of PCCO with a special attention to the search of the step-like feature. The role of the rare-earth atom could be more important than expected in the emergence of this feature. The step-like feature in the collinear phases of PCCO is expected but it may be weaker, since it lacks the amplification effect of the  $\text{Nd}^{3+}$  spins. It should be mentioned that, as discussed in section 6.1.1, it is believed that the coupling of the Cu-Nd ions leads to the spin reorientation transitions with temperature in the parent compound NCO, which are absent in  $\text{Pr}_2\text{CuO}_4$  [89]. Because of this, a different temperature dependence of the hysteresis  $\Delta\varphi$  can be expected in the PCCO family, with a monotonic decrease of  $\Delta\varphi$  with increasing temperature.

Finally, it would be interesting to study the evolution of the AMR and step-like feature with different annealing periods. In Chapter 10, a short study of the magnetotransport of an as-grown NCCO  $x = 0.13$  single crystal was presented. However, the results indicate that further investigation is needed to relate the effect of annealing to the features observed in the FDMR and AMR.



# Bibliography

- [1] G. Koetitz, *Cryst. Res. Technol.* **25**, 682 (1990).
- [2] H. S. M. Coxeter, *The American Mathematical Monthly* **75**, 692 (1968).
- [3] N. Sloane, *Nature* **425**, 126 (2003).
- [4] P. Paufler, *Acta Crystallographica Section A* **68**, 523 (2012).
- [5] C. Kloc, T. Siegrist, and J. Pflaum, "Growth of single-crystal organic semiconductors," in *Springer Handbook of Crystal Growth*, edited by G. Dhanaraj, K. Byrappa, V. Prasad, and M. Dudley (Springer Berlin Heidelberg, Berlin, Heidelberg, 2010) pp. 845–867.
- [6] A. W. Vere, *Crystal Growth Principles and Progress* (Springer US, 1987).
- [7] A. Erb, E. Walker, J. Y. Genoud, and R. Flükiger, *Physica C: Superconductivity* **282**, 459 (1997), proceedings of the International Conference on Materials and Mechanisms of Superconductivity High Temperature Superconductors V Part II.
- [8] M. Däumling, J. M. Seuntjens, and D. C. Larbalestier, *Nature* **346**, 332 (1990).
- [9] L. Klein, E. R. Yacoby, Y. Yeshurun, A. Erb, G. Müller-Vogt, V. Breit, and H. Wühl, *Phys. Rev. B* **49**, 4403 (1994).
- [10] A. Erb, J. Y. Genoud, F. Marti, M. Däumling, E. Walker, and R. Flükiger, *J. Low Temp. Phys.* **105**, 1023 (1996).
- [11] T. Wu, C. H. Wang, G. Wu, D. F. Fang, J. L. Luo, G. T. Liu, and X. H. Chen, *J. Phys. Condens. Matter* **20**, 275226 (2008).

- [12] T. Helm, *Electronic properties of electron-doped cuprate superconductors probed by high-field magnetotransport*, Ph.D. thesis, Technical University of Munich (2013).
- [13] A. Alshemi, *Magnetoresistance of the electron-underdoped cuprate superconductor  $Nd_{2-x}Ce_xCuO_4$* , Master's thesis, Technical University of Munich (2015).
- [14] H. Takagi, S. Uchida, and Y. Tokura, *Phys. Rev. Lett.* **62**, 1197 (1989).
- [15] E. Takayama-Muromachi, Y. Matsui, Y. Uchida, F. Izumi, M. Onoda, and K. Kato, *Jpn. J. Appl. Phys.* **27**, L2283 (1988).
- [16] J. Akimitsu, S. Suzuki, M. Watanabe, and H. Sawa, *Jpn. J. Appl. Phys.* **27**, L1859 (1988).
- [17] Y. Dalichaouch, M. de Andrade, and M. Maple, *Physica C: Superconductivity* **218**, 309 (1993).
- [18] P. Fournier, *Physica C: Superconductivity and its Applications* **514**, 314 (2015).
- [19] J. Hirsch, *Physica C: Superconductivity* **243**, 319 (1995).
- [20] N. P. Armitage, P. Fournier, and R. L. Greene, *Rev. Mod. Phys.* **82**, 2421 (2010).
- [21] M. Lambacher, *Crystal growth and normal state transport of electron doped high temperature superconductors*, Ph.D. thesis, Technical University of Munich (2008).
- [22] C. Niedermayer, C. Bernhard, T. Blasius, A. Golnik, A. Moodenbaugh, and J. I. Budnick, *Phys. Rev. Lett.* **80**, 3843 (1998).
- [23] P. K. Mang, O. P. Vajk, A. Arvanitaki, J. W. Lynn, and M. Greven, *Phys. Rev. Lett.* **93**, 027002 (2004).
- [24] S. Li, S. Chi, J. Zhao, H.-H. Wen, M. B. Stone, J. W. Lynn, and P. Dai, *Phys. Rev. B* **78**, 014520 (2008).
- [25] M. Matsuda, Y. Endoh, K. Yamada, H. Kojima, I. Tanaka, R. J. Birgeneau, M. A. Kastner, and G. Shirane, *Phys. Rev. B* **45**, 12548 (1992).

- [26] E. M. Motoyama, G. Yu, I. M. Vishik, O. P. Vajk, P. K. Mang, and M. Greven, *Nature* **445**, 186 (2007).
- [27] T. Uefuji, T. Kubo, K. Yamada, M. Fujita, K. Kurahashi, I. Watanabe, and K. Nagamine, *Physica C: Superconductivity* **357**, 208 (2001).
- [28] G. M. Luke, L. P. Le, B. J. Sternlieb, Y. J. Uemura, J. H. Brewer, R. Kadono, R. F. Kiefl, S. R. Kreitzman, T. M. Riseman, C. E. Stronach, M. R. Davis, S. Uchida, H. Takagi, Y. Tokura, Y. Hidaka, T. Murakami, J. Gopalakrishnan, A. W. Sleight, M. A. Subramanian, E. A. Early, J. T. Markert, M. B. Maple, and C. L. Seaman, *Phys. Rev. B* **42**, 7981 (1990).
- [29] M. Fujita, T. Kubo, S. Kuroshima, T. Uefuji, K. Kawashima, K. Yamada, I. Watanabe, and K. Nagamine, *Phys. Rev. B* **67**, 014514 (2003).
- [30] M. Lambacher, T. Helm, M. Kartsovnik, and A. Erb, *Eur. Phys. J. Special Topics* **188**, 61 (2010).
- [31] J. S. Higgins, Y. Dagan, M. C. Barr, B. D. Weaver, and R. L. Greene, *Phys. Rev. B* **73**, 104510 (2006).
- [32] H. J. Kang, P. Dai, B. J. Campbell, P. J. Chupas, S. Rosenkranz, P. L. Lee, Q. Huang, S. Li, S. Komiya, and Y. Ando, *Nat Mater* **6**, 224 (2007).
- [33] P. K. Mang, S. Laroche, A. Mehta, O. P. Vajk, A. S. Erickson, L. Lu, W. J. L. Buyers, A. F. Marshall, K. Prokes, and M. Greven, *Phys. Rev. B* **70**, 094507 (2004).
- [34] M. Naito, Y. Krockenberger, A. Ikeda, and H. Yamamoto, *Physica C: Superconductivity and its Applications* **523**, 28 (2016).
- [35] P. Richard, G. Riou, I. Hetel, S. Jandl, M. Poirier, and P. Fournier, *Phys. Rev. B* **70**, 064513 (2004).
- [36] R. Puche, M. Norton, and W. Glaunsinger, *Mater. Res. Bull.* **17**, 1523 (1982).
- [37] M. Dixon, *Physica C: Superconductivity* **174**, 117 (1991).
- [38] J. M. Tranquada, S. M. Heald, A. R. Moodenbaugh, G. Liang, and M. Croft, *Nature* **337**, 720 (1989).

- [39] N. P. Armitage, F. Ronning, D. H. Lu, C. Kim, A. Damascelli, K. M. Shen, D. L. Feng, H. Eisaki, Z.-X. Shen, Y. Onose, Y. Taguchi, and Y. Tokura, *Phys. Rev. Lett.* **88** (2002), 10.1103/PhysRevLett.88.257001.
- [40] H. Matsui, T. Takahashi, T. Sato, K. Terashima, H. Ding, T. Uefuji, and K. Yamada, *Phys. Rev. B* **75** (2007).
- [41] A. F. Santander-Syro, M. Ikeda, T. Yoshida, A. Fujimori, K. Ishizaka, M. Okawa, S. Shin, R. L. Greene, and N. Bontemps, *Phys. Rev. Lett.* **106**, 197002 (2011).
- [42] B. Kyung, V. Hankevych, A.-M. Daré, and A.-M. S. Tremblay, *Phys. Rev. Lett.* **93**, 147004 (2004).
- [43] D. Song, G. Han, W. Kyung, J. Seo, S. Cho, B. S. Kim, M. Arita, K. Shimada, H. Namatame, M. Taniguchi, Y. Yoshida, H. Eisaki, S. R. Park, and C. Kim, *Phys. Rev. Lett.* **118**, 137001 (2017).
- [44] M. V. Kartsovnik, T. Helm, C. Putzke, F. Wolff-Fabris, I. Sheikin, S. Lepault, C. Proust, D. Vignolles, N. Bittner, W. Biberacher, A. Erb, J. Wosnitza, and R. Gross, *New J. Phys.* **13**, 015001 (2011).
- [45] T. Helm, M. V. Kartsovnik, M. Bartkowiak, N. Bittner, M. Lambacher, A. Erb, J. Wosnitza, and R. Gross, *Phys. Rev. Lett.* **103** (2009).
- [46] W. S. Lee, J. J. Lee, E. A. Nowadnick, S. Gerber, W. Tabis, S. W. Huang, V. N. Strocov, E. M. Motoyama, G. Yu, B. Moritz, H. Y. Huang, R. P. Wang, Y. B. Huang, W. B. Wu, C. T. Chen, D. J. Huang, M. Greven, T. Schmitt, Z. X. Shen, and T. P. Devereaux, *Nat. Phys.* **10**, 883 (2014).
- [47] E. H. da Silva Neto, R. Comin, F. He, R. Sutarto, Y. Jiang, R. L. Greene, G. A. Sawatzky, and A. Damascelli, *Science* **347**, 282 (2015), <http://science.sciencemag.org/content/347/6219/282.full.pdf>.
- [48] E. H. da Silva Neto, B. Yu, M. Minola, R. Sutarto, E. Schierle, F. Boschini, M. Zonno, M. Bluschke, J. Higgins, Y. Li, G. Yu, E. Weschke, F. He, M. Le Tacon, R. L. Greene, M. Greven, G. A. Sawatzky, B. Keimer, and A. Damascelli, *Science Advances* **2**, e1600782 (2016).

- 
- [49] J. C. S. Davis and D.-H. Lee, *Proceedings of the National Academy of Sciences of the United States of America* **110**, 17623 (2013).
- [50] M. Hücker, M. v. Zimmermann, G. D. Gu, Z. J. Xu, J. S. Wen, G. Xu, H. J. Kang, A. Zheludev, and J. M. Tranquada, *Phys. Rev. B* **83**, 104506 (2011).
- [51] A. N. Lavrov, H. J. Kang, Y. Kurita, T. Suzuki, S. Komiya, J. W. Lynn, S.-H. Lee, P. Dai, and Y. Ando, *Phys. Rev. Lett.* **92**, 227003 (2004).
- [52] H. Shibata, K. Oka, S. Kashiwaya, and H. Yamaguchi, *Physica C: Superconductivity* **357**, 363 (2001).
- [53] Y. Krockenberger, H. Irie, O. Matsumoto, K. Yamagami, M. Mitsuhashi, A. Tsukada, M. Naito, and H. Yamamoto, *Scientific Reports* **3**, 2235 (2013).
- [54] A. Dorantes, *Magnetic properties of high quality single crystals of the electron underdoped cuprate superconductor  $Nd_{2-x}Ce_xCuO_4$* , Master's thesis, Technical University of Munich (2013).
- [55] M. Matsuura, P. Dai, H. J. Kang, J. W. Lynn, D. N. Argyriou, K. Prokes, Y. Onose, and Y. Tokura, *Phys. Rev. B* **68**, 144503 (2003).
- [56] A. Balbashov and S. Egorov, *Journal of Crystal Growth* **52**, 498 (1981).
- [57] M. Matsuda, Y. Endoh, and Y. Hidaka, *Physica C: Superconductivity* **179**, 347 (1991).
- [58] G. Dhanaraj, K. Byrappa, V. Prasad, and M. Dudley, *Springer Handbook of Crystal Growth* (Springer-Verlag Berlin Heidelberg, 2010).
- [59] W. Nerst, *Z. Phys. Chem.* **47**, 52 (1904).
- [60] A. Vere, *Crystal growth Principles and Progress*, edited by P. Dobson (Springer Science+Business, 1987).
- [61] W. Kossel, *Nachr. Ges. Wiss. Göttingen* **137**, 135 (1927).
- [62] M. Volmer and A. Weber, *Z. Phys. Chem.* **119**, 277–301 (1926).
- [63] C. H. Ting, in *Encyclopedia of Materials Characterization* (Butterworth-Heinemann, Boston, 1992) pp. 338 – 348.

- [64] L. Calvo Barrio and G. Vargas, *Photoelectron spectroscopy for surface analysis: X-ray and UV excitation* (Centro de ciencia y tecnologia de la Universidad de Barcelona, 2012).
- [65] C. P. BEAN, *Rev. Mod. Phys.* **36**, 31 (1964).
- [66] A. Galluzzi, M. Polichetti, K. Buchkov, E. Nazarova, D. Mancusi, and S. Pace, *Supercond. Sci. Technol.* **28**, 115005 (2015).
- [67] G. E. Bacon, *Neutron Diffraction* (Oxford University Press, 1962).
- [68] G. Shirane, S. M. Shapiro, and J. M. Tranquada, *Neutron scattering with a triple-axis spectrometer: basic techniques* (Cambridge University Press, 2002).
- [69] G. L. Squires, *Introduction to the Theory of Thermal Neutron Scattering* (Cambridge University Press, 2012).
- [70] E. M. Davenport Motoyama, *Neutron Scattering studies of the Electron-Doped High-Temperature superconductor Neodymium Cerium Copper Oxide*, Ph.D. thesis, Stanford University (2009).
- [71] H. Z. Berlin, "Introduction to neutron scattering," Lectures at the HZB school on neutron scattering (2015).
- [72] R. Pynn, "Neutron scattering: a primer," Los Alamos National Laboratory (1990).
- [73] H. J. Kang, P. Dai, J. W. Lynn, M. Matsuura, J. R. Thompson, S.-C. Zhang, D. N. Argyriou, Y. Onose, and Y. Tokura, *Nature* **423**, 522 (2003).
- [74] T. Uefuji, K. Kurahashi, M. Fujita, M. Matsuda, and K. Yamada, *Physica C: Superconductivity* **378-381**, 273 (2002).
- [75] W. Jiang, S. N. Mao, X. X. Xi, X. Jiang, J. L. Peng, T. Venkatesan, C. J. Lobb, and R. L. Greene, *Phys. Rev. Lett.* **73**, 1291 (1994).
- [76] H. J. Kang, P. Dai, H. A. Mook, D. N. Argyriou, V. Sikolenko, J. W. Lynn, Y. Kurita, S. Komiya, and Y. Ando, *Phys. Rev. B* **71**, 214512 (2005).
- [77] P. G. Radaelli, J. D. Jorgensen, A. J. Schultz, J. L. Peng, and R. L. Greene, *Phys. Rev. B* **49**, 15322 (1994).

- 
- [78] N. Fortune, K. Murata, Y. Yokoyama, M. Ishibashi, and Y. Nishihara, *Physica C: Superconductivity* **178**, 437 (1991).
- [79] Y. Krockenberger, M. Horio, H. Irie, A. Fujimori, and H. Yamamoto, *Appl. Phys. Express* **8**, 053101 (2015).
- [80] J. W. Cahn, *J. Chem. Phys.* **42**, 93 (1965), <http://dx.doi.org/10.1063/1.1695731>.
- [81] A. J. Bradley, *Proceedings of the Physical Society* **52**, 80 (1940).
- [82] J. M. Tranquada, *Physica B: Condensed Matter* **407**, 1771 (2012), proceedings of the International Workshop on Electronic Crystals (ECRYS-2011).
- [83] H. Takagi, S. Uchida, and Y. Tokura, *Phys. Rev. Lett.* **62**, 1197 (1989).
- [84] V. J. Emery, *J. Appl. Phys.* **67**, 4666 (1990).
- [85] J. F. Ding, Y. W. Yin, L. Xie, Q. X. Yu, and X. G. Li, *J. Phys. Condens. Matter* **22**, 275701 (2010).
- [86] M. A. Kastner, R. J. Birgeneau, G. Shirane, and Y. Endoh, *Rev. Mod. Phys.* **70**, 897 (1998).
- [87] M. Matsuda, K. Yamada, K. Kakurai, H. Kadowaki, T. R. Thurston, Y. Endoh, Y. Hidaka, R. J. Birgeneau, M. A. Kastner, P. M. Gehring, A. H. Moudden, and G. Shirane, *Phys. Rev. B* **42**, 10098 (1990).
- [88] J. W. Lynn, I. W. Sumarlin, S. Skanthakumar, W.-H. Li, R. N. Shelton, J. L. Peng, Z. Fisk, and S.-W. Cheong, *Phys. Rev. B* **41**, 2569 (1990).
- [89] R. Sachidanandam, T. Yildirim, A. B. Harris, A. Aharony, and O. Entin-Wohlman, *Phys. Rev. B* **56**, 260 (1997).
- [90] S. Skanthakumar, J. W. Lynn, J. L. Peng, and Z. Y. Li, *Phys. Rev. B* **47**, 6173 (1993).
- [91] S. Li, S. D. Wilson, D. Mandrus, B. Zhao, Y. Onose, Y. Tokura, and P. Dai, *Phys. Rev. B* **71**, 054505 (2005).

- [92] A. I. Ponomarev, L. D. Sabirzyanova, A. A. Ivanov, A. S. Moskvin, and Y. D. Panov, *JETP Lett.* **81**, 394 (2005).
- [93] D. Petitgrand, A. Moudden, P. Galez, and P. Boutrouille, *J. Less-Common Met.* **164**, 768 (1990).
- [94] D. Petitgrand, S. V. Maleyev, P. Bourges, and A. S. Ivanov, *Phys. Rev. B* **59**, 1079 (1999).
- [95] V. P. Plakhty, S. V. Maleyev, S. V. Gavrilov, F. Bourdarot, S. Pouget, and S. N. Barilo, *Europhys. Lett.* **61**, 534 (2003).
- [96] X. H. Chen, C. H. Wang, G. Y. Wang, X. G. Luo, J. L. Luo, G. T. Liu, and N. L. Wang, *Phys. Rev. B* **72**, 064517 (2005).
- [97] S. Blundell, *Magnetism in Condensed-matter* (Oxford University Press, 2001).
- [98] M. V. Kartsovnik, *Chem. Rev.* **104**, 5737 (2004), <http://dx.doi.org/10.1021/cr0306891>.
- [99] A. A. Abrikosov, *Fundamentals of the theory of metals* (North Holland, 1988).
- [100] Y. Dagan, M. Barr, W. Fisher, R. Beck, T. Dhakal, A. Biswas, and R. Greene, *Phys. Rev. Lett.* **94** (2005).
- [101] W. Yu, J. S. Higgins, P. Bach, and R. L. Greene, *Phys. Rev. B* **76**, 020503 (2007).
- [102] K. Jin, X. H. Zhang, P. Bach, and R. L. Greene, **80**, 012501 (2009).
- [103] V. P. Jovanović, L. Fruchter, Z. Z. Li, and H. Raffy, *Phys. Rev. B* **81**, 134520 (2010).
- [104] P. Fournier, M.-E. Gosselin, S. Savard, J. Renaud, I. Hetel, P. Richard, and G. Riou, *Phys. Rev. B* **69**, 220501 (2004).
- [105] A. S. Alexandrov, V. V. Kabanov, and N. F. Mott, *Phys. Rev. Lett.* **77**, 4796 (1996).

- [106] D. Andres, *Effects of high magnetic fields and hydrostatic pressure on the low temperature density wave state of the organic metal alpha-(BEDT-TTF)<sub>2</sub>KHg(SCN)<sub>4</sub>*, [Ph.D. thesis](#), Technical University of Munich (2005).
- [107] T. Helm, "Transport measurements in 214 high-temperature superconductors," (2009).
- [108] Y. Ando, A. N. Lavrov, and S. Komiya, [Phys. Rev. Lett. \*\*90\*\*, 247003 \(2003\)](#).
- [109] S. Ghamaty, B. Lee, J. Markert, E. Early, T. Bjørnholm, C. Seaman, and M. Maple, [Physica C: Superconductivity \*\*160\*\*, 217 \(1989\)](#).
- [110] A. N. Bazhan, [J. Magn. Magn. Mat. \*\*272\*\*, 361 \(2004\)](#).
- [111] H. Takagi, S. Uchida, and Y. Tokura, [Phys. Rev. Lett. \*\*62\*\*, 1197 \(1989\)](#).
- [112] O. Matsumoto, A. Utsuki, A. Tsukada, H. Yamamoto, T. Manabe, and M. Naito, [Physica C: Superconductivity \*\*469\*\*, 924 \(2009\)](#).



## Publication

A. Dorantes, A. Alshemi, Z. Huang, A. Erb and M.V. Kartsovnik. "Magnetotransport evidence of irreversible spin reorientation in the collinear antiferromagnetic state of underdoped  $\text{Nd}_{2-x}\text{Ce}_x\text{CuO}_4$ ." *Physical Review B* **97**, 054430 (2018).



## 12 Acknowledgements

During the past years I have been fortunate to have met a great variety of people who have contributed to this work. At the end of this thesis I would like to express my gratitude, in particular, to:

- Prof. Dr. Peter Böni, for his very enthusiastic supervision during my PhD and for opening the doors of the neutron science for me.
- Prof. Dr. Andreas Erb for giving me the opportunity to work in this project, for trusting me with such an interesting topic.
- Dr. Mark Kartsovnik for his excellent supervision and big help with many experiments. For challenging me with new tasks and for always being patient with this material scientist. For the tea and the good conversations.
- Prof. Dr. Rudolf Gross, for the opportunity to work at the WMI.
- Prof. Dr. Jürgen Haase, for the financial support in the last months of my thesis and for welcoming me in his group in Leipzig for a research visit.
- Dr. Robert Georgii, Dr. Tobias Weber and Dr. Markos Skoulatos from the Heinz-Maier-Leibnitz Institute FRM II for helping me with the neutron scattering experiments performed in this thesis.
- Dr. Arnaud Magrez from the École Polytechnique Fédérale de Laussane (EPFL) for the X-Ray Fluorescence analysis on my samples.
- The technical staff at WMI Karen Helm-Knapp and Astrid Habel. For helping me with the crystal growth and always being there for a nice talk.
- The colleagues of the crystal laboratory at the Physics department, particularly to Sussane Mayr and Katarzyna Danielewicz, for helping me with the

- sample preparation throughout these years. For being good colleagues and friends to me.
- Our exchange students Khai Qi and Zengle Huang, for being good friends and colleagues. For their help with the crystal growth and magnetoresistance experiments, respectively.
  - For the financial support of Consejo Nacional de Ciencia y Tecnología (CONACYT).
  - My friends Dr. Alison Barker and Carlos Pachajoa, who showed me great support during these years and always encouraged me to continue the hard work.
  - Johannes Lotze, for being a great partner and a source of advise and motivation. For his companionship and for always believing in me.
  - My family in Mexico. For everything.